
Collisional interaction between metastable neon atoms

Vom Fachbereich Physik der Technischen Universität Darmstadt
zur Erlangung des Grades
eines Doktors der Naturwissenschaften
(Dr. rer. nat.)

genehmigte Dissertation von

Wouter Johannes van Drunen M.Sc.
aus Amsterdam, Niederlande

Referent: Prof. Dr. Gerhard Birkl
Korreferent: Prof. Dr. Wolfgang Elsäßer

Tag der Einreichung: 13. Juni 2008
Tag der mündlichen Prüfung: 07. Juli 2008

Darmstadt 2008
Hochschulkennziffer D17

Abstract

In this thesis, the study of cold gases of neon atoms in different metastable states is described. It contains measurements of the collisional parameters for both the $3s[3/2]_2$ and the $3s'[1/2]_0$ metastable state and the dependence of the inelastic loss on external fields. Furthermore, the investigation of frequency dependent laser-induced collisions, and the possibility to excite photoassociation resonances is presented. Based on previous measurements we have selected ^{22}Ne for evaporative cooling. Although, we can experimentally achieve an increase in phase-space density with evaporative cooling, the relatively high inelastic collision parameters prevent the realization of a Bose-Einstein condensate in neon.

For the measurements described here, neon atoms have been confined in a magneto-optical trap, in a magnetostatic trap, or in an optical dipole trap, respectively. By laser cooling inside the magnetic trap, atomic samples with more than 95 percent occupation of the magnetic substate $m_J = +2$ could be prepared. They have a typical temperature of 0.5 mK, central densities up to 10^{11} cm^{-3} , and a central phase-space density of up to $2.2 \cdot 10^{-7}$. After loading the optical dipole trap from the magnetic trap, $2.5 \cdot 10^6$ atoms with typical temperatures of 0.1 mK, and central densities up to $5 \cdot 10^{10} \text{ cm}^{-3}$ were trapped. By evaporative cooling of the atoms in the magnetic trap we could increase the phase-space density by a factor of 200 to $5 \cdot 10^{-5}$. Also simulations of optimized evaporation for our experimental parameters show clearly that we are limited to a phase-space density on the order of 10^{-5} . From these simulations it became clear that a 5-fold increase in the "good-to-bad" ratio for evaporative cooling suffices to reach the quantum degenerate regime.

Investigating the frequency dependence of laser-induced collisions did not reveal an experimental signature for the excitation of photoassociation resonances. For the $^3\text{D}_3$ line a frequency dependence of laser enhanced Penning ionization was observed, which is interesting in itself. The absence of the collisional enhancement effect by laser light for the transition to the $^3\text{D}_2$ line is intriguing and for an explanation calculations are required. Measurement of the two-body loss coefficient as function of the magnetic field showed a field dependence of the inelastic loss. These losses increase towards both small and large offset fields. In the magnetic trap, we are limited to offset fields $\leq 50 \text{ G}$. In this range of fields, the two-body losses are too large to achieve a Bose-Einstein condensate of magnetically trapped metastable neon.

The implementation of an optical dipole trap allowed us to trap the $^3\text{P}_0$ metastable state. From the trap loss measurements we determined the two-body loss coefficient of the $^3\text{P}_0$ metastable state for both bosonic isotopes ^{20}Ne and ^{22}Ne . For ^{20}Ne we obtained

$\beta = 6_{-4}^{+5} \cdot 10^{-10} \text{ cm}^3/\text{s}$ and for ^{22}Ne $\beta = 11_{-6}^{+7} \cdot 10^{-10} \text{ cm}^3/\text{s}$. These large two-body losses make it extremely unlikely to reach degeneracy with this metastable state.

Nevertheless it is important that the $^3\text{P}_0$ metastable state can be trapped to investigate other interesting physical effects. For example, it is essential to apply the STIRAP technique for trapped atoms and to realize the proposed coherent control of collisions. There is also a large interest in a precise determination of the lifetime of this metastable state, which is of importance for the verification of QED. We can also trap neon atoms in their energetically lowest magnetic substate $^3\text{P}_2(m = -2)$ with the perspective of reducing inelastic collisions in the energetically lowest state.

Zusammenfassung

Die vorliegende Dissertation befasst sich mit kalten Gasen aus Neonatomen in verschiedenen metastabilen Zuständen. Hierbei wird auf die Untersuchung der Stoßparameter für die $3s[3/2]_2$ und $3s[1/2]_0$ metastabilen Zustände und die Abhängigkeit der inelastischen Stoßparameter von externen Feldern eingegangen. Des Weiteren werden die Resultate der frequenzabhängigen laser-induzierten Stöße mit der Möglichkeit zur Anregung photoassoziativer Resonanzen beschrieben. Basierend auf vorherigen Messungen wurde ^{22}Ne für die Verdampfungskühlung ausgewählt. Obwohl eine Erhöhung der Phasenraumdichte experimentell erreicht werden kann, erschweren die Zwei-Körper-Verlust-Parameter die Realisation eines Bose-Einstein-Kondensates metastabilen Neons auf direktem Weg.

Für die hier beschriebenen Messungen wurden Neonatome in einer magneto-optischen Falle, in einer magnetostatischen Falle bzw. in einer optischen Dipolfalle gespeichert. Durch Laserkühlung innerhalb der Magnetfalle konnten Ensembles mit über 95% Besetzung des magnetischen Unterzustandes $m_J = +2$ präpariert werden. Sie weisen eine typische Temperatur von 0,5 mK, eine zentrale Dichte von bis zu 10^{11} cm^{-3} und eine zentrale Phasenraumdichte von bis zu $2,2 \cdot 10^{-7}$ auf. Nach dem Laden der Dipolfalle sind $2,2 \cdot 10^6$ Atome mit einer typischen Temperatur von 0,1 mK und einer zentralen Dichte von bis zu $5 \cdot 10^{10} \text{ cm}^{-3}$ gefangen worden.

Mit Hilfe der Verdampfungskühlung in der Magnetfalle konnte die Phasenraumdichte um einen Faktor 200 bis zu $5 \cdot 10^{-5}$ erhöht werden. Simulationsrechnungen der optimierten Verdampfungskühlung für typische experimentelle Parameter zeigen, dass eine maximale Phasenraumdichte in Größenordnung 10^{-5} erreichbar ist. Sie zeigen aber auch, dass zum Erreichen des quantenentarteten Regimes eine 5-fache Erhöhung des Verhältnisses von guten zu schlechten Stößen genügt.

Bei der Untersuchung frequenzabhängiger laser-induzierter Stöße konnte keine Anregung photoassoziativer Resonanzen beobachtet werden. Für die $^3\text{D}_3$ Linie wurde eine Frequenzabhängigkeit der laser-induzierten Penning-Ionisation gemessen. Die Abwesenheit der Erhöhung der Stoßrate für den Übergang zu der $^3\text{D}_2$ Linie ist bemerkenswert. Diese Messungen liefern entscheidende Eingangsparameter für weitere theoretische Untersuchungen.

Messungen der Zwei-Körper-Verlustraten als Funktion des Magnetfeldes zeigen eine Feldabhängigkeit der inelastischen Verlustprozesse. Diese Verluste steigen für niedrige und auch für hohe Offsetfelder. In der Magnetfalle sind die Offsetfelder auf 50 G begrenzt. In diesem Bereich ist die Zwei-Körper-Verlustrate zu hoch, um die Bose-Einstein Kondensation von magnetisch gefangenem metastabilen Neon zu erreichen.

Die Implementierung der optischen Dipolfalle ermöglicht das Fangen des metastabilen

Zustandes 3P_0 . Aus den Fallenverlusten konnte die dichteabhängige Rate inelastischer Stöße sowohl für ${}^{20}\text{Ne}$ als auch ${}^{22}\text{Ne}$ bestimmt werden. Für ${}^{20}\text{Ne}$ beträgt der Verlustparameter $\beta = 6_{-4}^{+5} \cdot 10^{-10} \text{ cm}^3/\text{s}$ und für ${}^{22}\text{Ne}$ $\beta = 11_{-6}^{+7} \cdot 10^{-10} \text{ cm}^3/\text{s}$. Aufgrund dieser hohen Zwei-Körper-Verlustrate ist es sehr unwahrscheinlich, dass das quantenentartete Regime mit diesem metastabilen Zustand erreicht werden kann.

Weiterhin ermöglicht das Fangen des 3P_0 Zustandes zum Beispiel die Implimentierung von STIRAP für gefangene Atome und die Realisierung der vorgeschlagenen kohärenten Kontrollen von Stößen. Die präzise Messung der Lebensdauer dieses metastabilen Zustandes könnte außerdem zur Verifizierung der QED dienen. Es besteht außerdem die Möglichkeit auch Neonatome in ihrem energetisch niedrigsten Zustand ${}^3P_2(m_J = -2)$ zu fangen, in dem eine weitere Reduzierung der Zwei-Körper-Verluste erwartet wird.

Contents

1	Introduction	1
2	Experimental setup	5
2.1	Properties of metastable neon	5
2.2	Overview of the experimental setup	6
2.2.1	Computer control	7
2.2.2	Laser systems	7
2.2.3	Optical setup	8
2.2.4	Collimated beam of metastable neon atoms	9
2.2.5	Zeeman slower	10
2.2.6	Magneto-optical trap	10
2.2.7	Magnetic trap	12
2.2.8	Evaporative cooling	16
2.3	Determination of the atomic ensemble parameters	16
2.3.1	Optical detection	17
2.3.2	Electronic detection	19
2.4	Preparation of magnetic trapped spin-polarized atoms	21
3	Collisional parameters of metastable neon	25
3.1	Ionization rate	25
3.1.1	Calibration of the MCP	26
3.1.2	Measurements in the magnetic trap	27
3.1.3	Conclusion	27
3.2	Evaporative cooling	28
3.2.1	Short introduction to theory of evaporative cooling	29
3.2.2	Experimental realization	30

3.2.3	Simulation of the evaporative cooling	31
3.2.4	Conclusion	34
4	Light-assisted collision experiments	37
4.1	Experimental procedure	38
4.2	Experiment at the $^3P_2 \rightarrow ^3D_3$ transition	40
4.3	Experiment at the $^3P_2 \rightarrow ^3D_2$ transition	40
4.4	Conclusion	43
5	Two-body loss coefficient as function of magnetic field	45
5.1	Theoretical description of the trap loss	45
5.2	Measurements	47
5.3	Conclusion	51
6	Trapping neon in the 3P_0 metastable state	53
6.1	The optical dipole trap	54
6.1.1	ac Stark shift	54
6.1.2	Optical dipole trap	57
6.1.3	Density distribution in an optical dipole trap	59
6.2	Implementation of a crossed optical dipole trap	61
6.2.1	Experimental setup	61
6.2.2	Loading of the optical dipole trap	62
6.2.3	Optimization of the crossed optical dipole trap	63
6.2.4	Transfer to the 3P_0 metastable state	63
6.3	First trapping of neon in the 3P_0 metastable state	64
7	Collisional properties of the 3P_0 metastable state	67
7.1	Determination of the trap parameters	67
7.1.1	Intensity distribution and beam pointing stability of the laser beams	67
7.1.2	Parametric heating	70
7.1.3	Measurement of the radial density distribution	71
7.1.4	Summary of the trap parameters	72
7.2	Determination of the two-body loss coefficient	73
7.2.1	Theoretical treatment of the trap loss	73
7.2.2	Experimental procedure	74

<i>CONTENTS</i>	ix
7.2.3 Systematic effects in the detection of the atoms	75
7.2.4 Extraction of the two-body loss coefficients from atom loss measurements	80
7.3 Conclusion	81
8 Concluding remarks	83
A Neon parameters	97
B Laser intensity stabilization scheme	101

Chapter 1

Introduction

Experimental research on ultracold atomic gases involves atoms at typical temperatures in the range of nanoKelvin to a few milliKelvin and densities between the 10^{10} to 10^{15} cm^{-3} . In comparison, the air around us has typical densities of 10^{19} cm^{-3} . At these densities and ultra-low temperatures, we have access to a regime in which quantum effects play an important role. This is especially the case for a gas in the quantum degeneracy regime. Depending on the nature of the atoms, one has either a Bose-Einstein condensate or Fermi degeneracy. The difference between the two is of profound importance. In 1995 groups at JILA, a laboratory run by the National Institute of Standards and Technology and the University of Colorado in Boulder, Colorado, and the Massachusetts Institute of Technology (MIT) obtained for the first time compelling evidence for Bose-Einstein condensation in dilute atomic gases [1, 2, 3, 4]. Four years later Fermi degeneracy in a trapped gas ("Fermi sea") was also observed [5, 6, 7].

Research of cold and ultracold atomic gases combines different areas of physics: Atomic and molecular physics, quantum optics and physics of condensed matter [8, 9, 10, 11, 12, 13, 14]. This is expressed by the remarkable properties of a Bose-Einstein condensate. The coherence property of a Bose-Einstein condensate is closely related to the properties of a laser. Because of this property, the condensate is a macroscopic extended quantum object. The coherence property of the condensate is also responsible that this unusual state of matter shows properties, which are known from superfluids and superconductors. Examples of the various properties of a Bose-Einstein condensate in the area of quantum optics are the observation of interferences between two condensates [15], four-wave mixing [16] and propagation of solitons [17, 18]. In condensed matter physics, examples are the observation of Abriksov lattices from vortices [19, 20] and the Mott-insulator transition [21].

The techniques to obtain (ultra)cold gases are trapping and cooling of neutral atoms. For trapping of the atoms, mostly magneto-optical [22], optical dipole [23] and magnetic traps [24] are used. Cooling of the atoms is achieved by a sequence of laser cooling methods followed by evaporative cooling [25]. An overview of the different laser cooling methods is given in Metcalf and van der Straten [26]. Evaporative cooling is based on the removal of atoms from the high energy part of the Boltzmann distribution. This leads to a

truncated Boltzmann distribution in the trap. In elastic collisions between trapped atoms, some atoms gain an energy larger than the trap depth and are removed. Their collision partners lose energy in the collision leading to a smaller mean energy of the trapped atoms after the elastic collision. This technique has led to the Bose-Einstein condensation of many different species: ^1H , ^7Li , ^{23}Na , ^{39}K , ^{41}K , ^{52}Cr , ^{85}Rb , ^{87}Rb , ^{133}Cs , ^{174}Yb , ^{176}Yb and metastable helium $^4\text{He}^*$.

Elastic collisions do not only play an important role in the realization of ultracold gases, almost the total dynamic behaviour of the atomic gases can be ascribed to the collisional interactions between atoms. For most of the elements investigated in this regime so far, the elastic collisions dominate over the inelastic collisions. The importance of elastic collisions manifests itself in a special way for Bose-Einstein condensates. The formation of a Bose-Einstein condensate, its stability and coherence time, the superfluid behaviour and the application of Bose-Einstein condensates for non-linear optics depend crucially on the elastic collisional properties [4, 10, 11, 27, 28, 29].

In some atomic systems, it is possible to manipulate the collisional properties using external fields. Mostly the existence of a special scattering resonance - Feshbach resonance - is used. Depending on the applied magnetic field, the size of the elastic cross section can be changed, thus allowing one to create a cold gas in which strong interactions are either present or totally absent [12]. With these Feshbach resonances ultracold molecular quantum gases have been realized. Here, one could create dimers consisting of bosonic [30] or fermionic atoms [31]. The possibility to create molecules from ultracold fermionic atoms was used to create for the first time molecular Bose-Einstein condensates [32, 33, 34, 35]. The BEC-BCS transition was examined in detail [36, 37, 38, 39, 40, 41] and superfluidity has been proved [42]. More recently, the interactions between mixtures of bosonic and atomic atoms were examined [43, 44, 45, 46, 47, 48, 49]. A degenerate mixture of two bosonic isotopes [50, 51] and the creation of heteronuclear molecules has been realized as well [50].

Many of the studied phenomena in the last few years are fundamentally important. In all these studies, the observed effects depend on atomic interactions. That is why the choice of species is important. Adding new elements to the existing elements in which Bose-Einstein condensation has been reached, opens up new areas of research. Metastable atoms such as He^* and Ne^* are of special interest in this respect.

Metastable noble gases have an internal energy, which is orders of magnitude larger than the kinetic energy of trapped atoms. They are thus in an energetically unstable situation. From the metastable state ($3p[3/2]_2$ state for neon), there is a closed cooling transition to a higher lying state. This transition is perfectly suitable for laser cooling due to its linewidth. That is why metastable noble gases played an important role in laser cooling [52, 53, 54, 55] and the development of atom optics [56, 57, 58]. Many of these experiments profited from the high efficient electronic detection of metastable neon.

The high internal energy of a neutral metastable neon atom is sufficient to release an electron with high probability from a metal surface. From these electrons, a clear detectable signal can be obtained with an electron multiplier such as a micro-channel-plate (MCP) detector. Combined with optical detection methods as used in other atom species,

the range of detection possibilities is clearly extended for the noble gases in metastable states.

An important loss process in metastable noble gases is Penning ionization [59]. The high excitation energy of the metastable state is more than half the ionization energy of the atom. An inelastic collision with a second metastable noble gas atom leads to an ionization reaction. The products of the ionization reaction are a ground state atom, an ion, and an electron.

The inelastic collision rate is so high, that it long prevented the realization of a cold dense cloud of metastable noble gas atoms. This situation changed, when theoretical calculations revealed that for spin-polarized helium, the inelastic loss is probably suppressed by four orders of magnitude [60, 61]. In 2000, the suppression of Penning-ionization was experimentally observed by Herschbach *et al.* in Amsterdam [62]. One year later, Bose-Einstein condensation of metastable helium (^4He) was obtained for the first time in Paris simultaneously by two groups [63, 64]. In 2006, two groups, one in Amsterdam and the other in Canberra, obtained a Bose-Einstein condensate of metastable helium [65, 66]. The realization of a Hanbury Brown-Twiss experiment with quantum degenerate fermionic ^3He and bosonic ^4He followed soon thereafter [67].

For heavier noble gases, suppression of Penning-ionization by spin-polarization is not automatically the case, because of the different internal structure as compared to helium. The hole in the p -subshell leads to anisotropic interactions, which leads to depolarization of the collision partners during the collisions. In 1998, Doery *et al.* [68] predicted a suppression of Penning-ionization by four orders of magnitude for neon and no suppression at all for heavier noble gases. The latter was experimentally proved in xenon [69].

In neon, a suppression of Penning-ionization was indeed observed but with a suppression factor of 38(16) for ^{20}Ne and 7(5) for ^{22}Ne [70], much smaller as predicted. Although both isotopes have a rather large scattering length $-9.5(2.1)$ nm for ^{20}Ne and $+7.9_{-2.6}^{+9.0}$ nm for ^{22}Ne , the inelastic collision rate for spin-polarized atoms with $\beta(^{20}\text{Ne}) = 6.5(18) \cdot 10^{-11}$ cm³/s and $\beta(^{22}\text{Ne}) = 1.2(3) \cdot 10^{-10}$ cm³/s is still orders of magnitude larger when compared to other species. Nevertheless, first evaporation experiments on ^{22}Ne showed that an increase in phase-space density is possible.

In this thesis, we verify that the observed inelastic loss is almost entirely caused by Penning ionization. Simulations of evaporative cooling show that a 7-fold suppression of the two-body loss coefficient, or a 5-fold increase of the scattering length already suffices to reach the quantum degeneracy regime. We present experiments performed in metastable neon on the excited potential curves connecting asymptotically with the $^3\text{P}_2 + ^3\text{D}_3$ transition and the potential curves connecting asymptotically with the $^3\text{P}_2 + ^3\text{D}_2$ transition. Measurement of the two-body loss coefficient as function of the magnetic field showed us that already at moderate fields there is a field dependence of the two-body loss coefficient. With the implementation of an optical dipole trap, we were able to trap, for the first time, neon in the $^3\text{P}_0$ metastable state. From trap loss measurements, we extract the two-body loss coefficient for both ^{20}Ne and ^{22}Ne .

The layout of the thesis is as follows: We first briefly describe the experimental setup, and the preparation of magnetically trapped spin-polarized neon atoms. Of special attention

are the various detection methods applied in the measurements. Previously, a suppression of Penning ionization was observed. However, this suppression is much smaller as predicted [70]. In Chapter 3, we verify whether the observed inelastic collisions are indeed caused by Penning ionization. Compared to some of the other atomic species which already have been Bose condensed, ^{22}Ne has a large elastic collisions rate coefficient. At the same time, ^{22}Ne also has a very large inelastic collision rate coefficient. The latter hampers evaporative cooling. The questions: "How far can one get with evaporative cooling?", "Is it still possible to condense neon?" will be answered in this chapter.

Spectroscopy is a technique which allows us to probe the long range part of the molecular potentials. For the alkali-atoms, and also for metastable helium, this resulted in the precise determination of s -wave scattering lengths. In Chapter 4, we present experiments performed in metastable neon on the excited potential curves connecting asymptotically with the $^3\text{P}_2 + ^3\text{D}_3$ transition at 640.4 nm and the potential curves connecting asymptotically with the $^3\text{P}_2 + ^3\text{D}_2$ transition at 633.6 nm.

Calculations on the metastable state in earth-alkaline atoms revealed that already at moderate fields there is a field dependence of the collisional properties [71, 72]. For neon, these calculations do not exist, and it is thus unknown, whether collisional properties can be manipulated with external fields. We measured the two-body loss coefficient as function of the magnetic field, and indeed observed a dependence of the collisional properties on magnetic fields (see Chapter 5).

Neon has in addition, a second metastable state which has to our knowledge never been trapped before. With the implementation of the optical dipole trap we have managed to trap this state. This state could be an interesting candidate for Bose-Einstein condensation in neon, provided that the collisional parameters are favourable for efficient evaporative cooling. The theory, implementation of the optical dipole trap and experiments on the collisional properties of this second metastable state are presented in Chapters 6 and 7. The thesis closes with concluding remarks in Chapter 8.

Chapter 2

Experimental setup

One of the aims of this experiment is to determine whether it is possible to reach the degenerate regime with metastable neon atoms. To determine the collisional properties of metastable neon atoms, these atoms have to be slowed down and trapped. In the following sections a description of the properties of metastable neon is given, followed by a short introduction in the experimental realization of trapped metastable neon atoms. The main focus of this chapter is the determination of the atomic ensemble parameters by optical and electronic means and the preparation of magnetic trapped spin-polarized atoms.

2.1 Properties of metastable neon

There are three natural occurring Neon isotopes. Two are bosonic (^{20}Ne and ^{22}Ne) with a natural abundance of 90.48% and 9.25% and one is fermionic (^{21}Ne , abundance: 0.27%). ^{20}Ne and ^{22}Ne do not have a nuclear spin while ^{21}Ne has one of $3/2$. In Fig. 2.1, the lowest energy levels (not on scale) are given for the bosonic isotopes. Here we used the LS -notation: $^{2S+1}L_J$. The levels are ordered to the total angular momentum J . In order to get to the first excited state, one of the p -electrons from the closed $(2s)^2(2p)^6$ -shell has to be excited to the next higher lying shell. With an excitation energy of 16.6 eV most of the ionization energy of 21.6 eV is used in the process. Due to the strong spin-orbit coupling between valence electron and the remaining $(2p)^5$ -subshell, we are in the intermediate field coupling regime and the LS -notation here is not entirely correct. Therefore we have given as well the Racah notation $nl[K]_J$ with $K = J_{core} + l$ as $J = K + S$. The apostrophe behind the l stands for $J_{core} = 3/2$. With the apostrophe missing, this stands for $J_{core} = 1/2$. Two of the first excited states are metastable states. The $^3\text{P}_2$ state, with a magnetic quadrupole transition to the ground state, and the $^3\text{P}_0$ state, which decays via the $^1\text{P}_1$ state to the ground state. The remaining states with $J = 1$ are connected to the ground state by fast dipole transitions. The $^3\text{P}_2$ metastable state, magnetically trappable and with a closed cooling transition to the $^3\text{D}_3$ state at a wavelength of 640.4 nm and a linewidth of $\Gamma = 2\pi \cdot 8.18$ MHz, is very well suitable for laser cooling and trapping. The experimental most important parameters for neon are given in appendix A.

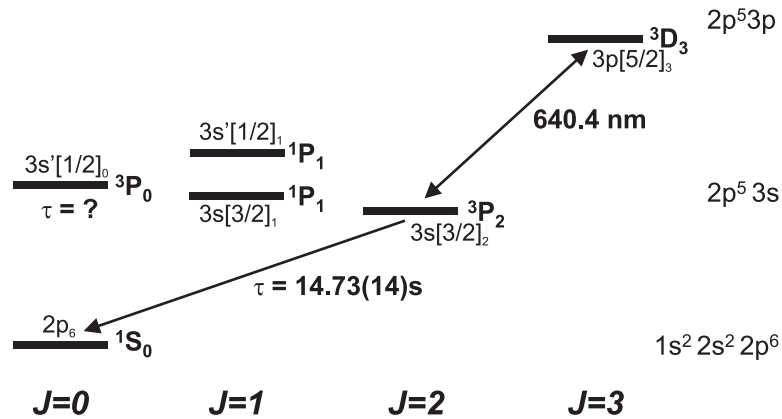


Figure 2.1: Level scheme for neon where only the lowest energy levels are given. The levels are ordered to total angular momentum J and are identified by the LS - (bold) and Racah-notation.

2.2 Overview of the experimental setup

The neon atoms, excited to the metastable state by means of an electrical discharge between the hollow cathode of the liquid nitrogen cooled neon source and the skimmer, are collimated by radiative pressure forces in laser fields with curved wavefronts. The collimated beam of metastable neon atoms is then slowed in a Zeeman slower and used to load a magneto-optical trap (MOT). After a cooling phase, the atoms are spin-polarized by optical pumping and loaded in an Ioffe-Pritchard type magnetic trap. After an one-dimensional Doppler cooling phase, the atoms can either be loaded in a crossed optical dipole trap or compressed and cooled down further using rf-forced evaporative cooling. Switching off the trap, the atoms are detected either as a time-of-flight on a double micro-channel plate detector or by absorption imaging. A schematic overview of the setup is given in Fig. 2.2. In the following sections, the different parts of this setup are described.

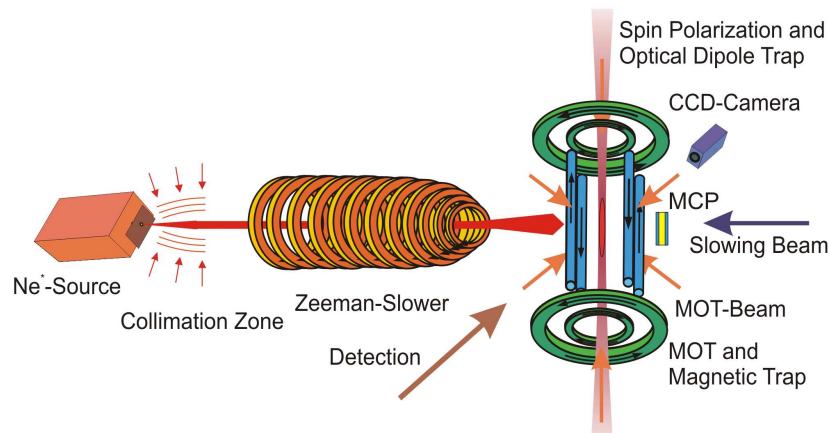


Figure 2.2: Schematic overview of the experimental setup.

2.2.1 Computer control

The experiment is controlled by three National Instruments IO-cards (*PCI-DIO-32HS*, *PCI-M10-16E-4* and *PCI-6713*) with on-board clocks, processors and memory. The timetable containing the actions and the corresponding times, which have to be performed subsequently, is loaded into the memory of the cards. During an experimental cycle, one of these cards triggers the others allowing the execution of these actions and their corresponding timing in real time with a time resolution of $2 \mu\text{s}$. With the digital (TTL) outputs various acousto-optic modulators (AOMs), mechanical shutters (atomic and laser beams), current switches (IGBTs), Zeeman slower coils and as well the camera trigger and triggering of the digital oscilloscopes are controlled. The currents for the MOT and magnetic trap, also the intensity and frequency for the MOT, Doppler cooling and spin polarization beams are controlled with the analog outputs. With an additional GPIB-card the rf signal generator is programmed for forced evaporative cooling. The computer card system is addressed by the LabVIEW program.

2.2.2 Laser systems

Dye laser

For the manipulation of atoms in the $^3\text{P}_2$ metastable state only one laser at a wavelength of 640.4 nm is needed. The corresponding frequency shifts needed in the different parts of the setup are obtained with AOMs. The laser light is created with a dye laser (*Coherent 699-21*) pumped by a frequency-doubled Nd:YVO4 laser (*Coherent Verdi V10*). The dye used here is Sulforhodamin B (*Kiton Red 6200*). With an output power of 2.1 W at a pump power of 10.5 W, there is plenty light to run the experiment (typically 1.3–1.5 W). The laser is locked on its temperature stabilized cavity and for long time stability, locked onto the $^3\text{P}_2$ – $^3\text{D}_3$ transition by Doppler free saturation spectroscopy. The light needed for the saturation spectroscopy is obtained by reflecting a part of the laser beam using a single-side anti-reflection coated substrate. From this light two parallel beams with both approximately 4% of the intensity are obtained by reflection on a thick substrate. The transmitted part of the beam goes through a double-pass AOM and is shifted +520 MHz. It is then sent, from the side where the photodiodes are located over a partially reflecting substrate, through a rf-discharge in a neon filled glass cell. With an intensity $I \approx 1 - 2I_{sat}$ with I_{sat} the saturation intensity, it saturates the atomic transition and is therefore called "pump beam". The two parallel beams are also sent through the glass cell, but from the opposite direction (Fig. 2.3). One of these beams is overlapped with the pump beam and is called "probe beam". The signal of this probe beam shows a Doppler broadened spectrum with the Lamb dips for neon when the laser is scanned over a large frequency range. The signal of the other beam shows only a Doppler broadened spectrum. Instabilities in the laser intensity or rf-discharge, mechanical vibrations but mostly the Doppler background appear in the same extent for both beams. By subtracting the currents of both photodiodes, one obtains a background free Lamb dip, which can then be amplified. To lock the laser at the Lamb dip, the pump laser is frequency modulated at a frequency of 6 kHz with a

modulation depth $\Delta\nu$ of typical 1 – 2 MHz (Marconi 2019A). The detected photodiode signal is amplified and frequency demodulated by a Lock-In amplifier. The obtained error signal is connected via a PI-controller to the external frequency control input of the dye laser and by this, the dye laser is locked at -260 MHz relative to the atomic transition.

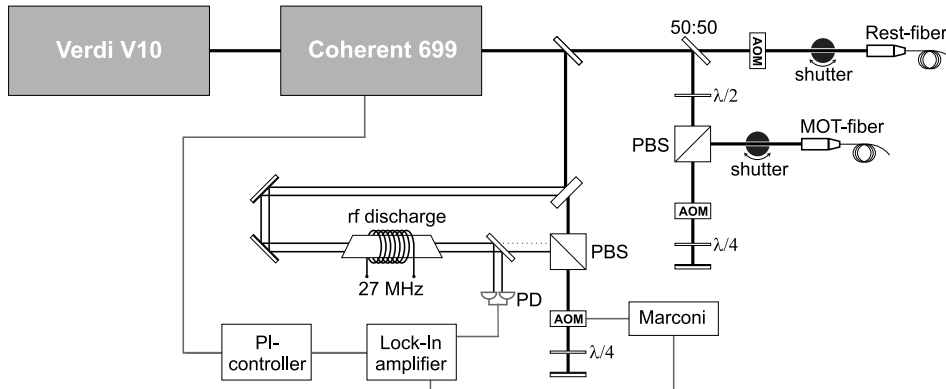


Figure 2.3: Schematic overview of the laser stabilization and the splitting of the laser beam into two beams. The "MOT" laser beam first passes a double-pass AOM in order to adjust both the frequency and the intensity of the MOT beams. The "Rest" laser beam passes a single-pass AOM, which shifts the frequency by $+130$ MHz. These beams are then sent via single-mode fibers to the experimental setup (Fig. 2.4).

Home-build dye laser

A second dye laser was also at our disposal. This home-build dye laser, pumped by an argon ion laser (Coherent INNOVA 200 Series) with 6.4 W output power, was used for those measurements described in this theses which required two strongly different laser wavelengths. It delivers an output power of 0.6 W at 640 nm. Locked to its external reference cavity, this laser has a linewidth of 4 MHz. For the long time stability, the laser is locked on an atomic transition by Doppler free saturation spectroscopy as described above. However, depending on the type of measurement, the laser could also be tuned without mode hop over a range of 20 GHz (see Chapter 4). With a single-mode fiber, the laser light is transferred to the vacuum chamber and aimed at the atomic cloud.

2.2.3 Optical setup

The laser light from the Coherent dye laser is split into two beams. The "MOT" laser beam first passes a double-pass AOM in order to obtain and control both the frequency and the intensity of the MOT beams while the "Rest" laser beam passes a single-pass AOM, which shifts the frequency by $+130$ MHz. With mechanical shutters placed before the fiber incouplers, the beams can be blocked, preventing any near resonant stray light entering the vacuum chamber. The beams are then transferred by two single-mode fibers to the experimental setup. At the experimental setup, light from the MOT-fiber is first

collimated to a beam with a Gaussian width (ω_0) of 10 mm and then split into six MOT beams by half-waveplates and polarizing beam splitters (see 2.4). Light from the Rest-fiber is splitted into several beams, each with its own AOM. These beams are used for the collimation zone, optical detection, Zeeman slower as well as spin polarization and one-dimensional Doppler cooling in the magnetic trap.

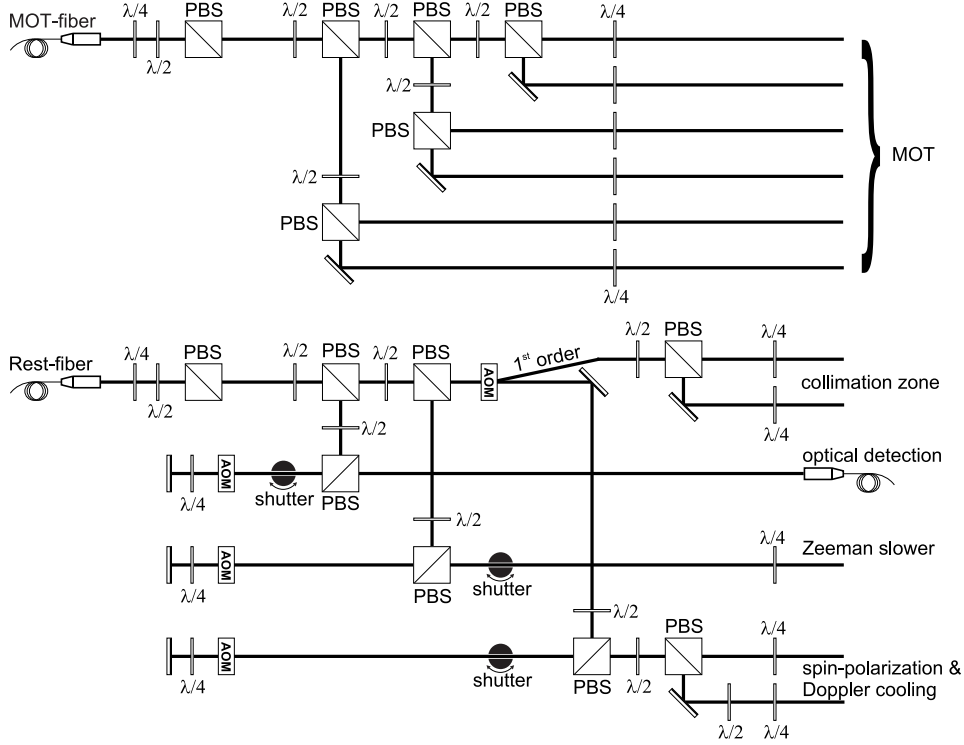


Figure 2.4: Schematic overview of the optical part of the experimental setup. Light from the MOT-fiber is split into six MOT beams by half-waveplates ($\lambda/2$) and polarizing beam splitters (PBS). Light from the Rest-fiber is split into several beams, each with its own AOM. These beams are used for the collimation zone, optical detection, Zeeman slower as well as spin polarization and Doppler cooling.

2.2.4 Collimated beam of metastable neon atoms

In order to slow down, trap and manipulate metastable neon atoms, the metastable state has to be populated. This is obtained by collisions with electrons via an electrical discharge. This discharge is stable for pressures of $p_0 \approx 1$ mbar and runs between the hollow cathode of the neon source through a nozzle of 0.3 mm diameter and skimmer (with $I = 5 - 10$ mA and $V = 0.6$ kV). Approximately a fraction of 10^{-4} of the atoms are excited to the 3P_2 metastable state with an internal energy of 16.6 eV. In order to reduce the mean velocity of the atomic beam, the neon source is cooled with liquid nitrogen. The skimmer, with a hole diameter of 1.3 mm, is approximately 6 mm away from the nozzle and selects a small part of the atomic beam. It also serves as a differential pumping stage.

The huge remaining gas ballast is pumped away by an oil-diffusion pump backed by a rotary vane vacuum pump. By this, the pressure could be kept at roughly $1 \cdot 10^{-5}$ mbar. After the source chamber, there are two more differential pumping stages before reaching the main vacuum chamber with a pressure of $1 - 2 \cdot 10^{-10}$ mbar. Both stages (i.e. additional chambers) are pumped by turbomolecular pumps. Due to the low percentage of metastable neon atoms and the long distance of 95 cm needed between the source and the main vacuum chamber, an increase in luminance of the atomic beam is advantageous. The collimation of an atomic beam is based on radiative pressure forces in laser fields with curved wavefronts [73]. The collimation zone starts directly after the skimmer and has a length of 5 cm. It is described in detail by Eva-Maria Kriener [74]. With this collimation zone, the capture angle α_c could be increased from 2.6 to 15.1 mrad in two dimensions, thereby increasing the loading rate of the MOT by a factor of 35. The last chamber before the Zeeman slower contains a mechanical shutter. This shutter prevents the atoms from entering the Zeeman slower and the main chamber and is only opened during loading of the MOT. By this, the pressure of $1 - 2 \cdot 10^{-10}$ mbar in the main vacuum chamber is substained.

2.2.5 Zeeman slower

The atoms with a main velocity of 620 m/s as created in the liquid nitrogen cooled discharge are too fast to be trapped and therefore slowed down by spontaneous light forces from a focused circular polarized counter-propagating beam. To remain resonant during this deceleration process, the Doppler shift is compensated with the Zeeman shift of the corresponding cycling transition. The Zeeman slower, build by Aydin Aclan [75], has a length of 54 cm. After this distance, the main velocity of 620 m/s is reduced to 50 m/s (for more details, see [76]). With a maximum capture velocity of approximately 50 m/s, the atoms can now be trapped in the MOT. The Zeeman slower beam crosses the MOT region and in order to not disturb it, this beam is blue detuned from the $^3P_2 - ^3D_3$ transition by $\Delta = +20\Gamma$. Unfortunately, it has still a disturbing effect on the trapped atoms and the loading rate of the MOT therefore depends sensitively on the intensity of the Zeeman slower beam.

2.2.6 Magneto-optical trap

For experiments with the aim to increase the phase-space density, an ultra-high vacuum (UHV) with a pressure in the order of 10^{-10} mbar is needed. Otherwise the lifetime of the trapped atoms is limited by the collisions with the background gas. In order to reach this pressure, the main vacuum chamber is pumped by three vacuum pumps. A turbomolecular pump with a pumping speed of 250 l/s (for N_2), an ion getter pump with a special noble gas triode (pumping speed for N_2 : 250 l/s and for neon: 20 l/s) and a titanium sublimation pump, which can be cooled with liquid nitrogen. With the titanium sublimation pump, the pressure can be reduced from $1 - 2 \cdot 10^{-10}$ mbar to below $7 \cdot 10^{-11}$ mbar. When loading of the MOT, the pressure increases by $1 \cdot 10^{-10}$ mbar, but is reduced to the steady-state value within a few seconds. The main vacuum chamber is surrounded by three

pairs of coils perpendicular to each other. These coils compensate the earth magnetic field, but can as well be used to move the position of the MOT. The principle of the MOT is based on the cooling effect by radiative pressure forces of laser light on the atoms. Superimposed with a magnetic field, the MOT combines both the cooling effect of a three dimensional optical molasse with confinement by the spatial dependence of the radiative pressure force due to the Zeeman shifts [77]. It consists of three pairs of circular polarized laser beams for the three dimensions and two anti-parallel connected coils, which produce a quadrupole magnetic field. For red detuning ($\Delta < 0$), a trapping potential is created and the atoms are cooled by the radiation pressure force. The MOT has been studied both experimentally and theoretically in depth for alkali atoms [78, 79] and as the number of trapped atoms increases, the effect of multiple scattering of the photons should as well be taken into account [80, 79]. However, we will not go into detail here, but instead merely describe the experimental realization of our MOT. The MOT consists of two anti-parallel connected coils, which serve as dipole coils in the magnetic trap (see Section 2.2.7). The symmetry axis of the dipole coils is perpendicular to the atomic beam (Fig. 2.5). The axial gradient B'_z is approximately twice as large as the radial gradients

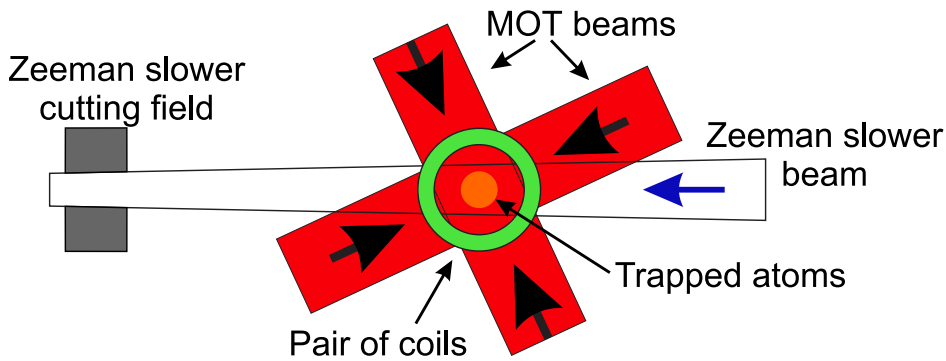


Figure 2.5: Schematic overview of the MOT along the axial direction. The optical access is limited by the Ioffe bars. To have full optical access to the trap center, the vertical beams are turned 25° from the horizontal/vertical axes.

and is typically $20 - 30$ G/cm. The MOT beams have a Gaussian intensity distribution with a width of 10 mm and are limited by a diafragma at a diameter of 22 mm to maximize the trapping volume, which is limited by the opening in the magnetic trap. The intensity ratio of the three pairs of MOT beams is 2:2:1. The lower intensity in the axial direction is compensated by the larger axial gradient and by this an isotropic ensemble is obtained. The intensity and the frequency of the MOT beams are controlled by a double-pass AOM. This allow us to change the frequency, but as well the intensity over a sufficient large range ($\Delta = -10\dots + 2\Gamma$ and $I_{total} = 0\dots 30I_{sat}$). With a capture velocity of approximately 50 m/s, the atoms from the Zeeman slower can now be trapped.

2.2.7 Magnetic trap

In this section, the magnetic trap is discussed. The magnetic trap used in this experiment is an Ioffe-Pritchard type magnetic trap and was designed and built by Martin Zinner [76].

Magnetic trapping

The atomic levels of an atoms with magnetic moment $\vec{\mu}$ and nonzero internal angular momentum, placed in an external magnetic field, are shifted. This gives rise to a potential energy

$$U(\vec{r}) = -\vec{\mu} \cdot \vec{B}(\vec{r}), \quad (2.1)$$

where \vec{B} is the magnetic field and $\vec{\mu}$ the magnetic moment of the atom. By choosing the quantization axes along the magnetic field, this energy shift can be expressed as function of m_J :

$$U(\vec{r}) = g_J m_J \mu_B B(\vec{r}), \quad (2.2)$$

with g_J the Landé factor, μ_B the Bohr magneton and m_J the magnetic substate, which has values between $-J$ and J . The trap region is a current free volume: $\nabla \times \vec{B} = 0$. Hence, there is no local maximum of $|\vec{B}|$ and only low-field seeking states (states with $g_J m_J > 0$) can be trapped in the magnetic field minima. The atoms are, however, only trapped if they - in their frame of reference - stay in the same magnetic substate during their motion in the magnetic trap. They should be able to change their direction of the magnetic moments $\vec{\mu}$ via Larmor precession to the local direction of the magnetic field $B(\vec{r})$, otherwise they undergo Majorana spin-flip transitions and are lost. The Larmor frequency ω_L should be larger than the rate of change of the magnetic field direction:

$$\omega_L = g_J m_J \mu_B B(\vec{r}) / \hbar \gg \left| \frac{d \vec{B}(\vec{r})}{dt B(\vec{r})} \right|. \quad (2.3)$$

At vanishing magnetic fields, this is no longer the case and the atoms are lost.

Ioffe-Pritchard trap

The Ioffe-Pritchard trap consists of a two-dimensional quadrupole field in the x, y -plane with a perpendicular on this plane dipole field together with a homogeneous field. The quadrupole field is produced by four bars parallel to the z -axis, where the neighboring bars carry opposite currents. The axial dipole field and the axial homogeneous field are produced by the two pairs of coils with the currents flowing in the same direction. A schematic view of the trap is given in Fig. 2.6. The resulting magnetic field is described by:

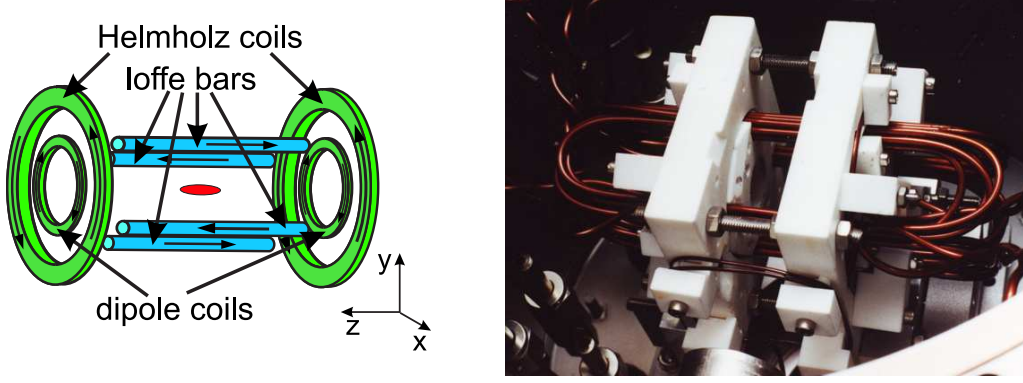


Figure 2.6: Left-hand side: Ioffe-Pritchard configuration. Right-hand side: Picture of the magnetic trap. The coils and bars are created from hollow copper tubes carried by the two Marcor plates. Between the Marcor plates, the Ioffe bars can be seen. At the front side, one sees the rf-antenna with two windings. The trap is water cooled through the hollow copper tubes.

$$\vec{B}(\vec{r}) = B_0 \begin{pmatrix} 0 \\ 0 \\ 1 \end{pmatrix} + B' \begin{pmatrix} x \\ -y \\ 0 \end{pmatrix} + \frac{B''}{2} \begin{pmatrix} -xz \\ -yz \\ -z^2 - \frac{1}{2}(x^2 + y^2) \end{pmatrix} \quad (2.4)$$

and depends on the radial gradients $B' = \partial_x B_x$ at $z = 0$, the radial curvature $B'' = \partial_z^2 B_z$ and the contribution of the offset field B_0 obtained from the difference of the axial fields. The magnetic field grows quadratic in the axial direction. In the radial direction it starts quadratic and grows linearly for larger distances from the trap center. The trap depth is limited by four saddle points [76].

Trap potential For small displacements from the trap center, the trap potential $U(\vec{r})$ can be approximated by a Taylor expansion of $\vec{B}(\vec{r})$ to the position coordinates. Putting the potential minimum at $U = 0$, one gets

$$U(x, y, z) = \frac{1}{2}m\omega_{ax}^2 z^2 + \frac{1}{2}m\omega_{rad}^2(x^2 + y^2) + \frac{1}{2}m\omega_{ax}^2 \frac{B'}{B_0}(y^2 - x^2)z + \mathcal{O}(4), \quad (2.5)$$

where the trap frequencies depend on the offset field B_0 , the gradient B' and curvature B'' of the magnetic field [81]:

$$\omega_{ax}^2 = \frac{g_J m_J \mu_B}{m} B'' \quad (2.6)$$

$$\omega_{rad}^2 = \frac{g_J m_J \mu_B}{m} \left(\frac{B'^2}{B_0} - \frac{B''}{2} \right). \quad (2.7)$$

If the third order terms can be neglected, then the potential is cylindric symmetric along the axial direction of the trap. The harmonicity in the radial direction is created by the

superimposition of the linear radial quadrupole field with the axial offset field. The trap is harmonic only for small distances where the deviation of the field strength from the offset field is small ($z \ll 0.7$ cm for $B_0 = 1$ G, $B' = 200$ G/cm and $B'' = 300$ G/cm² [81]).

Density distribution The density distribution for an ideal gas in an infinitely deep trap is given by

$$n_{\text{inf}}(\vec{r}) = n_0 \exp \left[-\frac{U(\vec{r})}{k_B T} \right], \quad (2.8)$$

with $U(\vec{r})$ the trapping potential, T the temperature of the cloud, n_0 the central density and k_B the Boltzmann constant [82]. For a cylindric harmonic potential, the density is given by a Gaussian distribution

$$n_{\text{inf}}(x, y, z) = n_0 \exp \left[-\frac{x^2}{2\sigma_{\text{rad}}^2} - \frac{y^2}{2\sigma_{\text{rad}}^2} - \frac{z^2}{2\sigma_{\text{ax}}^2} \right], \quad (2.9)$$

with

$$\sigma_{\text{rad}} = \sqrt{\frac{k_B T_{\text{rad}}}{m\omega_{\text{rad}}^2}} \quad \text{and} \quad \sigma_{\text{ax}} = \sqrt{\frac{k_B T_{\text{ax}}}{m\omega_{\text{ax}}^2}}, \quad (2.10)$$

and

$$n_0 = \frac{N}{(2\pi)^{3/2} \sigma_{\text{ax}} \sigma_{\text{rad}}^2}. \quad (2.11)$$

where N is the total number of atoms. The mean density n_m is defined as

$$n_m \equiv \frac{\int d^3r n_{\text{inf}}^2(\vec{r})}{\int d^3r n_{\text{inf}}(\vec{r})} = \frac{\int d^3r n_{\text{inf}}^2(\vec{r})}{N}, \quad (2.12)$$

and for a Gaussian distribution (Eq. 2.9), the integration over the position space gives us:

$$n_m = \frac{N}{8\pi^{3/2} \sigma_{\text{ax}} \sigma_{\text{rad}}^2}. \quad (2.13)$$

Equation 2.8 is only valid for a thermodynamic equilibrium. If this is the case, there is a correlation between the potential and kinetic energy of the ensemble, given by the equipartition theorem. The mean energy per atom is given by $U_{m,\text{tot}} = 3k_B T$ and $U_{m,\text{pot}} = U_{m,\text{kin}} = \frac{3}{2}k_B T$. If there are no collisions between the atoms, the motion in a harmonic potential is not ergotic i.e. the three dimensions are uncoupled and one has to describe this ensemble with independent temperatures T_{ax} for the axial direction and T_{rad} for the radial direction. The mean temperature is given by

$$T_m = \frac{1}{3}(T_{ax} + 2T_{rad}). \quad (2.14)$$

Implementation of the Ioffe-Pritchard trap

In order to get the highest possible gradients, the magnetic trap is installed inside the main vacuum chamber. The coils and bars are wound with hollow copper tubes, isolated by a Kapton coating, and are carried by two Marcor plates. The distance between these Marcor plates, but also the distance between the neighboring Ioffe bars is 22 mm, thus giving good optical access to the trap center. The calculated trap frequencies for an offset field of 2.2 G are $\omega_{rad}/2\pi = 648$ Hz and $\omega_{ax}/2\pi = 79.9$ Hz (Table 2.1 together with Eq. 2.6 and 2.7). This is achieved for a current of 230 A flowing through all coils. The

Table 2.1: *Contribution of the different coils to the offset field, gradient and curvature [76]. Parameters for $I = 230$ A are given in bold.*

Coils	Parameters
2D quadrupole	$B' = I \cdot 0.913 \text{ G/cmA} = \mathbf{210 \text{ G/cm}}$
Dipole	$B'' = I \cdot 1.478 \text{ G/cm}^2\text{A}$ $B_0 = I \cdot 1.7596 \text{ G/A}$
Helmholtz	$B'' = I \cdot 0.168 \text{ G/cm}^2\text{A}$ $B_0 = I \cdot 1.7500 \text{ G/A}$
Dipole and Helmholtz	$B'' = I \cdot 1.310 \text{ G/cm}^2\text{A} = \mathbf{301 \text{ G/cm}^2}$ $B_0 = I \cdot 0.0096 \text{ G/A} = \mathbf{2.2 \text{ G}}$
Dipole with antiparallel currents	$B'_z = I \cdot 1.491 \text{ G/cmA}$
Helmholtz with antiparallel currents	$B'_z = I \cdot 0.660 \text{ G/cmA}$

coils are cooled by water pushed through these hollow tubes at a pressure of 8 – 10 bar. The current source for this magnetic trap is the *HP 6682A* with a maximum current output of 233 A and a maximum voltage of 22 V. For the magnetic trap configuration, the dipole coils, Ioffe bars and Helmholtz coils are connected in series. To be flexible, IGBTs have been built in as well. The corresponding electronic circuit is given Fig. 2.7. It allows us to create the different trap geometrics for the MOT, magnetic trap and optical pumping. The induction voltage obtained during switching of the IGBTs is limited by the Varistors connected parallelly to the IGBTs. By this, switching times of 30 μs could be achieved. However, the disappearance of the magnetic fields (2 – 4 ms) takes longer due to the induced eddy currents in the stainless steel vacuum chamber [81]. Two MOSFET plates, each with 100 MOSFETs, are used to control the currents. One of these MOSFET plates (MF1) is used to control the total current through the coils. With the other MOSFET plate (MF2), the current through the Helmholtz coils can be adjusted, allowing us to control the offset field of the magnetic trap. Thus, we are able to go from offset fields of 2 G to 50 G (Chapter 5). Both the IGBTs and the MOSFET banks are connected to the National Instruments IO-cards and are controlled by LabVIEW.

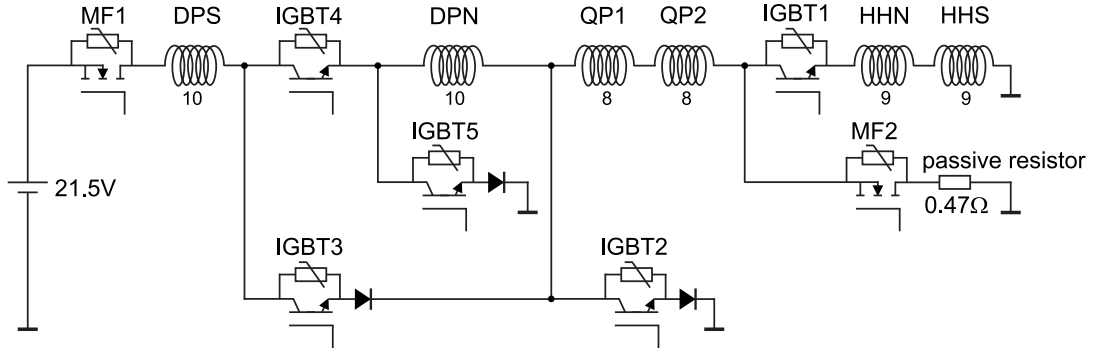


Figure 2.7: Electronic circuit to control and switch the magnetic trap. DPN/S stands for dipole coils north/south, HHN/S for Helmholtz coils north/south and QP for the quadrupole fields. The passive resistor (0.47Ω) is chosen so that for a total current of 230 A and a fully conducting MF2 we have $B_0 = 26$ G. For each coil, the number of windings are given as well.

2.2.8 Evaporative cooling

Evaporative cooling is mostly used to increase the phase-space density of trapped atoms. Nevertheless, it requires a method, which truncates the energy distribution of the trapped atoms at a variable energy ϵ_{trunc} . Therefore, perpendicular on the trap geometry, a rf-antenna has been installed (Fig. 2.6, right-hand side). It consists of two square windings with an edge length of 5 cm. The radio frequencies are generated by a signal generator (*Rohde & Schwarz SMG*) and amplified with a 10 W amplifier. The signal generator is connected to a GPIB-card and can be programmed with LabVIEW. The linear polarized rf field orthogonal to the trapping magnetic field induces position depending spin-flip transitions ($\Delta m = 1$). In the ideal case, all atoms with an energy above this truncation energy are effectively removed from the ensemble by the adiabatic transitions from the $^3P_2(m = +2)$ to the $^3P_2(m = 0, -1, -2)$ magnetic substates. If this process is efficient, the trap depth is reduced to ϵ_{trunc} . The energy at which these spin-flips occur depends on the offset field B_0 of the magnetic trap and the rf frequency ν_{RF} applied:

$$\epsilon_{trunc} = h\nu_{RF} - \frac{3}{2}\mu_B B_0, \quad (2.15)$$

2.3 Determination of the atomic ensemble parameters

For the investigation of a trapped atomic ensemble, it is important to know the characteristic parameters. Only then one is able to obtain information about the physics behind processes such as collisions. Characteristic parameters are the number of atoms, temperature and size of the atomic cloud. Together with the trap parameters one can then for example determine the density distribution in an optical dipole trap (Chapter 6 and 7). The size is obtained from the Gaussian width of the ensemble, the temperature from

expansion of the atomic cloud. In general it is assumed that the velocity distribution is described by a Maxwell-Boltzmann distribution. In the following sections, three detection methods are introduced. Two of these methods are based on optical detection (fluorescence and absorption imaging). The other method is based on electronic detection by an electron multiplier. Here we used a micro-channel plate (MCP).

2.3.1 Optical detection

For the optical detection, a 12-bit CCD Camera (*Sensys 1400E, Photometrics*) is used. The CCD-chip has a resolution of 1500×1035 pixels, a pixel size of $6.8 \times 6.8 \mu\text{m}$ and a quantum efficiency of 60% for $\lambda = 640 \text{ nm}$. The atomic cloud is focused on the camera from above so that the axial and the radial size of the atomic cloud are imaged on the CCD-chip. For focusing the atomic cloud on the CCD-chip, a commercial telescope (*MINOLTA MD Macro-Objective 100 mm*) is used. The calibration factor with this commercial telescope is $16.5 \mu\text{m}/\text{pixel}$. The distance of the CCD-chip to the trap center is approximately 47 cm. For the detection of the atoms in the trap, both fluorescence and absorption imaging can be used.

Fluorescence imaging

Fluorescence imaging is the only method that does not disturb the atoms in a magneto-optical trap and allows one to observe the atomic cloud for a longer time. If the optical density of the atomic cloud is low, there is a linear relation between the scattered photons and the number of atoms. To determine the absolute number of atoms, the detuning, laser intensities, but as well the detection efficiency of the optical detection system should be known. In addition, a model describing the spontaneous emission in the MOT and taking into account the different levels and velocity components of the atoms has to be applied. We used this detection method mostly for the optimization of the collimation zone and the positioning of the source.

Absorption imaging

Unlike fluorescence imaging, absorption imaging is based on the relative transmitted light through an atomic ensemble. This is achieved by irradiating the atoms from below and measuring the transmitted light with the camera. Due to the small viewing angle, only a negligible fraction of the scattered light is detected by the camera. By dividing the irradiation with atoms by the irradiation without atoms, a relative absorption is obtained. The advantage of this method is that for low intensities $I \ll I_{sat}$ the absolute value of the intensity I is not needed to obtain the absolute number of atoms. It is also not critical to small intensity fluctuations. Another advantage is that the overall detection efficiency of the optical detection system is not important. This method only measures the density distribution in two dimensions. Since the density distribution is in good approximation described by a Gaussian function and we have a cylindrical density distribution, it is

sufficient to determine the radial size in one direction. The intensity, which is absorbed on its way through the atomic cloud, is described by the absorption rate multiplied with the density [83]:

$$\frac{dI(y)}{dy} = -\frac{\Gamma}{2}\hbar\omega \frac{I(y)/I_{sat,lin}}{1 + I(y)/I_{sat,lin} + 4(\Delta/\Gamma)^2} \cdot n(x, y, z), \quad (2.16)$$

with $I_{sat,lin}$ the saturation intensity for linear polarized light, Γ the spontaneous emission rate, ω the transition frequency, $n(x, y, z)$ the density distribution and Δ the detuning from atomic resonance. Here the velocity of the atoms is neglected. For $\Delta = 0$ and $I \ll I_{sat}$, this equation simplifies to

$$\frac{dI(y)}{dy} = -\frac{\Gamma}{2}\hbar\omega \frac{I(y)}{I_{sat,lin}} \cdot n(x, y, z), \quad (2.17)$$

and after integration, one obtains

$$n_{col} = \frac{2AI_{sat,lin}}{\hbar\omega\Gamma} \ln \left(\frac{I_{det}(0)}{I_{det}(n_{col})} \right), \quad (2.18)$$

with $I_{det}(0)$ the detected intensity without atoms, $I_{det}(n_{col})$ the intensity with atoms and A the pixel area $d \times d$ [81]. With x, z spanning the horizontal plane and y accounting for the vertical direction (See Fig. 2.6), the column density n_{col} is defined as:

$$n_{col} \equiv \int_{-d/2}^{d/2} dx \int_{-d/2}^{d/2} dz \int_{-\infty}^{+\infty} dy n(x, y, z). \quad (2.19)$$

The absorption image containing the column densities is integrated over the axial and radial direction and fitted with a Gaussian function. From these fits, the number of atoms and the radii of the density distribution are obtained. The temperature of the cloud is determined by a time-of-flight measurement.

Time-of-flight

After switching off the trap, the disappearance of the magnetic fields takes place in the order of 2 – 4 ms and influences the atomic transition for absorption imaging. To overcome this, the absorption images are taken after a certain expansion time in which the ensemble expands freely due to the velocity distribution and is accelerating downwards due to gravity. For an initial Gaussian density distribution, this expansion is also Gaussian and the width after a certain time-of-flight (TOF) is given by

$$\sigma_i^2(t) = \sigma_{i,0}^2 + \frac{k_B T_i}{m} t^2, \quad (2.20)$$

with $\sigma_{i,0}$ the initial Gaussian width of the density distribution and T_i the temperature in the corresponding dimension. By measuring the width for different expansion times, the temperature and initial Gaussian width are obtained. Together with the number of atoms, one can then calculate the mean density with Eq. 2.13. For high densities (i.e. small cloud size), the determination of the radii gets inaccurate since the contribution of the initial width to the total width becomes small and the expansion is mostly described by the velocity distribution. For the magnetic trap, the initial size is given by (Eq. 2.10)

$$\sigma_{i,0} = \sqrt{\frac{k_B T_i}{m \omega_i^2}}. \quad (2.21)$$

Substituting this relation in Eq. 2.20 gives the following relation

$$\sigma_i^2(t) = \frac{k_B T}{m \omega_i^2} (1 + \omega_i^2 t^2) = \sigma_{i,0}^2 (1 + \omega_i^2 t^2). \quad (2.22)$$

Thus if the trap frequencies are known, one measurement suffices to determine both density and temperature of the atomic ensemble.

2.3.2 Electronic detection

The high internal energy of a neutral metastable neon atom (16.6 eV) is sufficient to release an electron with high probability from a metal surface. This enables us to detect the atoms by electronic means such as a micro-channel-plate (MCP) detector. The MCP detector has a high sensitivity and is therefore extremely useful to detect low number of atoms, but as well ions produced by Penning ionization between metastable neon atoms or by collisions with the background gas. The surface electrons released from the metal surface by impact of a metastable neon atom, create an avalanche of electrons, thus amplifying the signal. The MCP detector in the experimental setup is a double MCP (*MCP-MA25, TOPAG GmbH*) in Chevron configuration. It has an active diameter of 18 mm and is operated at a voltage of -1.8 kV (-0.9 kV per plate). The amplification factor per atom for this setting is around $10^5 - 10^6$ electrons. The MCP detector is located 13.9 cm below and with its center 2.7 cm sideways (in the radial direction) of the trap center allowing optical access to the detection beam for absorption imaging. Directly in front of the MCP detector there is a grid followed (in the outwards direction) by an aperture electrode. Putting a positive voltage on the aperture electrode, ions are repelled and only the neutral atoms fall on the MCP detector. For the detection of neutral atoms, we put the aperture electrode at a voltage of $+2.4$ kV. The grid is put at a voltage of -2.1 kV. This prevents the electrons released by collisions of the ions with the metal surface of the aperture electrode to reach the MCP detector. Another advantage is that secondary electrons released from the MCP surface by impact of neutral metastable atoms missing the micro-channels are accelerated back towards the MCP, thus increasing the efficiency. The electron pulses are detected by an electric isolated anode at the backside of the MCP. We operated the MCP detector in the current modus. The recorded TOF signal on the MCP detector, af-

ter switching off the trap, gives us information about the temperature and the number of atoms initially trapped (Fig. 6.6 for a typical TOF signal). The TOF signal is proportional to the flux of atoms through the active surface of the MCP detector as function of time

$$I(t) = \int_{\text{surfaceMCP}} \vec{J}(\vec{x}, t) \cdot d\vec{\sigma}, \quad (2.23)$$

with $d\vec{\sigma}$ an infinitesimal surface vector. With the coordinate system defined in Fig. 2.6, the MCP detector is positioned in the horizontal x, z -plane so that $d\vec{\sigma} = \hat{e}_y \cdot d\sigma$. The atom current density vector $\vec{J}(\vec{x}, t)$ is defined as

$$\vec{J}(\vec{x}, t) = \int \rho(\vec{x}, \vec{v}, t) \cdot \vec{v} d^3v, \quad (2.24)$$

with $\rho(\vec{x}, \vec{v}, t)$ the probability density for finding an atom at time t , at the location \vec{x} and with velocity \vec{v} . This is determined by the initial distribution of coordinates and velocities of the atoms $\rho(\vec{x}_0, \vec{v}_0, 0) d^3\vec{x}_0 d^3\vec{v}_0$ and the trajectories \vec{X}, \vec{V} of the free falling atoms

$$\rho(\vec{x}, \vec{v}, t) = \int d^3\vec{x}_0 \int d^3\vec{v}_0 \rho(\vec{x}_0, \vec{v}_0, 0) \delta^3(\vec{X}(t) - \vec{x}) \delta^3(\vec{V}(t) - \vec{v}), \quad (2.25)$$

with the trajectories and velocities are given by $\vec{X}(t) = \vec{x}_0 + \vec{v}_0 t - \frac{1}{2} \vec{g} t^2$ and $\vec{V}(t) = \vec{v}_0 - \vec{g} t$. For a localized density distribution $n_0(\vec{x}_0)$ and a Maxwell-Boltzmann distribution for the velocity of the atoms, the probability density at $t = 0$ is given by

$$\rho(\vec{x}_0, \vec{v}_0, 0) = n_0(\vec{x}_0) \left(\frac{m}{2\pi k_B T} \right)^{3/2} \exp \left[-\frac{m \vec{v}_0^2}{2k_B T} \right]. \quad (2.26)$$

Since the distance between the trap center and the MCP detector is large compared to the size of the atomic cloud, one can approximate the density distribution $n_0(\vec{x}_0) d^3\vec{x}_0$ by $N \delta^3(\vec{x}_0) d^3\vec{x}_0$ or simply $\delta^3(\vec{x}_0) d^3\vec{x}_0$ for $N = 1$. This gives us the following expression for the atom flux:

$$I(t) = \left(\frac{m}{2\pi k_B T} \right)^{3/2} \exp \left[-\frac{m}{2k_B T} \left(\frac{y_{MCP}}{t} + \frac{1}{2} g t \right)^2 \right] \left(\frac{y_{MCP}}{t^4} - \frac{1}{2} \frac{g}{t^2} \right) \cdot A(t), \quad (2.27)$$

with

$$A(t) = \int_{\text{surfaceMCP}} \exp \left[-\frac{m}{2k_B T} \left(\frac{x^2}{t^2} + \frac{z^2}{t^2} \right) \right] dx dy. \quad (2.28)$$

The integral $A(t)$ can be calculated for the circular surface of the MCP detector using Bessel functions. Taking instead a quadratic surface for the MCP detector (it hardly makes

a difference), the integral $A(t)$ can then be expressed by the available error functions in the fitting routines

$$A(t) = \frac{\pi k_B T t^2}{m} \operatorname{erf} \left(\frac{l}{2} \sqrt{\frac{m}{2k_B T t^2}} \right) \cdot \left[\operatorname{erf} \left(\left(\frac{l}{2} + x_{MCP} \right) \sqrt{\frac{m}{2k_B T t^2}} \right) - \operatorname{erf} \left(\left(-\frac{l}{2} + x_{MCP} \right) \sqrt{\frac{m}{2k_B T t^2}} \right) \right], \quad (2.29)$$

with $l = \sqrt{\pi R_{MCP}^2}$ the dimension of the effective quadratic MCP surface [74, 83]. The Ioffe bars and the bolts, keeping the Marcor plates together, impose geometrical constraints on the atom trajectories. The effect of these geometrical constraints on the TOF signal was numerically simulated and the effect is so small that the analytic solution for the TOF signal is still valid. We can detect atomic ensembles down to temperatures of $\sim 3 \mu\text{K}$. For lower temperatures, the expansion gets so slow that a large fraction of the atoms simply miss the MCP detector entirely (Fig. 2.8). To obtain the total number of

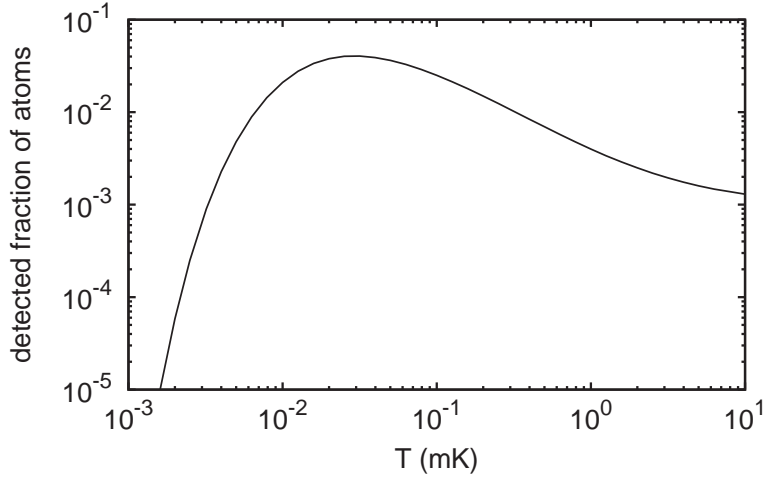


Figure 2.8: *Fraction of trapped atoms detected on the MCP for different temperatures.*

atoms initially trapped, one needs to know the number of electrons released per atom. Since the TOF signal is proportional to the flux of atoms and we are only interested in the initial number of atoms in the trap, it is reasonable to calibrate the MCP current by absorption imaging. The calibration factor obtained is $3.8(3) \cdot 10^7 \text{ V}^{-1}$ (January 2007) with a conversion factor of 10^6 V/A .

2.4 Preparation of magnetic trapped spin-polarized atoms

In earlier works, the preparation of magnetic trapped spin-polarized atoms was critical and time consuming. By the implementation of the Doppler cooling phase in the mag-

netic trap, the loading sequence simplified and became more reliable [81]. The one-dimensional Doppler cooling in the magnetic trap is achieved with two counter propagating σ^+ -polarized laser beams and it only works for higher offset fields. At high offset fields B_0 , the depolarization transitions ${}^3P_2(m = +2) \rightarrow {}^3D_3(m' < +3)$ are suppressed and only the ${}^3P_2(m = +2) \rightarrow {}^3D_3(m' = +3)$ polarization conserving transition is driven. For example, at a detuning of $-\frac{1}{2}\Gamma$ in respect to the Zeeman shifted level and for offset fields $B_0 \geq 20$ G, the rate of depolarizing transitions is suppressed by at least a factor of 10^2 [81]. With the two counter propagating laser beams along the axial direction of the magnetic trap, the cloud is cooled in this direction by Doppler cooling. For an optically dense cloud of atoms, the scattered photons are reabsorped resulting in an indirect cooling of the atomic cloud in the radial direction as well. The theoretically minimum reachable axial temperature is $T_{ax,min} = 0.7 \cdot T_D$ [84].

Loading the MOT Loading of the MOT takes 400 ms for ${}^{20}\text{Ne}$ and 700 ms for ${}^{22}\text{Ne}$. Already in this short period, the MOT is in equilibrium and limited by Penning-ionization. The detuning of the MOT light during this loading phase is -4.9Γ with a total intensity $I_{tot} = 1.53I_{sat}$ and a magnetic field gradient $B'_z = 18$ G/cm. The Zeeman slower beam crosses the MOT region and is $+20\Gamma$ detuned in order to minimize the effect on the loading of the MOT. The effect is, however, not negligible. The number of atoms in the MOT depends sensitively on the intensity of the Zeeman slower beam and has its optimum at an intensity of $0.56I_{sat}$. For the offset of the Zeeman slower a current of 45.5 A is needed. Furthermore, we need for the parabola ("Parabelfeld"), spatially varying fields 1 & 2 and for the extraction coils currents of 3.0, 2.8, 2.0 and 35.0 A. With these parameters, we trap $6 \cdot 10^8$ atoms (${}^{20}\text{Ne}$) or $3 \cdot 10^8$ atoms (${}^{22}\text{Ne}$) in the MOT at a temperature of 1 – 2 mK. After the loading sequence, the atomic beam is blocked and the Zeeman slower is switched off.

Compression The MOT loading phase is followed by a 40 ms phase in which the magnetic field gradient but also the detuning and intensity are increased to 25 G/cm, -6.9Γ and $2.60I_{sat}$. To assure an efficient loading of the magnetic trap, the atomic cloud is compressed by increasing the magnetic field gradient to 39 G/cm. The detuning and the intensity are decreased to -2.3Γ and $0.11I_{sat}$. After this 20 ms compression stage, the atomic cloud has a Gaussian width of ~ 1.2 mm and a temperature of typically 0.5 mK.

Optical pumping Only the low-field seeking states ($m = +1, +2$) can be trapped in the magnetic trap. If one transfers the atoms directly to the magnetic trap, the transfer efficiency would be limited to 40%. In order to increase this efficiency, the atoms are at first optically pumped to the ${}^3P_2(m = +2)$ state by means of two in axial direction counter propagating σ^+ -polarized beams. These beams, limited by geometrical constraints, are 1 degrees tilted with regard to the axial direction of the trap. Switching on the magnetic field (4.8 G), defining the quantization axis, followed by a 100 μs pump pulse with a detuning of $+2.36\Gamma$ and a total intensity of $0.20I_{sat}$ results in a fully spin-polarized ensemble.

Transfer and Doppler cooling The magnetic trap is then switched on, followed by a waiting time of 5 ms in which the atoms can adjust to the potential with $B_0 = 8.4$ G, $B' = 67$ G/cm and $B'' = 96$ G/cm². This step is optimized for maximum number of atoms ($4.5 \cdot 10^8$, ²⁰Ne). The trap is then compressed to $B_0 = 26$ G, $B' = 211$ G/cm and $B'' = 305$ G/cm² by a linear increase of the control voltage for MF1 from 0 to +10 V in 2 ms (gives an exponential increase in the current by the non-linear response of the MOSFETs) while keeping the control voltage for MF2 constant at +10 V. The compression stage is followed by an 80 ms one-dimensional Doppler cooling phase. With $\Delta = -0.27\Gamma$ (for $B_0 = 26$ G) and $I_{tot} = 6.3 \cdot 10^{-3} I_{sat}$, we end up with a magnetic trapped fully spin-polarized ensemble in the ³P₂($m = +2$) state with $\sim 4.5 \cdot 10^8$ atoms at a mean temperature of 0.45 mK and a mean density of $8.6 \cdot 10^{10}$ cm⁻³.

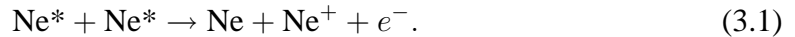
Chapter 3

Collisional parameters of metastable neon

The elastic and inelastic two-body collisions of cold spin-polarized neon atoms in the metastable $^3P_2(m_J = +2)$ state for ^{20}Ne and ^{22}Ne were previously measured in a magnetic trap [70]. From particle loss, we determined a loss parameter of inelastic collisions $\beta = 6.5(18) \cdot 10^{-12} \text{ cm}^3/\text{s}$ for ^{20}Ne and $\beta = 1.2(3) \cdot 10^{-11} \text{ cm}^3/\text{s}$ for ^{22}Ne . Whereas from cross-dimensional relaxation measurements, we obtained the elastic scattering lengths $a = -180(40)a_0$ for ^{20}Ne and $a = -150_{-50}^{+80}a_0$ for ^{22}Ne , where $a_0 = 0.0529 \text{ nm}$.

3.1 Ionization rate

The high excitation energy of the metastable state of 16.6 eV is more than half the ionization energy of 21.6 eV. An inelastic collision with a second metastable neon atom, can therefore lead to an ionization reaction, known as Penning ionization [59]



The products of the ionization reaction are a ground state atom, an ion and an electron. The ionization reaction in the collision is described by the exchange process (see Ref. [68] and the references therein) in which the valence electron of one atom fills the electron hole in the $(2p)$ -shell of the other atom. The valence electron is thereby ejected with excess energy. Since the ground state atoms are not trapped, both atoms are lost in this process. To verify whether the observed inelastic collisions are indeed caused by Penning ionization, we measure in the same experiment the rate of ions produced in the cloud of trapped metastable neon atoms with the MCP detector and determine the number of atoms as well as the loss rate by absorption imaging. The ion rate R_{ion} is described by

$$R_{ion}(t) = -\alpha_{ion}N(t) - \frac{1}{2}\beta_{ion} \int d^3r n^2(\vec{r}, t). \quad (3.2)$$

For each ionizing inelastic collision between two metastable atoms, both atoms are lost but only one ion is produced. This is accounted for the factor of $\frac{1}{2}$ in front of the rate of ionizing inelastic collisions $\beta_{ion} \int d^3r n^2(\vec{r}, t)$ in Eq. 3.2. The large internal energy of the metastable state leads as well to Penning ionization of background gas molecules. Here only one neon atom is lost to the ground state. This loss process is given by α_{ion} . The number decay on the other hand is described by

$$\dot{N}(t) = -\alpha N(t) - \beta \int d^3r n^2(\vec{r}, t), \quad (3.3)$$

with β the two-body loss coefficient and α the one-body loss rate which includes the lifetime of the metastable state and the lifetime due to collisions with the background gas. For the detection of the ions, the aperture electrode and the grid of the MCP detector are put at a negative voltage of -2.0 kV and -2.2 kV. However, the electric field of the aperture electrode seen by the ions in this trap region is reduced since the coils around the trap region are at a small voltage thus practically grounded. The efficiency with which ions are attracted to the MCP detector and not on the aperture electrode is unknown. And since there is also the magnetic field of the trap which influences the flight path of the ions, we have to calibrate the MCP current first with respect to the ion production rate in order to verify whether the observed inelastic collisions are indeed caused by Penning ionization.

3.1.1 Calibration of the MCP

For the detection of ions, we put the aperture electrode in front of the MCP detector at -2.0 kV and the grid at -2.2 kV. The MCP detector is operated at 1.78 kV. For the calibration of the MCP current, a MOT with ^{22}Ne atoms under normal conditions was realized first then followed by a period of time of $20 \mu\text{s}$ during which the detuning of the MOT laser is switched from -6.2Γ to -3.86Γ and the intensity of the MOT laser beams is increased from $11.8 \text{ mW}/\text{cm}^2$ to $40 \text{ mW}/\text{cm}^2$. The Penning ionization rate by light assistant collisions between two metastable atoms is thereby increased. This allows us to distinguish between the ions produced due to Penning ionization of background gas molecules and Penning ionization caused by inelastic collisions between two metastable atoms. The ion current on the MCP signal anode is measured for different loading times of the MOT, thus for different number of trapped atoms to realize different densities to the trapped cloud. Putting a large positive voltage on the aperture electrode instead of the negative one, ions are repelled from the detector and the contribution of the metastable neon atoms to the MCP current is measured. This contribution is however negligibly small. By absorption imaging the total number of atoms in the cloud is determined and from fluorescence images of the MOT, the cloud radii are obtained. The rate coefficients K_{SP} and K_{SS} have been previously determined in loss measurements by Martin Zinner and Peter Spoden [81, 76]. They found $K_{SP} = 8.9(25) \cdot 10^{-9} \text{ cm}^3/\text{s}$ and $K_{SS} = 8(5) \cdot 10^{-11} \text{ cm}^3/\text{s}$ for ^{22}Ne . From these parameters and with the mean density obtained from absorption and fluorescence imaging, the ion production rates for the two different MOT parameter settings are calculated. The assumption here is that the dominant loss processes in the MOT

are the Penning ionization and laser enhanced Penning ionization. In order to obtain the ion current contribution from two-body loss only, we subtract the ion currents measured in the two MOT parameter settings. Dividing by the difference of the corresponding calculated ion production rates gives the calibration factor $1.4(3) \cdot 10^{-9} \mu\text{A} \cdot \text{s}/\text{ion}$.

3.1.2 Measurements in the magnetic trap

To verify whether the observed trap loss through inelastic collisions of cold spin-polarized neon atoms are indeed caused by Penning ionization, the magnetic trap is loaded with spin-polarized metastable neon atoms (^{22}Ne) and number decay and ion production are measured. After a 200 ms Doppler cooling phase, the atoms are cooled down to a mean temperature of 0.7 mK at an offset field $B_0 = 30$ G and we start with $\sim 1.0 \cdot 10^8$ atoms. To detect the ions, the aperture in front of the MCP detector is put at -1.8 kV and the grid at -2.0 kV. The MCP detector is operated at 1.78 kV. By putting a large positive voltage of $+2.0$ kV on the grid instead of the negative one, the contribution of the metastable neon atoms to the ion signal is measured. The number of atoms are determined from absorption images and from time-of-flight measurements the initial radii of the cloud are obtained. From number decay measurements we extract the two-body loss coefficient β using Eq. 3.3 in the analyses. Similarly we can analyse the ion production rate using Eq. 3.2. From the ion rate, corrected for the metastable atom flux, we extract α_{ion} . To obtain the ion current contribution which gives R_{2-body} : 2-body loss rate leading to ionization, the metastable atom flux and the one-body loss rate α_{ion} are subtracted from the ion current. The remaining ion current stemming from 2-body loss only is then divided by the calibration factor of the MCP current. Comparing the ion current $\beta_{ion}/2$ to the two-body loss rate from the number decay gives us the ratio of the rate of ionization loss ($\beta_{ion}n_m$) to the total rate of inelastic collisions (βn_m): $\beta_{ion}/\beta = 1.1(2)$ where the uncertainty is dominated by the calibration uncertainty of the MCP detector current. In Fig. 3.1 two-body loss rates for both the ionization loss as well as the total atom loss are given as a function of trapping time.

3.1.3 Conclusion

By measuring simultaneously the number of atoms and the rate of ions production in the cloud of trapped ^{22}Ne atoms, we have been able to establish the ratio of the rate of ionization losses ($\beta_{ion}n_m$) to the total rate of inelastic collisions (βn_m): $\beta_{ion}/\beta = 1.1(2)$ where the uncertainty is dominated by the calibration uncertainty of the MCP detector current. These measurements confirm that the observed inelastic loss is almost entirely caused by Penning ionization.

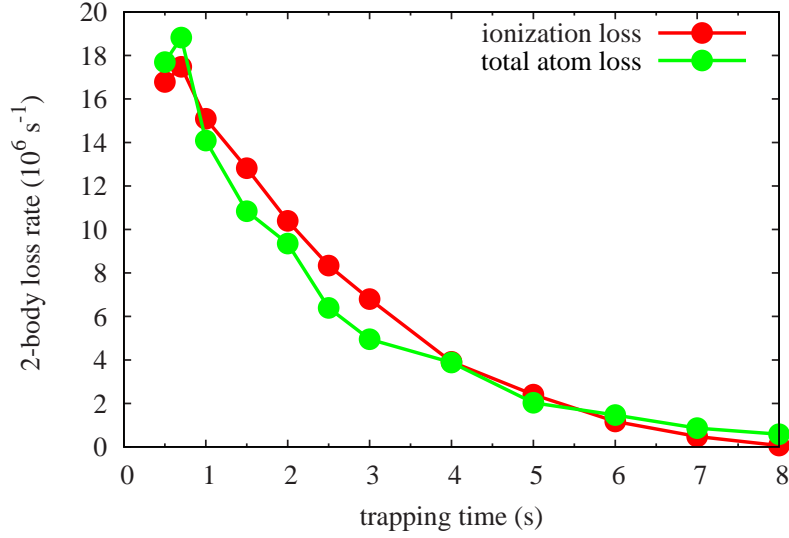


Figure 3.1: Two-body loss rate as function of trapping time. The ratio of the rate of ionizing inelastic collisions ($\beta_{ion}n_m$) to the total rate of inelastic collisions (βn_m) we obtain from these measurements is: $\beta_{ion}/\beta = 1.1(2)$.

3.2 Evaporative cooling

Evaporative cooling is mostly used to increase the phase-space density (ρ_Φ) of trapped atoms. It has led to Bose-Einstein condensation of atomic gases in 1995 [1, 2, 3]. The criteria for this phase transition is given by [85]

$$\rho_\Phi = n_0 \cdot \Lambda^3 \geq g_{3/2}(1) \approx 2.61, \quad (3.4)$$

with n_0 the peak density, $\Lambda = h/\sqrt{2\pi m k_B T}$ the de Broglie wavelength and $g_n(z) = \sum_{k=1}^{\infty} z^k/k^n$ the polylogarithm function. So far Bose-Einstein condensation has been observed with various atoms. For each of these atoms, evaporative cooling is the key technique to reach the phase transition. It is based on the removal of atoms from the high energy part of the Boltzmann distribution. Atoms with energy ϵ larger than ϵ_t leave the trap. This leads to a truncated Boltzmann distribution in the trap. In elastic collisions between trapped atoms, some atoms gain an energy larger than the trap depth and are removed. Their collision partners lost energy in the collision leading to a smaller mean energy of the trapped atoms after the elastic collision. Elastic collisions are thus the key mechanism for evaporative cooling. However, as the temperature of the gas drops, the number of atoms that leave the trap are exponentially suppressed ($\propto \exp[-\epsilon/k_B T]$) and eventually the cooling rate is balanced by competing heating mechanisms. By lowering the trap depth continuously, the evaporation can be kept going provided that the elastic collision rate stays large enough. The good-to-bad ratio R is an important number for effective evaporative cooling. It is defined as the ratio of the elastic collision rate to the inelastic collision rate. For rubidium, the good-to-bad ratio is typically in the order of $10^2 - 10^3$ [86].

3.2.1 Short introduction to theory of evaporative cooling

The evaporation process and the increase in phase-space density are impeded by one-, two-body and higher order losses. The elastic collision rate γ_{el} for an untruncated Boltzmann velocity distribution given by [87]

$$\gamma_{el} = n_m \langle \sigma v_{rel} \rangle, \quad (3.5)$$

where the rate coefficient $\langle \sigma v_{rel} \rangle$ is the mean of the product between the elastic scattering cross section σ and the relative velocity v_{rel} of the colliding pair of atoms. Here we assumed that the elastic collision rate does not depend on the magnetic field of the trap. The mean density n_m is defined as

$$n_m(t) \equiv \frac{\int d^3r n^2(\vec{r}, t)}{\int d^3r n(\vec{r}, t)} = \frac{\int d^3r n^2(\vec{r}, t)}{N(t)}. \quad (3.6)$$

For neon, we start with the evaporative cooling in a regime where the elastic scattering cross section σ is energy dependent. With the approximation

$$\sigma = \frac{8\pi a^2}{k^2 a^2 + 1}, \quad (3.7)$$

where $k = mv_{rel}/2\hbar$ is the thermal wave vector and a the scattering length, one can use approximations leading to [87]

$$\langle \sigma v_{rel} \rangle = 8\pi a^2 \langle v_{rel} \rangle [\xi_c - \xi_c^2 e^{\xi_c} \Gamma(0, \xi_c)], \quad (3.8)$$

with $\xi_c = \hbar^2/(a^2 m k_B T)$, $\langle v_{rel} \rangle = 4\sqrt{k_B T/\pi m}$ the average relative velocity and

$$\Gamma(a, z) = \int_z^\infty dt t^{a-1} e^{-t}. \quad (3.9)$$

The good-to-bad ratio R , defined as the ratio of the elastic collision rate to the inelastic collision rate, is given by

$$R = \frac{\gamma_{el}}{\gamma_{inel}} = \frac{n_m \langle \sigma v_{rel} \rangle}{\alpha + \beta n_m}. \quad (3.10)$$

where the inelastic collision rate γ_{inel} is given by the one-body losses α and the two-body loss rate βn_m . Three-body and higher order losses have so far not been observed in metastable neon and are neglected for the moment. R depends both on density and temperature. For densities of $> 10^{11} \text{ cm}^{-3}$, the contribution of the one-body losses ($\alpha \approx 0.1 \text{ s}^{-1}$) to the inelastic collision rate is less than 10% and can be neglected. The elastic and the inelastic collision rate as function of the temperature and the corresponding good-to-bad ratio for ^{22}Ne are given in Fig. 3.2.

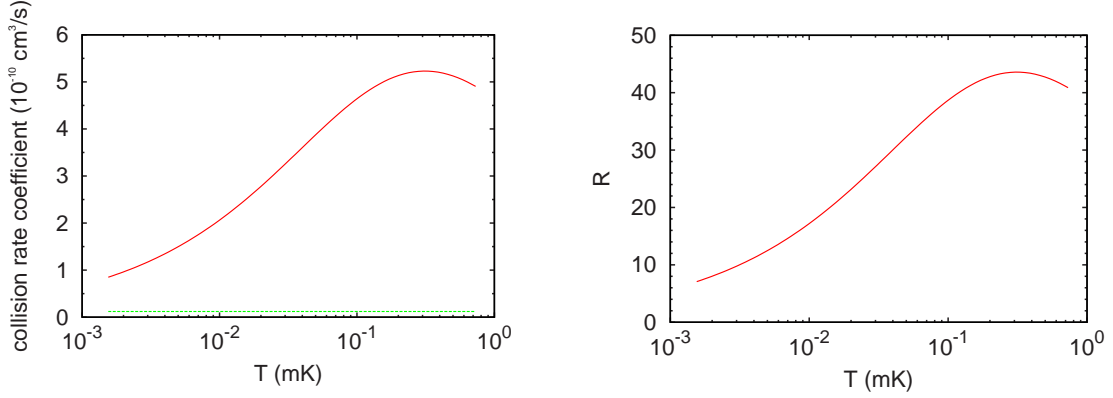


Figure 3.2: *Left-hand side: Elastic (solid) and inelastic (points) collision rate coefficient as function of temperature for ^{22}Ne with $a = +150a_0$ and $\beta = 1.2 \cdot 10^{-11} \text{ cm}^3/\text{s}$. For densities of 10^{11} cm^{-3} , the one-body loss contribute less than 10% and is not included. Right-hand side: Corresponding good-to-bad ratio as function of temperature.*

The aim of evaporative cooling is to keep the evaporation rate high by lowering the trap depth continuously. The case when the elastic collision rate increases during evaporative cooling is called runaway evaporation. For practically all atoms, the elastic collision rate coefficient decreases for lower temperatures. Although the elastic cross section increases for lower temperatures, it is counteracted and overwon by the decrease ($\sim \sqrt{T}$) in the averaged relative velocity. For neon, the elastic collision rate coefficient decreases for temperatures below ~ 0.1 mK and the evaporation becomes inefficient because of $R \rightarrow 0$.

3.2.2 Experimental realization

In comparison to some of the other atomic species, which already have been Bose condensed, ^{22}Ne has a large rate coefficient of elastic collisions but at the same time a rate coefficient of inelastic collisions which is several orders of magnitude larger than for other BEC species. The latter hampers evaporative cooling. How far can one get experimentally with evaporative cooling? Is it still possible to condensate neon? In order to evaporatively cool the atoms, the atom ensemble is prepared as described in Section 2.4. After a 400 ms Doppler cooling phase, the atoms are cooled down to a mean temperature of 0.48 mK at an offset field $B_0 = 26 \text{ G}$ ($\nu_{RF} = 54 \text{ MHz}$) and we start with $\sim 8.7 \cdot 10^7$ atoms at $\rho_\Phi = 2.2 \cdot 10^{-7}$ (see Fig. 3.3). To vary the trap depth, a rf field is applied to induce position dependent spin-flip transitions ($\Delta m = 1$). In the ideal case, all atoms with an energy above the truncation energy ϵ_t (Eq. 2.15) are effectively removed from the trap by adiabatic transitions to an untrapped magnetic substate. By sweeping the frequency from a high to a low value, the trap depth is gradually reduced. Experimental optimization of the evaporative ramps was performed by splitting the ramps into three parts of which each was optimized separately. Each ramp consist of reduction of the trap depth by a factor 5. We optimized the duration of the ramp for the highest attainable ρ_Φ . First we optimized evaporation ramps with a large B_0 of 26 G. After the third ramp, we end up with $2.1 \cdot 10^5$ atoms at $\rho_\Phi = 1.3 \cdot 10^{-5}$ and a mean temperature of 26 μK . The truncation parameter $\eta = \epsilon_{trunc}/k_B T$ is 2.2. For a lower end frequency, we obtained a phase-space density of

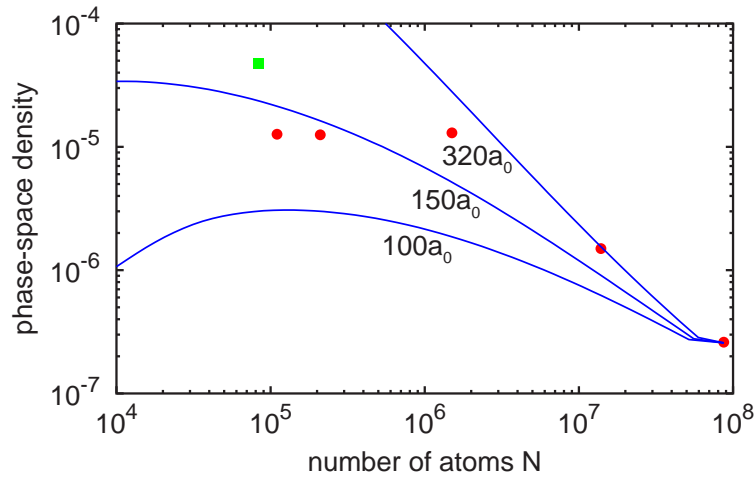


Figure 3.3: The dots indicate the results of evaporative cooling at $B_0 = 26$ G. The rectangle is the result of evaporative cooling after compression to $B_0 = 2.2$ G. Simulations of evaporative cooling for different scattering lengths are given by the lines and are discussed in Section 3.2.3.

$1.3 \cdot 10^{-5}$ at $N = 1.1 \cdot 10^5$ atoms. Since the good-to-bad ratio decreases for temperatures ~ 0.1 mK, it is favourable to adiabatically compress the trap after cooling to this temperature range. Thereby the temperature is increased and evaporation can continue with improved efficiency. The trap is compressed after the second evaporation ramp by lowering B_0 to 2.2 G. Followed by a third evaporation ramp, we end up with $8.4 \cdot 10^4$ atoms at a mean temperature of 21 μ K and with truncation parameter $\eta = 3.1$. The corresponding phase-space density ρ_Φ is $4.7 \cdot 10^{-5}$. Thus we have achieved a 200-fold increase in phase-space density by evaporation. For these evaporation ramps, the output of the signal generator, connected with a 10 W amplifier, was put at -5 dBm resulting in ~ 10 W rf-output for evaporative cooling. The lowest temperature so far observed is 14 μ K and a corresponding time-of-flight signal measured is given in Fig. 3.4.

3.2.3 Simulation of the evaporative cooling

Though ^{22}Ne has a large positive scattering length, it has as well a very large two-body loss coefficient. This two-body loss limits us to reach the degeneracy regime. So far we have reached $\rho_\Phi = 4.7 \cdot 10^{-5}$ with $N = 8.4 \cdot 10^4$ atoms. In order to verify whether a BEC is attainable, the evaporation cooling process is simulated. The program to simulate the evaporation cooling was developed in the group of Prof. Wolfgang Ertmer in Hannover by Claus Fühner and Kai Bongs [88, 86] to optimize the realization of a BEC with Rubidium atoms. It searches for optimum evaporation ramps for given starting parameters. The temporary evolution of the truncation energy ϵ_t is hereby chosen such that the efficiency parameter $\chi = (\dot{\rho}_\Phi/\rho_\Phi)/(\dot{N}/N)$ is maximum for each time step [89]. The program is

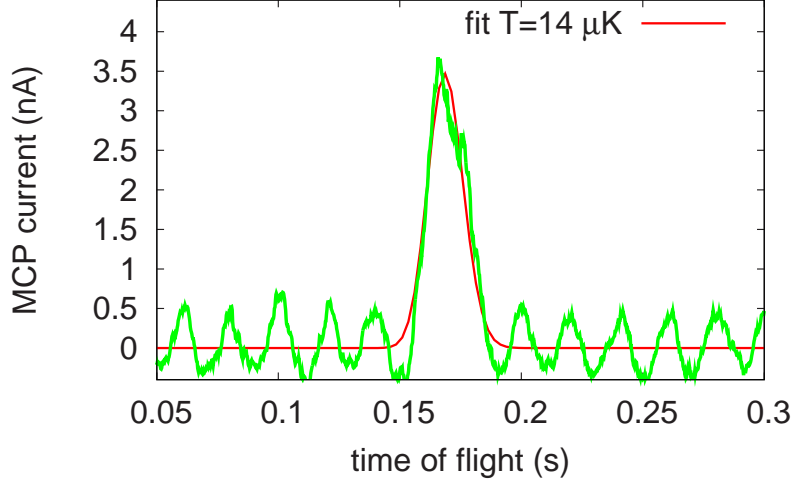


Figure 3.4: *The lowest temperature for neon so far observed after evaporative cooling.*

based on the kinetic theory of the evaporative cooling of a trapped gas developed by Luiten *et al.* [82]. The theory assumes collisions occurring in the s -wave regime only, an energy-independent elastic scattering cross section σ and sufficient ergodicity in the trap. In order to describe the distribution in a trap of finite depth, a truncated Boltzmann distribution is introduced and shown it is consistent with the Boltzmann equation. In the theory, the function describing the phase-space distribution is given by

$$f(\epsilon) = n_0 \Lambda^3 \exp[-\epsilon/k_B T] \Theta(\epsilon_t - \epsilon), \quad (3.11)$$

with ϵ the energy of the trapped atom, ϵ_t the truncation energy and $\Theta(\epsilon_t - \epsilon)$ a step function which is unity for atoms with an energy $\epsilon \leq \epsilon_t$ and zero otherwise. From this truncated distribution function given by Eq. 3.11 and the Boltzmann equation, equations describing the kinetics, particle loss and energy loss are obtained. Tol *et al.* [87] extended this theory to incorporate an energy-dependent elastic scattering cross section given by

$$\sigma = \frac{8\pi a^2}{k^2 a^2 + 1}. \quad (3.12)$$

This energy-dependent elastic scattering cross section was incorporated in the program in Hannover by Norbert Herschbach using the approximations from Tol *et al.* [87]. It allows us to simulate the evaporative cooling starting in the transition range between the low temperature limit and the unitarity limit. Incorporated in the program are as well one-body, two-body and three-body losses and spilling. For neon, three-body losses have so far not been observed since the two-body loss dominates. The three-body loss parameter L , describing the loss process $\dot{N}(t) = -L \int d^3r n^3(\vec{r}, t)$, can be calculated with [90]

$$L = 11.6 \frac{\hbar a^4}{m}, \quad (3.13)$$

leading to $L = 1.3 \cdot 10^{-28} \text{ cm}^6/\text{s}$ for ^{22}Ne with $a = 150a_0 (= 7.9 \text{ nm})$. To check the optimum route for evaporative cooling, we simulate the evaporation process for our experimental parameters. They show consistency with the experimental optimized evaporation route. In Fig. 3.3 optimum routes for evaporative cooling are given for $a = 100, 150$ and $320a_0$. The values correspond to the uncertainty in the scattering length. For $a = 150a_0$ we find a maximum ρ_Φ of $3.4 \cdot 10^{-5}$. With the current collisional properties of neon and initial density it is not possible to reach quantum degeneracy. However, it is possible to manipulate collisional properties using external fields like in metastable alkaline-earth atoms. Derevianko *et al.* [71] were the first to theoretically approach the problem of anisotropic long-range interactions between metastable alkaline-earth atoms in an external magnetic field. The theoretical study was carried further by Kokoouline *et al.* [72] for the alkaline-earth atom ^{88}Sr . It is unknown whether the manipulation of the collisional properties by external fields works for neon. In order to estimate the change in collisional properties needed to reach the degeneracy regime, we simulate the evaporative cooling for different scattering lengths and two-body loss coefficients. Starting with $2.0 \cdot 10^8$ atoms at a temperature of 0.72 mK and an offset field of 0.2 G ($B' = 215 \text{ G/cm}$, $B'' = 310 \text{ G/cm}^2$), we reach a phase-space density of $2 \cdot 10^{-3}$ with $N = 100$ atoms. Keeping the scattering length at $150a_0$ but suppressing the two-body loss coefficient by a factor of 7 suffices to reach the quantum degeneracy regime. The results of the simulation for $\beta = 0.17 \cdot 10^{-11} \text{ cm}^3/\text{s}$ and $\beta = 1.2 \cdot 10^{-11} \text{ cm}^3/\text{s}$ are given in Fig. 3.5.

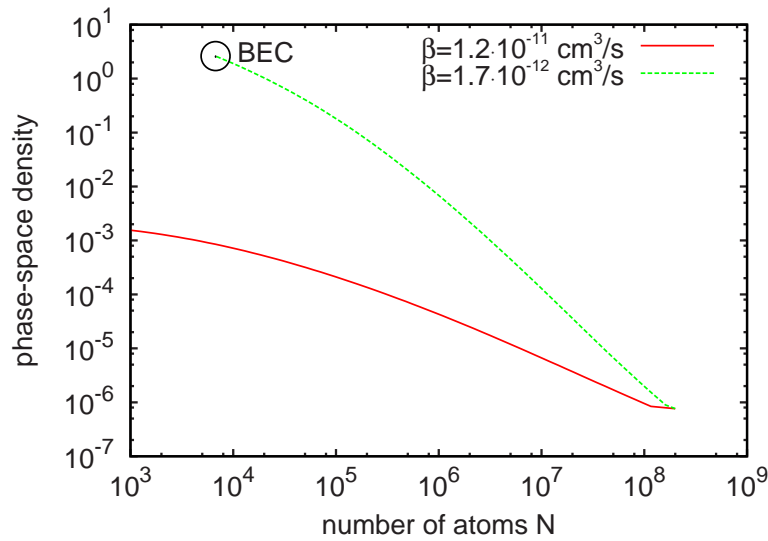


Figure 3.5: *Simulation: A 7-fold suppression in the two-body loss coefficient β leads to a BEC of metastable neon atoms after 1.7 s evaporation with $\sim 7 \cdot 10^3$ atoms at a density of $1.7 \cdot 10^{13} \text{ cm}^{-3}$ and a temperature of $0.5 \mu\text{K}$.*

Increasing the scattering length leads to a larger elastic scattering rate with the maximum moving to lower temperatures. The elastic scattering rate as function of the temperature for different scattering lengths in the range between $150a_0$ and $1500a_0$ is given in Fig. 3.6. Starting with the same initial parameters ($N = 2.0 \cdot 10^8$, $T = 0.72 \text{ mK}$ and $B_0 = 0.2 \text{ G}$),

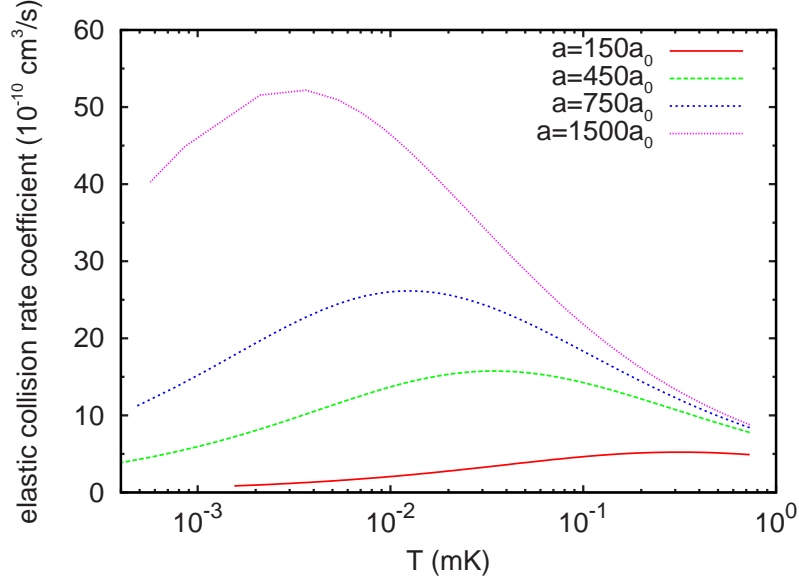


Figure 3.6: *The elastic scattering rate in the range between $150a_0$ and $1500a_0$ as function of the temperature. Increasing the scattering length leads to a larger elastic scattering rate with the maximum moving to lower temperatures.*

evaporative cooling is simulated for different scattering lengths. A 3-fold increase in the scattering length suffices to reach the quantum degeneracy regime but with only 500 atoms at $T = 0.2 \mu\text{K}$. Increasing the scattering length by a factor of 5 leads on the other hand to a BEC of metastable neon atoms with $\sim 6.5 \cdot 10^3$ atoms at $T = 0.5 \mu\text{K}$. In Fig. 3.7 we have given the results of this simulation for different scattering lengths.

We simulated the evaporative cooling also for higher initial number of atoms and although this leads to higher phase-space densities in the end, even a 50-fold increase in the initial number of atoms is not sufficient to reach the quantum degeneracy regime.

3.2.4 Conclusion

A 200-fold increase of phase-space density has been achieved by evaporative cooling. Simulations show that without changing the scattering length a and/or the two-body loss coefficient β the ρ_Φ is limited to $3.4 \cdot 10^{-5}$. Higher initial number of atoms lead also to higher phase-space densities. However, even a 50-fold increase in the initial number of atoms is not sufficient to reach BEC. On the other hand, a 7-fold suppression of the two-body loss coefficient or a 5-fold increase of the scattering length already suffices to reach the quantum degeneracy regime.

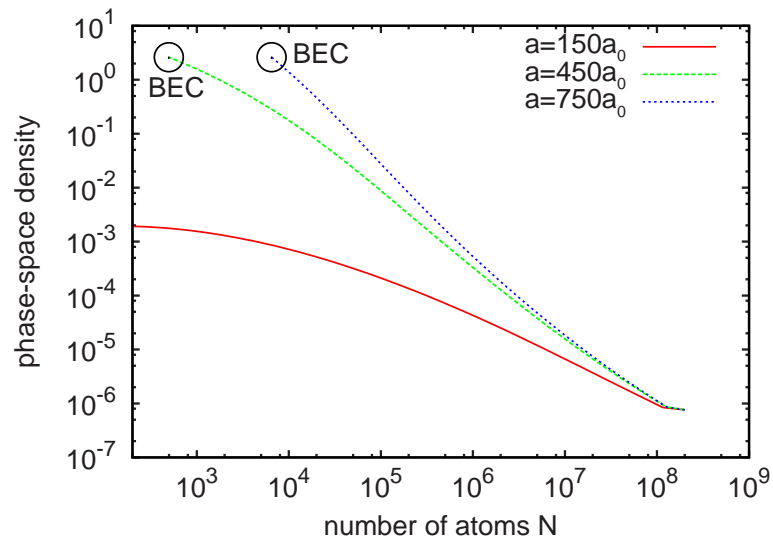


Figure 3.7: *Simulation: A 5-fold increase in the scattering length suffices to create a BEC of metastable neon after 0.5 s evaporation with $\sim 6.5 \cdot 10^3$ atoms at a density of $1.6 \cdot 10^{13} \text{ cm}^{-3}$ and a temperature of $0.5 \mu\text{K}$.*

Chapter 4

Light-assisted collision experiments

A laser tuned close to an atomic resonance excites a colliding neutral atom pair at the Condon radius R_C to an attractive C_3R^{-3} potential. The Condon radius R_C , defined as the distance between the atoms at which the colliding atom pair is excited, is given by $(C_3/\hbar\Delta_C)^{1/3}$ with Δ_C the detuning from atomic resonance [91]. Once the atom pair is promoted to the excited potential curve, these pairs accelerate towards each other, gaining kinetic energy as the internuclear distance is reduced ([92], Fig. 4.1). Collisions taking place before an atom pair radiatively decays to the lower state potential curve lead to additional excited-state inelastic processes such as excited-state Penning ionization. In some cases, fine-structure (or hyperfine-structure) changing collisions occur in which the excited atom pair exits the collision on a lower lying excited potential curve associated with an asymptote to a lower lying fine-structure (or hyperfine-structure) state. Apart from a change in the atomic state this results in a large release of kinetic energy in the collision ([93, 94, 95, 96], Fig. 4.1). If the atom pair radiatively decays before a collision takes place, then the collisional flux in the groundstate potential is enhanced. This leads to an enhancement of inelastic collision events and consequently trap loss. In our case this is predominantly ground-state Penning ionization. When the atom pair does not collide inelastically but instead gains enough kinetic energy before the radiative decay to escape the trap, this leads to so-called radiative escape loss. If the kinetic energy does not suffice for the atoms to leave the trap, this results in heating of the ensemble.

When the laser is tuned to a photoassociative resonance then the colliding atom pair can be photoassociated to a bound excited state and forms a dimer molecule. With this technique it is possible to probe the long range part of the molecular potentials. For alkali-atoms this resulted in the precise determination of s -wave scattering lengths, which is of high interest for studies of Bose-Einstein condensation in dilute trapped gases [97, 98, 99]. In these experiments, a tunable probe laser beam is sent through a cold gas of trapped atoms and the trap loss as function of the laser frequency is measured. When the probe laser is tuned to a photoassociative resonance, the trap losses increase by the formation of molecules which are not trapped. In some cases, the excited molecules are photoionized by absorbing a second photon. These ions can then be detected with high efficiency [100, 101]. Metastable rare gas systems differ from alkali systems mainly with regards to the possibility of Penning ionization occurring at short distances. A dimer molecule formed

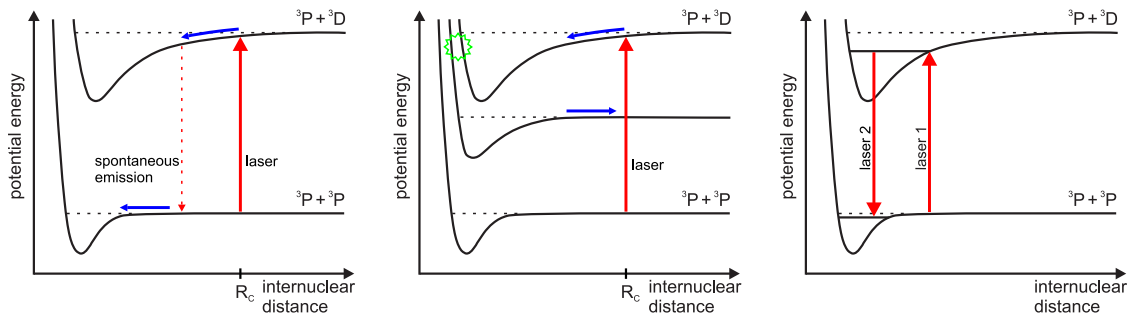


Figure 4.1: Schematic view of light-assisted collision processes: Collisional flux enhancement in the ground-state, radiative escape (left), light-assisted fine-structure changing collision (middle) and a two-colour photoassociation technique to probe vibrational states in the ground state potential (right).

by photoassociation has an internal energy of several tenths of electronvolt and is expected to be short-lived compared with the vibrational period by the large ionization probability at short distances. In some cases, the potential curves have a shallow well below the asymptote at long distances. A dimer molecule formed by photoassociation in such a well is on the other side expected to be long-lived since the atoms in these states do not come close enough to each other for the Penning ionization reaction to be probable. In 2000, three vibrational series were observed by photoassociation spectroscopy in metastable helium over a frequency range of 20 GHz. The photoassociative resonances manifested themselves as peaks in the Penning ionization rate [62]. Then in 2003 long-range dimer states in a purely long-range well were measured by trap heating [102]. And in 2006, a two-colour photoassociation technique was applied to probe the vibrational states in the ground-state potential of metastable helium ([103], Fig. 4.1). This resulted in a precise determination of the scattering length for the 2^3S_1 metastable state in helium.

For metastable neon, Doery *et al.* [68] calculated the long-range diatomic $s + p$ potentials. Of special interest are the potential curves connecting asymptotically with the $^3P_2 + ^3D_3$ separated atomic states, since these atomic states form the cycling transition that we use for cooling and trapping. The potential curves connecting asymptotically with the $^3P_2 + ^3D_2$ are more interesting since there exist long-range potential outer wells which could support long-lived photoassociation states for which Penning ionization reactions are less probable. With 40 potential curves (Fig. 4.2), this could result in a complicated spectrum with rotational and vibrational spectra in photoassociation experiments. However for many of these potential curves it will be difficult or even impossible to observe photoassociation resonances, since ionization reactions in light-assisted collisions can be expected to be dominant.

4.1 Experimental procedure

We probed the long range part of the molecular potentials below the $^3P_2 \rightarrow ^3D_3$ transition at 640.4 nm and also the $^3P_2 \rightarrow ^3D_2$ transition at 633.6 nm. For these measurements, the

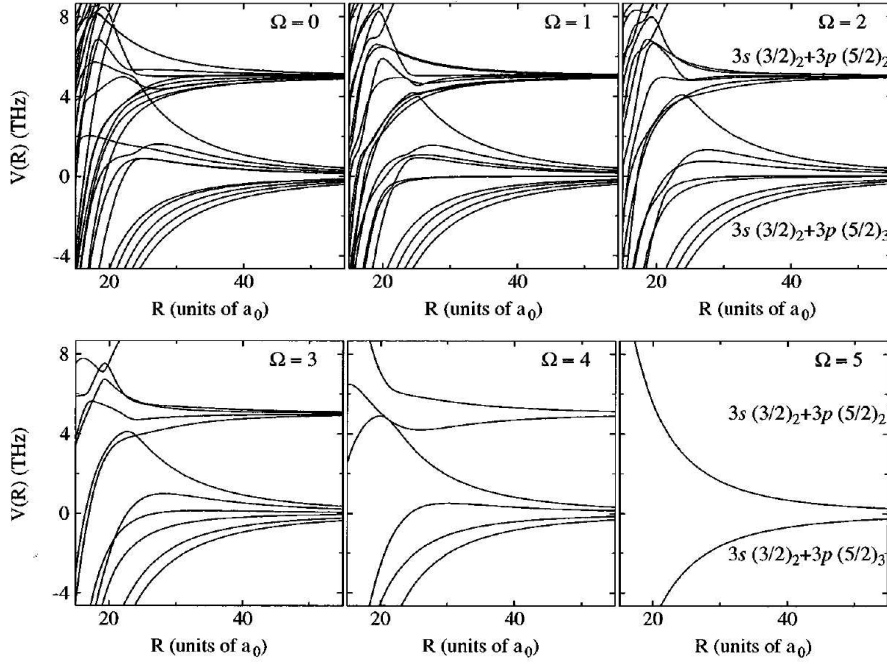


Figure 4.2: Diatomic Ne potentials connecting asymptotically to $3s(3/2)_2 + 3p(5/2)_3$ (${}^3P_2 + {}^3D_3$) and $3s(3/2)_2 + 3p(5/2)_2$ (${}^3P_2 + {}^3D_2$) limits. The asymptotic energies are 1.2926 a.u. and 1.2933 a.u.). The $3s(3/2)_2 + 3p(5/2)_3$ asymptotic limit has been chosen as the zero of energy [104].

second dye laser was used as probe laser. Locked to its external reference cavity, this laser has a linewidth of 4 MHz and can be tuned without mode hop over a range of 20 GHz. In order to keep track of the frequency, we record the signal from absorption saturation spectroscopy in a heated I_2 vapor cell as well as the saturation spectroscopy signal of neon (see Section 2.2.2) and the fringes of a Fabry-Pérot interferometer locked on the trap laser and thus used as transfer cavity. The FSR of this resonator is determined from the isotope shift ${}^{22}\text{Ne} - {}^{20}\text{Ne}$ and is 151.0(3) MHz. The experimental procedure consisted of slowly scanning the frequency of the probe laser while the trap setup repeated the following cycle: the MOT was loaded for 0.5 s with ${}^{20}\text{Ne}$ metastable atoms and compressed during 50 ms to reach a high density of $3 \cdot 10^{10} \text{ cm}^{-3}$. Then for 40 μs the MOT light was switched off and the probe laser was switched on. Finally the MOT light was switched on again to determine the fraction of atoms remaining after the probe pulse. Apart from measuring the MOT fluorescence we recorded the signal from the MCP detector with the grid in front of it at negative potential to attract ions. From the signal levels at the different times during the experimental cycle we inferred the atom loss induced by the probe laser as well as the ion production rate during the probe laser pulse. Additionally, the time-of-flight delay of 20 μs for ions allows the discrimination between ions and MCP signal from UV photons produced when the probe laser induces transitions to states of short radiative lifetimes. In the compressed MOT number densities of $3 \cdot 10^{10} \text{ cm}^{-3}$ were achieved and probe laser intensities of 0.3 kW/cm^2 were used.

4.2 Experiment at the ${}^3\text{P}_2 \rightarrow {}^3\text{D}_3$ transition

For the experiments at ${}^3\text{D}_3$ line, the probe laser was scanned to -10 GHz from the atomic resonance ${}^3\text{P}_2 \rightarrow {}^3\text{D}_3$ with a step size of 26 MHz. Also scans with smaller frequency steps of 5.0 MHz/step around the atomic resonance were carried out. The corresponding ionization signal during the probe laser pulse and after the probe laser pulse, normalized to the ionization signal from the MOT before the probe laser pulse are given in Fig. 4.3 and 4.4. Given as well is the I_2 spectroscopy signal.

We observe that for large detuning the ionization signal after the probe laser pulse, normalized to the ionization signal from the MOT, is 80% compared to ionization signal before the probe laser pulse. This can be ascribed to the trap loss in the compressed MOT. Since the ionization signals from the MOT before, during and after the probe laser pulses are averaged over a certain time-interval, these ionization signals differ.

The ionization signal during the probe laser pulse shows a pronounced enhancement of Penning ionization for red detuning. It is a smooth and spectrally broad feature with a maximum close to atomic resonance for red detuning. No enhancement of the signal is seen for blue detuning. This dependence of the ion signal on probe laser detuning is characteristic for optical collisions.

Would the probe laser excite photoassociative resonances, peaks in the ionization signal during the probe laser pulse can be expected. Trap loss induced by formation of molecules would as well produce dips in the ionization signal after the probe laser pulse. Such narrow structures which would indicate photoassociative resonances cannot be found in the measured spectra. Also scans with smaller frequency steps of 5.0 MHz/step around the atomic resonance did not show any narrow structures (Fig. 4.4).

4.3 Experiment at the ${}^3\text{P}_2 \rightarrow {}^3\text{D}_2$ transition

For the experiments performed close to the ${}^3\text{D}_2$ line, we scanned the probe laser from -10 to -3 GHz with a step size of 7.0 MHz and from -3 to 0.6 GHz with a step size of 4.2 MHz. The ionization signals together with the I_2 spectroscopy signal are given in Fig. 4.5.

Very interestingly, for red detunings from the transition to the ${}^3\text{D}_2$ state we observe that the probe laser does not produce the strong enhancement of the ionization signal measured for the ${}^3\text{P}_2 \rightarrow {}^3\text{D}_3$ transition. Just a slight increase of the MCP signal close to atomic resonance is visible. Atom loss (middle curve in Fig. 4.5) is strong in a narrow region at atomic resonance. It appears symmetric for red and blue detuning. This is typical for a mechanism involving only single atoms. We can conclude that practically no laser induced enhancement of inelastic collision processes occurs.

The difference to the observation made for the ${}^3\text{P}_2 \rightarrow {}^3\text{D}_3$ transition is striking and very remarkable. Comparing the transition parameters main differences are: The radiative decay rate $\Gamma'/2\pi = 2.6$ MHz for the ${}^3\text{P}_2 \rightarrow {}^3\text{D}_2$ transition is approximately a factor of

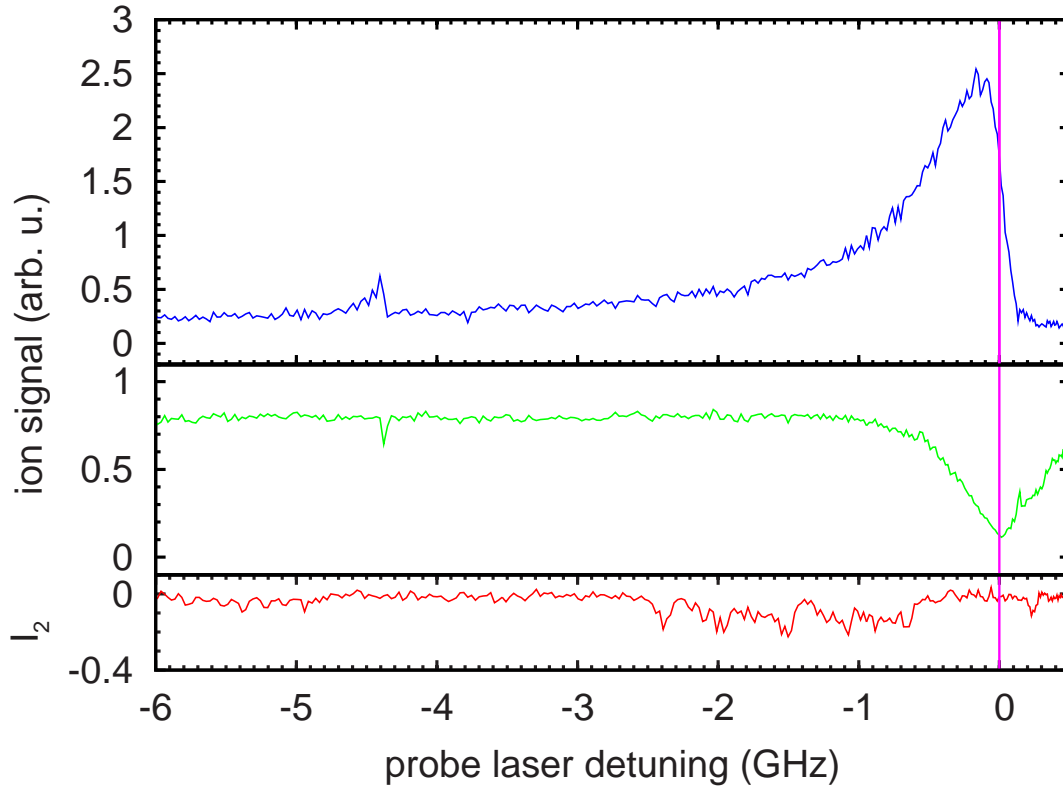


Figure 4.3: Ionization loss induced by the probe laser for detunings close to the ${}^3P_2 \rightarrow {}^3D_3$ transition. The ionization signal during the probe laser pulse (upper part) and after the probe laser pulse (middle part) are normalized to the ionization signal from the MOT before the probe laser pulse. Given as well is the I_2 spectroscopy signal (lower part). (The increase in ionization signal during the probe laser pulse at -4.35 GHz is ascribed to a second probe laser frequency component. In a beat note experiment the second frequency component was found to have a 10^3 -fold lower intensity as the main laser mode.)

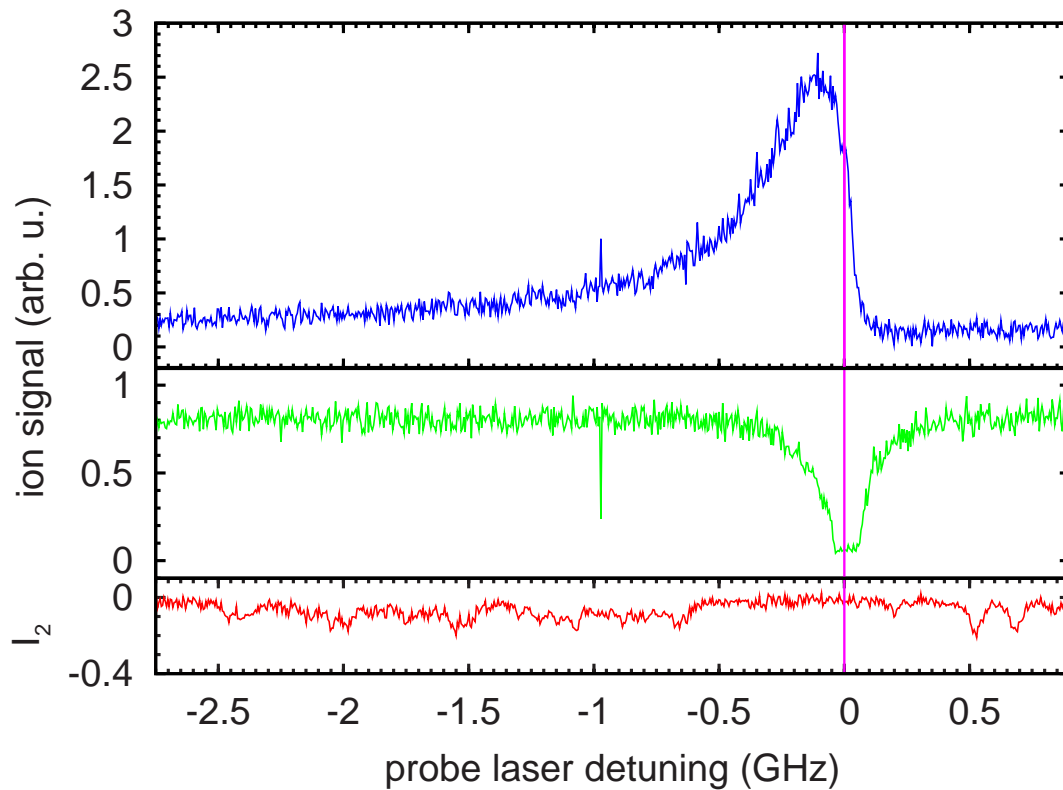


Figure 4.4: Ionization loss induced by the probe laser for detunings close to the ${}^3P_2 \rightarrow {}^3D_3$ transition measured in more detail around the atomic resonance: normalized ionization signal during the probe laser pulse (upper part), ion signal after probe laser pulse (middle part) and I_2 spectroscopy signal (lower part). (The narrow structure at -0.97 GHz is an artifact caused by a failure of the MOT.)

three smaller than Γ for the ${}^3\text{P}_2 \rightarrow {}^3\text{D}_3$ transition. In addition, the ${}^3\text{D}_2$ state decays as well with the probability of 74% via the ${}^1\text{P}_1$ states to the ground state emitting easily detectable UV photons [105]. Still the total lifetime decay rate of the ${}^3\text{D}_2$ state with $\Gamma_{tot}/2\pi = 7.8$ MHz is very close to the decay rate of the ${}^3\text{D}_3$ state ($\Gamma/2\pi = 8.18$ MHz).

Regarding the smaller radiative Γ' , one can conclude that the C_3 coefficient characterizing the excited state potential curves is about three times smaller because of the relation $C_3 \simeq \hbar\Gamma(\lambda/2\pi)^3$ [91]. This means that atom pairs excited to upper state potential curves will see a reduced acceleration in these potentials leading to a smaller effect of radiative enhancement of collisional flux. It is hard to imagine that radiative enhancement of collisions could become that small in this way especially because the excitation probability increases for smaller C_3 coefficients [91]. Simulation of the laser-induced collision process for our parameters is required to give a definite explanation.

Also here no obvious narrow structures can be found in the spectra which would indicate excitation of photoassociation resonances.

4.4 Conclusion

These are the first experiments performed in metastable neon in which the frequency dependence of laser-induced collisions and the possibility to excite photoassociation resonances are investigated. The frequency dependence of laser enhanced Penning ionization for the transition to the ${}^3\text{D}_3$ line is interesting in itself and the results of the measurement can be useful. The observed absence of the collisional enhancement effect by laser light for the transition to the ${}^3\text{D}_2$ line is intriguing and for an explanation calculations are required. An experimental signature for the excitation of photoassociation resonances was not found.

Although metastable neon differs in many aspects from metastable helium, photoassociation experiments should also be possible with neon. The system of adiabatic diatomic potential curves for neon is more complicated, because there are more atomic states and coupling possibilities involved. Also the fine structure splitting is on the order of THz rather than GHz. Doery *et al.* [68] pointed out states with expected ionization width small enough for an observation of photoassociation. These states are most probable found in so-called purely long range potential wells which form under the asymptotes of higher lying atomic finestructure states. Another promising candidate is the long-range potential well connecting to the $3s[3/2]_2 - 3p'[3/2]_2$ asymptote which can be populated from the ${}^3\text{P}_2$ metastable state with laser light at 594.6 nm. In future experiments larger number densities, better spectral resolution and higher stability of the magneto-optical trap will favour a more systematic and hopefully successful search for photoassociative resonances.

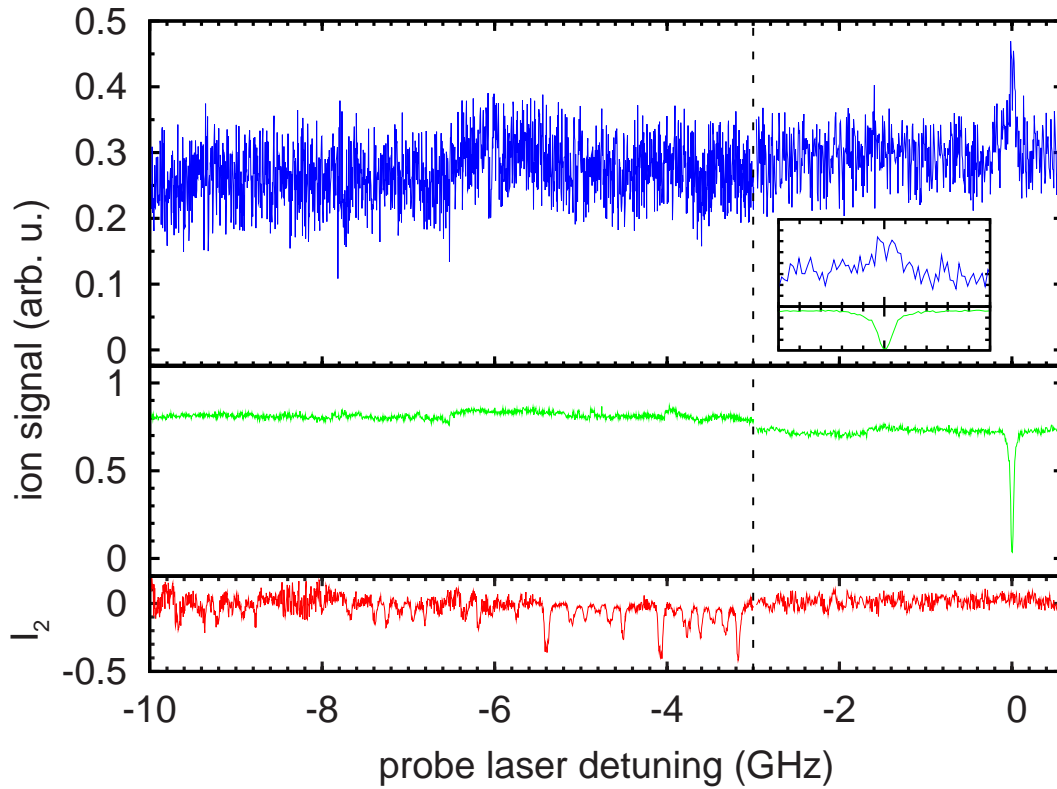


Figure 4.5: Ionization loss induced by the probe laser beam for detunings close to the ${}^3P_2 \rightarrow {}^3D_2$ transition. The ionization signal during the probe laser pulse (upper part) and after the probe laser pulse (middle part) are normalized to the ionization signal from the MOT before the probe laser pulse. Given as well is the I_2 spectroscopy signal (lower part). The measurement consists of two partial scans. The first scan with a step size of 7.0 MHz goes from -10 to -3 GHz and the second scan with a step size of 4.2 MHz covers the range from -3 to 0.6 GHz. The inset shows with more detail the ionization signal during the probe laser pulse and after the probe laser pulse for detunings between -0.25 and 0.25 GHz.

Chapter 5

Two-body loss coefficient as function of magnetic field

From simulations of evaporative cooling (Chapter 3) it is clear that a 5 to 7-fold increase of the good-to-bad ratio for ^{22}Ne suffices to reach quantum degeneracy. The collisional properties and thereby the good-to-bad ratio can be manipulated with external fields. This was essential to achieve BEC in other species like, for instance, Cs, where a Feshbach resonance was used to change the collisional properties. For atoms in $^3\text{P}_2$ states like metastable earth-alkaline atoms and also metastable neon atoms, it was shown by Derevianko and Porsev as well as later by Kokoouline *et al.* [71, 72], that there exists a dependence of elastic and inelastic collisional properties on magnetic field for moderate field strengths ~ 100 G due to the anisotropic interaction of these systems and its dependence on magnetic field through van der Waals-Zeeman interaction. Detailed calculations have been done for earth-alkaline atoms Mg, Ca, Sr. So far no such calculations exist for metastable neon. Still similar effects can be expected. To look for this effect within the range accessible in the magnetic trap, we performed measurements of the two-body loss coefficient as a function of magnetic field. With temperatures between 0.1 and 0.5 mK, the atoms see a thermal width of the magnetic field in the trap $\Delta B = k_B T / 3\mu_B < 2$ G. Thus one can assume that collisions happen essentially at the offset field of the magnetic trap B_0 .

5.1 Theoretical description of the trap loss

The trap loss ("number decay") is described by one-body, two-body and higher-order losses. For neon, these higher-order losses have so far not been observed since the two-body loss dominates. One-body losses are density independent losses, such as the limited lifetime of the metastable state and collisions with the background gas. Two-body losses are density dependent. These are the collisions in which a trapped atom, by collision with a second trapped atom, is lost. In a trap with metastable neon atoms, these losses are mostly Penning ionization reactions. The number of these collisions is proportional to the probability that two atoms are at the same location at the same time. The number decay

can thus be described by the following differential equation:

$$\dot{N}(t) = -\alpha N(t) - \beta \int d^3r n^2(\vec{r}, t) + \mathcal{O}(n^3), \quad (5.1)$$

with α the one-body loss rate, β the two-body loss coefficient, N the number of atoms and n the density. With the mean density n_m defined as

$$n_m(t) \equiv \frac{\int d^3r n^2(\vec{r}, t)}{\int d^3r n(\vec{r}, t)} = \frac{\int d^3r n^2(\vec{r}, t)}{N(t)} \equiv \frac{N(t)}{V_{eff}(t)}, \quad (5.2)$$

where V_{eff} is the effective volume, one can rewrite the differential equation to

$$\dot{N}(t) = -\alpha N(t) - \beta \frac{N^2(t)}{V_{eff}(t)}. \quad (5.3)$$

When the effective volume is not time dependent, the differential equation can be integrated, giving us the following relation:

$$N(t) = \frac{\alpha N(0)}{\left(\beta \frac{N(0)}{V_{eff}} + \alpha\right) e^{\alpha t} - \beta \frac{N(0)}{V_{eff}}}, \quad (5.4)$$

with $N(0)$ the number of atoms at $t = 0$. For a time dependent V_{eff} , for example when the cloud is heated, one can formally integrate the differential equation and arrive at the relation:

$$\begin{aligned} \left(\frac{1}{t} \log \frac{N(t)}{N(0)}\right) &= -\alpha - \beta \left(\frac{1}{t} \int_0^t dt' n_m(t')\right), \\ y(t) &= -\alpha - \beta x(t). \end{aligned} \quad (5.5)$$

This is linear relation between quantities $x(t)$, $y(t)$, which we numerically obtain from experimental data. Temperature and effective volume variations are now accounted for by calculating the mean density n_m for each data point. In addition, this representation of the data is convenient to extract β and α in least square fitting procedures [70].

Heating rate Two-body loss contribute also to the heating of the ensemble. Most of the losses occur in the center of the trap, since the density there is the highest. The average energy carried away by a lost atom is less than the mean energy per trapped atom. The assumption of a temperature dependent two-body loss coefficient given by $\beta_{heating} \propto v_{rel}^{2j}$ leads to an increase of average energy per atom, and thus to a temperature increase according to:

$$\dot{T}(t) = (1 - q)\beta_{heating}n_m(t)T(t). \quad (5.6)$$

where $q = (9 - 2j)/12$ accounts for the below-average potential energy $q \times (3 + 3)k_B T$ when two atoms escape after an inelastic collision, and for the difference between the average kinetic energy of each colliding particle and $(3/2)k_B T$ [106]. For low temperatures, the two-body loss rate is temperature independent ($j = 0$) and the equation simplifies to:

$$\dot{T}(t) = \frac{1}{4}\beta_{heating}n_m(t)T(t). \quad (5.7)$$

Integrating the differential equation, one obtains the following relation

$$\left(\log \frac{T(t)}{T(0)} - c \int_0^t dt' \frac{1}{T(t')} \right) = \frac{1}{4}\beta_{heating} \left(\int_0^t dt' n_m(t') \right), \quad (5.8)$$

where c is a constant heating rate. This is a linear relation, where the quantities between brackets are determined by the experimental data (see also Eq. 5.5).

5.2 Measurements

After the Doppler cooling phase (Section 2.4) we have $\sim 6 \cdot 10^7$ atoms (^{22}Ne) at a mean temperature of 0.4 mK with $B_0 = 26$ G. To measure the two-body loss coefficient as function of the magnetic field, the atomic ensemble is prepared at different B_0 . With the second MOSFET bank (MF2), we control the current through the Helmholtz coils. This allows us to compress or decompress the magnetic trap, and the number decay can be measured for different offset fields.

Doppler cooling is very sensitive to a change in the offset field and this field should be kept constant to have a reproducible ensemble preparation. MOSFETs have a strong non-linear behaviour. Temperature effects and also electronic noise at the control output of the MOSFET bank leads to a varying offset field and a non-reproducible ensemble preparation. We solved this problem by connecting a passive resistor in series with MF2. The resistance of the resistor is chosen such, that for a fully conducting MF2, we have an offset field of 26 G. The total current is controlled by changing the total resistance of the system with MF1. For longer times, however, the system heats up and the total resistance changes. To assure a constant total current, the power supply for the magnetic trap was operated in a current control mode at 231 A.

Other effects which can influence the number decay measurement are heating effects and laser intensity fluctuations. They are cancelled by measuring the number decay back and forth repeatedly. For number decay measurements at $B_0 < 26$ G, we first evaporative cooled the atomic ensemble, and then compressed the magnetic trap to a specific B_0 . For number decay measurements at $B_0 > 26$ G, we connected the passive resistor in parallel with MF2. This allowed us to change the offset fields between 26 and 47 G. After

Doppler cooling the cloud at $B_0 = 47$ G, the density is further increased by evaporative cooling. The magnetic trap is then compressed to a specific B_0 , and a number decay is measured. We started with $1 - 30 \cdot 10^6$ atoms at temperatures of $0.1 - 0.5$ mK and mean densities of $5 - 10 \cdot 10^9$ cm³/s. The background pressure during these measurements was $1 - 4 \cdot 10^{-10}$ mbar.

The number of atoms for different trapping times are determined from absorption images. From our number decay measurements we can extract the two-body loss coefficient β . Since two-body losses contribute to heating of the ensemble, we have a time dependent effective volume $V_{eff}(t)$. To extract the two-body loss coefficient β from number decay measurements, we need to know the mean density for each measured point. With the trap frequencies ω_{ax} and ω_{rad} obtained from the total and bypass current (Section 2.2.7), a single absorption measurement suffices to determine both the temperature and the radii of the atomic cloud (Eq. 2.22). For each point we numerically calculate the mean density, where the full trapping potential described by the trap parameters B_0 , B' and B'' is considered. To produce the quantity $x(t) \equiv t^{-1} \int_0^t dt' n_m(t')$ (Eq. 5.5) we do this integration of the mean density numerically. With $x(t)$ and $y(t)$, the number decay is described by a linear relation, where the slope is given by the two-body loss coefficient β , and the offset given by the one-body loss rate α . In Fig. 5.1, a number decay and a corresponding linear representation of the number decay are given for a measurement at $B_0 = 46.7$ G. From the slope we obtain the two-body loss coefficient: $\beta = 2.9(8) \cdot 10^{-11}$ cm³/s. The number

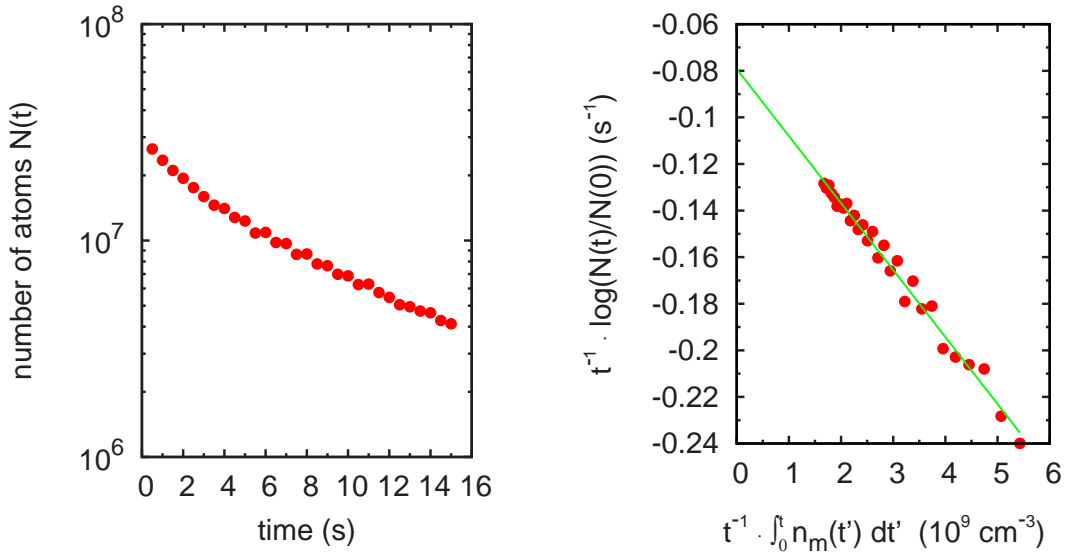


Figure 5.1: *Left-hand side: Number decay for spin-polarized ^{22}Ne in the 3P_2 metastable state at $B_0 = 46.7$ G. Right-hand side: Corresponding linear representation of the number decay measurement with $\beta = 2.9(8) \cdot 10^{-11}$ cm³/s.*

decay measurements are repeated for different offset fields. From each measurement the two-body loss coefficient is extracted using Eq. 5.5 in the analyses. The number decay for $B_0 = 2.2$ and 25.2 G is given in Fig. 5.2 and 5.3.

From the trap loss measurements we observe that the two-body loss coefficient is temperature independent in the range of 0.1 to 0.5 mK. This allows us to use Eq. 5.7 to

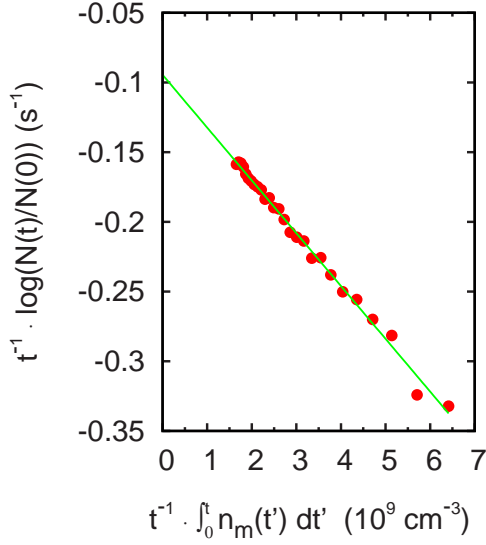


Figure 5.2: Linear representation of the number decay for spin-polarized ^{22}Ne in the 3P_2 metastable state at $B_0 = 2.2$ G with $\beta = 3.8(10) \cdot 10^{-11} \text{ cm}^3/\text{s}$.

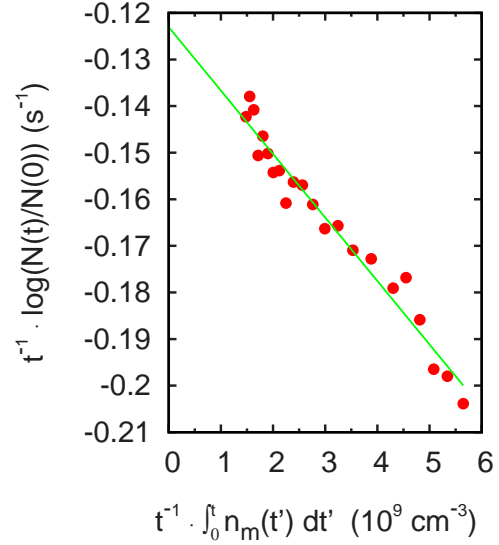


Figure 5.3: Linear representation of the number decay for spin-polarized ^{22}Ne in the 3P_2 metastable state at $B_0 = 25.2$ G with $\beta = 1.4(4) \cdot 10^{-11} \text{ cm}^3/\text{s}$.

get a second independent measurement of the rate of inelastic collisions from observed heating rate (see Section 5.1). Using the transformation of data described by Eq. 5.8, the heating of the ensemble is described by a linear relation, where the slope is given by the two-body loss coefficient β_{heating} . In Fig. 5.4, the temperature increase during a number decay and a corresponding linear representation of the heating rate are given for a measurement at $B_0 = 46.7$ G. From the slope we obtain the two-body loss coefficient: $\beta_{\text{heating}} = 2.2(6) \cdot 10^{-11} \text{ cm}^3/\text{s}$. This value agrees with the result from the corresponding trap loss measurement and indicates that other heating mechanisms do not contribute significantly to observed heating rates.

To check the purity of the spin state of the trapped atoms, we performed a Stern-Gerlach experiment in which the inhomogeneous field separates the atoms with different magnetic substates. The field is obtained by running a current only through one of the dipole coils (DPS). One should be careful though, that the spin state is sustained while the configuration of the coils is changed. After switching off the inhomogeneous field, the atoms are detected with absorption imaging. From this experiment we see that the purity of the spin state is more than 90%.

The extracted two-body loss coefficients from number decay measurements at different offset fields are given in Fig. 5.5. We observe that β increases towards both small and large offset fields of the magnetic trap ($2 \leq B_0 \leq 50$ G).

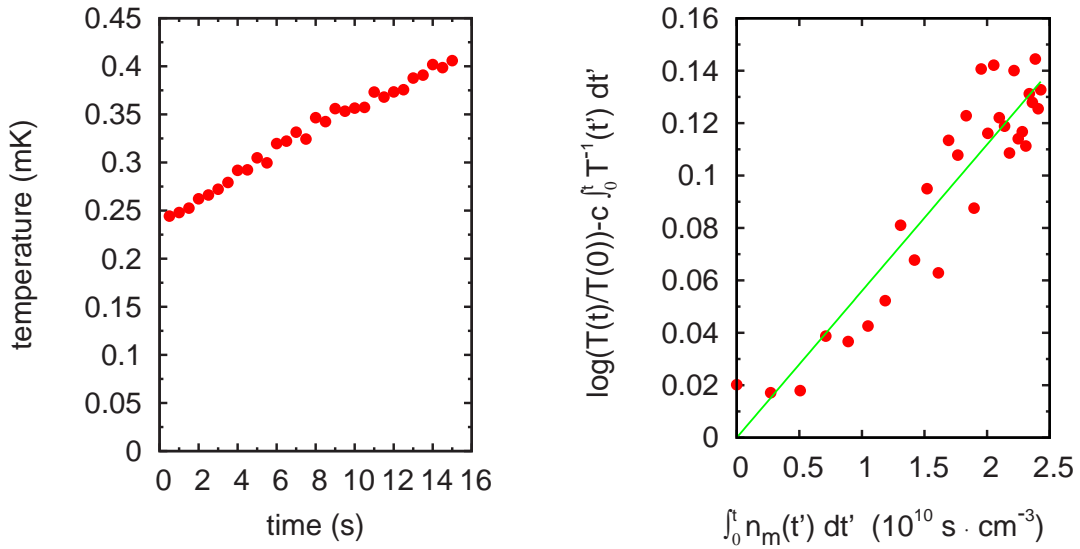


Figure 5.4: Left-hand side: Temperature increase during the number decay for spin-polarized ^{22}Ne in the 3P_2 metastable state at $B_0 = 46.7$ G. Right-hand side: Corresponding linear representation of the heating with $\beta_{\text{heating}} = 2.2(6) \cdot 10^{-11} \text{ cm}^3/\text{s}$ and $c = 8.8 \text{ } \mu\text{K}/\text{s}$.

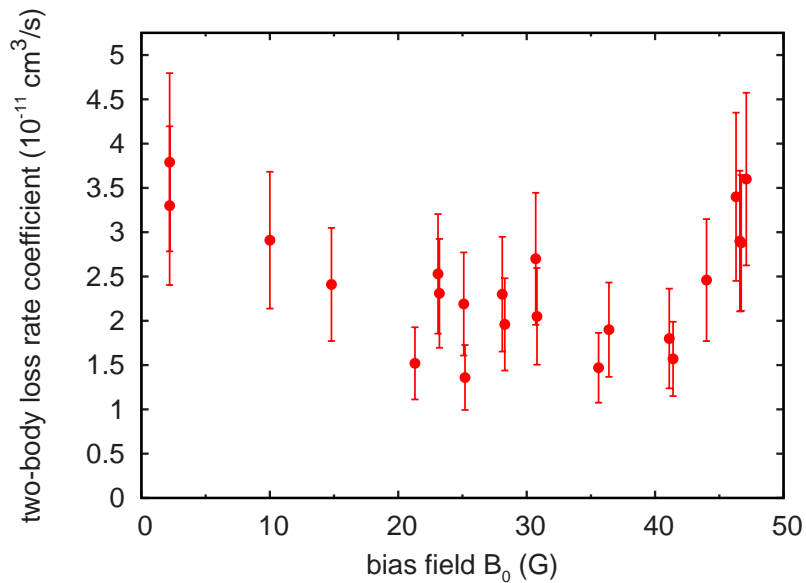


Figure 5.5: Two-body loss parameter as function of the offset field for spin-polarized ^{22}Ne in the 3P_2 metastable state.

5.3 Conclusion

From the measurements, we observed that the two-body loss coefficient is temperature independent in the range of 0.1 to 0.5 mK. We measured the two-body loss coefficient for different offset fields between 2 and 47 G (Fig. 5.5). The two-body loss coefficient has a magnetic field dependence and increases towards both small and large offset fields. With the magnetic trap, we are limited to offset fields ≤ 50 G. In this range of fields, the two-body loss is too large to achieve a BEC of magnetically trapped metastable neon.

Trapping metastable neon in an optical dipole trap extends the range of possible experiments. We can measure the two-body loss coefficient as function of the magnetic field for fields up to 400 G using the Helmholtz coils. Furthermore, we can trap neon atoms in their lowest magnetic substate $^3P_2(m = -2)$ and measure two-body loss. We can also trap the 3P_0 metastable state. Since this state has no magnetic moment, it can only be trapped in an optical dipole trap and so far nothing is known about the elastic and inelastic collisions of this state.

Chapter 6 explains the trapping of metastable neon atoms in an optical dipole trap. We are the first to have trapped the 3P_0 metastable state. It could be an interesting candidate for a BEC in neon provided that the collisional parameters are favourable for efficient evaporative cooling.

Chapter 6

Trapping neon in the 3P_0 metastable state

From measurements of two-body loss as function of magnetic field (Chapter 5), it turned out that the two-body loss rate increases towards both small and large offset fields of the magnetic trap ($2 \leq B_0 \leq 50$ G). With the implementation of an optical dipole trap, the range of magnetic fields can be extended up to 400 G. Another advantage is that the atoms can be trapped in their lowest magnetic substate. In ^{52}Cr the two-body loss rate could be drastically reduced in this way, which was essential to produce a Bose-Einstein condensate [107]. For ^{133}Cs , this also led to a full suppression of the two-body loss processes, but the approach to BEC was limited by three-body loss. By tuning interactions with external magnetic fields using a low-field Feshbach resonance, BEC has been achieved in Cs as well [108]. For neon, three-body losses have so far not been observed since the two-body loss dominates in the $m = +2$ state. It is an open question whether trapping in the $m = -2$ state will reduce the two-body loss substantially. Therefore, it would be very intriguing to trap the neon atom in the anti-trapping state and determine the two-body loss as function of the magnetic field.

We decided to trap the other metastable state 3P_0 first, because this state can only be trapped in an optical dipole trap. Atoms have never been trapped in this state, thus nothing is known about the elastic and inelastic collisions. It has a much longer lifetime of ~ 430 s [109] compared to the lifetime of $14.73(14)$ s of the 3P_2 metastable state [110]. This metastable state could also be an interesting candidate for Bose-Einstein condensation in neon, provided that the collisional parameters are favourable for efficient evaporative cooling. In the following section, both the ac Stark shift and the calculation of the mean density are discussed. Then, the experimental realization of the optical dipole trap is presented in Section 6.2. This chapter concludes by describing the experiment in which we trapped neon atoms in the 3P_0 metastable state. As far as we know, we are the first to have trapped neon atoms in this state.

6.1 The optical dipole trap

A laser field leads to an energy shift of atomic levels. This energy shift, the so-called dynamic Stark shift or ac Stark shift, is used to realize a trapping potential. In this section the description of the ac Stark shift and the calculation of the polarizability for the 3P_2 and the 3P_0 metastable states of neon are given. Then, the realization of a dipole potential using a spatially inhomogeneous light field is treated. A calculation of the density distribution in an optical dipole trap rounds up this chapter.

6.1.1 ac Stark shift

Starting from a classical point of view, where the atom is considered to be a simple oscillator subject to a classical radiation field, we derive the equations for the dipole potential and the scattering rate, and extend these to the case of multi-level atoms.

The atom as a classical oscillator

If the atom is considered to be a simple oscillator subject to a classical radiation field, equations for the dipole potential and the scattering rate can be deduced [111]. An atom placed in such a field, for example in a laser light, will have an induced atomic dipole moment \vec{p} oscillating at the driving frequency ω of this electric field. The electric field, described as $\vec{E}(\vec{r}, t) = \hat{e}E_0(\vec{r}) \exp[-i\omega t] + c.c.$ with \hat{e} the unit polarization vector, is related to the induced dipole moment $\vec{p}(\vec{r}, t) = \hat{e}p_0(\vec{r}) \exp[-i\omega t] + c.c.$ by the following relation:

$$p_0(\vec{r}) = \alpha E_0(\vec{r}), \quad (6.1)$$

where α is the complex polarizability, which depends on the driving frequency ω . The interaction potential of the induced dipole moment is given by the time average of the interaction energy

$$U_{\text{dip}}(\vec{r}) = \langle W \rangle = -\frac{1}{2} \langle \vec{p} \vec{E} \rangle = -\frac{1}{2\epsilon_0 c} \text{Re}(\alpha) I(\vec{r}), \quad (6.2)$$

with $I(\vec{r}) = 2\epsilon_0 c |E_0(\vec{r})|^2$ the intensity of the field. The power absorbed from the driving field by the oscillator (P_{abs}) and re-emitted as dipole radiation, gives us the scattering rate

$$\Gamma_{\text{sc}}(\vec{r}) = \frac{P_{\text{abs}}}{\hbar\omega} = \frac{\langle \dot{\vec{p}} \vec{E} \rangle}{\hbar\omega} = \frac{1}{\hbar\epsilon_0 c} \text{Im}(\alpha) I(\vec{r}). \quad (6.3)$$

In the classical picture the electron is elastically bound to the core with an eigenfrequency ω_0 corresponding to the optical transition frequency. The electron is driven by the radiation field with driving frequency ω . The damping rate, resulting from the dipole radiation of the oscillating electron, is described by Larmor's formula for the power radiated by

an accelerated charge [111, 112]. The polarizability can be calculated by integrating the equation of motion for the electron, and is given by:

$$\alpha = 6\pi\epsilon_0 c^3 \frac{\Gamma}{(\omega_0^2 - \omega^2) - i(\omega^3/\omega_0^2)\Gamma}, \quad (6.4)$$

with Γ the on-resonance damping rate [111]. For $(\omega^3/\omega_0^2)\Gamma \ll |\omega_0^2 - \omega^2|$ one can write down the following equations for the dipole potential and the scattering rate:

$$U_{\text{dip}}(\vec{r}) = -3\pi c^2 \frac{\Gamma}{\omega_0^2(\omega_0^2 - \omega^2)} I(\vec{r}), \quad (6.5)$$

$$\Gamma_{\text{sc}}(\vec{r}) = \frac{6\pi c^2}{\hbar} \frac{\omega^3 \Gamma^2}{\omega_0^4 (\omega_0^2 - \omega^2)^2} I(\vec{r}). \quad (6.6)$$

However, this derivation is only valid if saturation effects can be neglected. For dipole trapping, this is usually the case, since one wants to have very low scattering rates ($\Gamma_{\text{sc}} \ll \Gamma$) and thus uses driving frequencies which are far-detuned from the atomic resonance.

If the driving frequency is below the atomic resonance ($\omega < \omega_0$, red detuning), the dipole potential is negative and the atoms are attracted to the field maxima (Fig. 6.1). For driving frequencies above the atomic resonance ($\omega > \omega_0$, blue detuning), the atoms are pushed to the field minima.

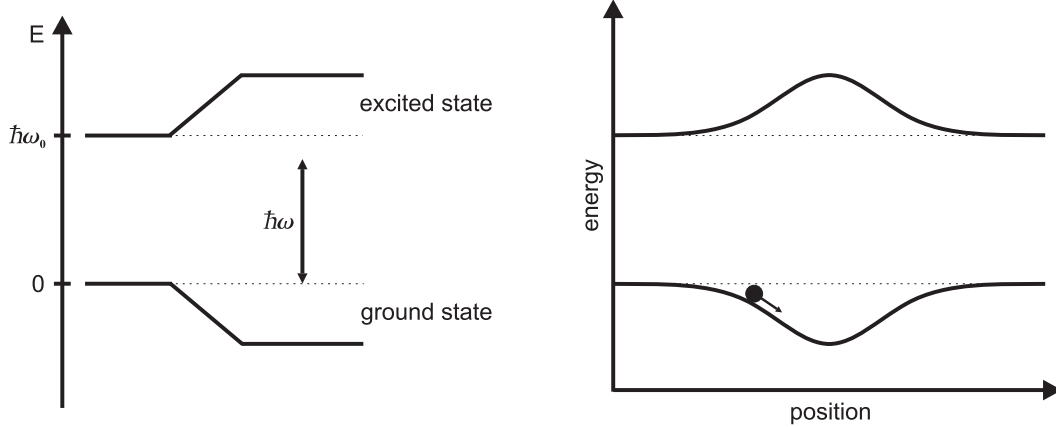


Figure 6.1: *Energy shift for a two-level atom interacting with a laser field. Left-hand side: Red detuned light shifts the energy levels equally apart. Right-hand side: A spatially inhomogeneous light field, for example a Gaussian laser beam, creates a dipole potential in which the atoms can be trapped.*

Multi-level atoms

Real atoms have a complex electronic structure, and thus there are many more levels involved. The dipole potential depends on the specific substate of the atom and the simple

oscillator model as described above has to be extended. Each transition from the desired state i to a level k , with its own particular transition strength, has an individual induced polarizability α_{ik} . The sum of all these individual polarizabilities gives us the total polarizability of this specific substate i .

In another approach the interaction of the atoms with the laser is seen as a second-order perturbation. The interaction of an atom with a laser field, given by the Hamiltonian $H_1 = -\hat{\mu}\vec{E}$ with $\hat{\mu} = -e\vec{r}$ representing the electric dipole operator, leads to an energy shift U_i of an atomic state i with Zeeman level m_i . This energy shift can be expressed as $U_i(\vec{r}, \omega) = -\alpha_i(\omega)I(\vec{r})/2\epsilon_0c$ with α_i the induced polarizability [113]. The latter can be calculated by summing up all the contributions from all the dipole transitions from the desired state i to the levels k , Zeeman levels m_k and transition frequencies ω_{ik} :

$$\alpha_i(\omega) = \sum_{k, m_k} \frac{2\omega_{ik} |\langle J_k m_k | e\vec{r} | J_i m_i \rangle|^2}{\hbar(\omega_{ik}^2 - \omega^2)}. \quad (6.7)$$

The dipole matrix element $\langle J_k m_k | e\vec{r} | J_i m_i \rangle$ with J the total angular momentum and m the total angular momentum quantum number, can be further expressed as a product of a Clebsch-Gordan coefficient $CG_{J_i, m_i, q, J_k, m_k}$ and a reduced matrix element $\langle J_i || e\vec{r} || J_k \rangle$ using the Wigner-Eckart theorem [114]:

$$\langle J_k m_k | e\vec{r} | J_i m_i \rangle = \langle J_i J_p m_i q | J_k m_k \rangle \langle J_i || e\vec{r} || J_k \rangle \equiv CG_{J_i, m_i, q, J_k, m_k} \langle J_i || e\vec{r} || J_k \rangle, \quad (6.8)$$

with $J_p = 1$ the photon momentum and $q = 0, \pm 1$ the polarization of the driving field ω . The reduced matrix element is given by

$$|\langle J_i || e\vec{r} || J_k \rangle|^2 = A_{ki} \frac{3\pi\epsilon_0\hbar c^3}{\omega_{ik}^2}, \quad (6.9)$$

with A_{ki} the Einstein coefficient, which is the spontaneous emission rate Γ_{ki} for $\epsilon_k > \epsilon_i$. $\epsilon_{i,k}$ is the unperturbed energy of the i, k -th state [115]. This gives us the following equations for the dipole potential and the scattering rate for multi-level atoms:

$$U_{\text{dip}}(\vec{r}) = -3\pi c^2 I(\vec{r}) \sum_{k, m_k} \frac{CG_{J_i, m_i, q, J_k, m_k}^2 \Gamma_{ki}}{\omega_{ik}^2 (\omega_{ik}^2 - \omega^2)}, \quad (6.10)$$

$$\Gamma_{\text{sc}}(\vec{r}) = \frac{6\pi c^2}{\hbar} I(\vec{r}) \sum_{k, m_k} \frac{\omega^3 CG_{J_i, m_i, q, J_k, m_k}^4 \Gamma_{ki}^2}{\omega_{ik}^4 (\omega_{ik}^2 - \omega^2)^2}. \quad (6.11)$$

The above equations are valid for atoms without a nuclear spin. For atoms with a nuclear spin and thus a hyperfine structure (for example ^{21}Ne , ^{85}Rb and ^{87}Rb), Eq. 6.7 has to be slightly modified. Instead of the dipole matrix $\langle J_k m_k | e\vec{r} | J_i m_i \rangle$ we now have the dipole matrix $\langle F_k m_{F_k} | e\vec{r} | F_i m_{F_i} \rangle$. This dipole matrix can be expressed as a product of a Clebsch-Gordan coefficient $CG_{F_i, m_{F_i}, q, F_k, m_{F_k}}$ and the reduced matrix element $\langle F_i || e\vec{r} || F_k \rangle$:

$$\begin{aligned}
\langle F_k m_{F_k} | e\vec{r} | F_i m_{F_i} \rangle &= \langle F_i 1 m_{F_i} q | F_k m_{F_k} \rangle \langle F_i || e\vec{r} || F_k \rangle \\
&\equiv CG_{F_i, m_{F_i}, q, F_k, m_{F_k}} \langle F_i || e\vec{r} || F_k \rangle.
\end{aligned} \tag{6.12}$$

The reduced matrix element can be further written as a product of a Wigner $6J$ symbol and the reduced matrix element $\langle J_i || e\vec{r} || J_k \rangle$:

$$\begin{aligned}
|\langle F_i || e\vec{r} || F_k \rangle| &\equiv |\langle J_i I F_i || e\vec{r} || J_k I F_k \rangle| \\
&= |\langle J_i || e\vec{r} || J_k \rangle| \sqrt{(2J_k + 1)(2F_i + 1)} \left\{ \begin{matrix} F_i & F_k & 1 \\ J_k & J_i & I \end{matrix} \right\},
\end{aligned} \tag{6.13}$$

with I the nuclear spin quantum number [116, 26]. For $\langle J_i || e\vec{r} || J_k \rangle$ one can write down Eq. 6.9, and the expression in large curly brackets denotes a Wigner $6J$ symbol. The derivation of the equations for the dipole potential and the scattering rate for multi-level atoms with a nuclear spin is from here on straightforward and therefore not given here.

Polarizability of neon

Both bosonic isotopes ^{20}Ne and ^{22}Ne do not have a nuclear spin, and therefore no hyperfine structure. Knowing the transition frequencies and the spontaneous emission rates for neon (see [105]), one can calculate the dipole potential and the scattering rate, using Eq. 6.10 and 6.11, for the driving frequency $\omega = 2\pi c/\lambda$ with $\lambda = 1065.7$ nm. Introducing the ac Stark shift per unit intensity \bar{u}_{dip} and the spontaneous scattering rate per unit intensity \bar{u}_{sc} , we have the following values for the $^3\text{P}_2$ and $^3\text{P}_0$ metastable states:

$$\begin{aligned}
^3\text{P}_2 : \bar{u}_{\text{dip}} &= 8.99 \cdot 10^{-37} \text{ m}^2\text{s}, \quad \text{and} \quad \bar{u}_{\text{sc}} = 7.29 \cdot 10^{-11} \text{ m}^2/\text{J}, \\
^3\text{P}_0 : \bar{u}_{\text{dip}} &= 9.15 \cdot 10^{-37} \text{ m}^2\text{s}, \quad \text{and} \quad \bar{u}_{\text{sc}} = 3.17 \cdot 10^{-11} \text{ m}^2/\text{J}.
\end{aligned} \tag{6.14}$$

For example: For a typical intensity of $6 \cdot 10^5$ W/cm² we have $U_{\text{dip}}(^3\text{P}_2)/k_B = I \cdot \bar{u}_{\text{dip}}/k_B = 0.40$ mK and $U_{\text{dip}}(^3\text{P}_0)/k_B = 0.41$ mK. The corresponding scattering rates ($\Gamma_{\text{sc}} = I \cdot \bar{u}_{\text{sc}}$) are 0.5 photons/s and 0.2 photons/s for the $^3\text{P}_2$ respectively $^3\text{P}_0$ metastable state.

6.1.2 Optical dipole trap

In the previous section, we have seen that for red detuned light, the dipole potential is negative and the atoms are attracted to the field maxima. Using a spatially inhomogeneous light field, for example a focused Gaussian laser beam, one can create a dipole potential in which atoms can be trapped in three dimensions.

Gaussian beam

The intensity distribution of a focused Gaussian beam can be written as

$$I(r, z) = I(0, z) \exp\left[-\frac{2r^2}{\omega^2(z)}\right] = \frac{2P}{\pi\omega^2(z)} \exp\left[-\frac{2r^2}{\omega^2(z)}\right], \quad (6.15)$$

where the radial and axial coordinates are given by r and z with z the distance from the focus and r the distance from the z -axis, P is the total power and $\omega(z)$ is the beam radius at which the intensity $I(r, z)$ has the value of $I(0, z)/e^2$ [117]. The beam radius $\omega(z)$ is given by

$$\omega(z) = \omega_0 \sqrt{1 + \left(\frac{z}{z_R}\right)^2}, \quad (6.16)$$

with ω_0 (waist) being the smallest beam radius and z_R is the Rayleigh length, defined as the distance to the focus at which $I(0, z_R) = \frac{1}{2}I(0, 0)$:

$$z_R = \frac{\pi\omega_0^2}{\lambda}, \quad (6.17)$$

where λ is the wavelength of the laser. The maximum intensity I_{max} , and thus the potential minima, is for $I(0, 0)$, and is given by

$$I_{max} = \frac{2P}{\pi\omega_0^2}. \quad (6.18)$$

Crossed optical dipole trap

Loading neon atoms into a crossed optical dipole trap is much more advantageous compared to loading neon atoms in a single beam optical dipole trap, because a much smaller volume and a higher density is attained. The latter gives us a good starting condition for measuring the two-body loss coefficient. To write down the intensity distribution of a crossed optical dipole trap, the intensity distribution for a focused Gaussian beam written in Cartesian coordinates is needed first:

$$I(x, y, z) = I(0, 0, z) \exp\left[-\frac{2(x^2 + y^2)}{\omega^2(z)}\right], \quad (6.19)$$

with z the axial coordinate, x the in plane, but perpendicular to z coordinate and y the out of plane, but orthogonal to x, z coordinate. The intensity distribution for a crossed optical dipole trap (CODT) can now be written as:

$$I_{CODT}(x, y, z) = I(z \sin(\frac{\alpha}{2}) + x \cos(\frac{\alpha}{2}), y, z \cos(\frac{\alpha}{2}) - x \sin(\frac{\alpha}{2})) + I(-z \sin(\frac{\alpha}{2}) + x \cos(\frac{\alpha}{2}), y, z \cos(\frac{\alpha}{2}) + x \sin(\frac{\alpha}{2})), \quad (6.20)$$

where we have applied a transformation $x \rightarrow \pm z \sin(\frac{\alpha}{2}) + x \cos(\frac{\alpha}{2})$ and $y \rightarrow z \cos(\frac{\alpha}{2}) \mp x \sin(\frac{\alpha}{2})$, with α the angle between the two laser beams. This gives us the following potential for a crossed optical dipole trap (Fig. 6.2):

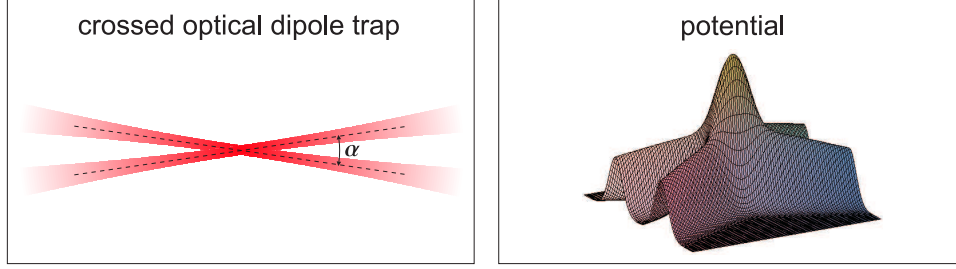


Figure 6.2: Two focused Gaussian beams crossing at an angle α produce a narrow potential well.

$$U_{CODT}(x, y, z, \omega) = -\frac{\alpha_i(\omega)}{2\epsilon_0 c} I_{CODT}(x, y, z). \quad (6.21)$$

If the atoms in the crossed optical dipole trap have a thermal energy $k_B T$, which is much lower than the depth of the optical dipole trap, one can approximate the optical dipole potential with a harmonic potential:

$$U_{CODT}(x, y, z, \omega) = U_{CODT}(0, 0, 0, \omega) \left(1 - 2\frac{x^2}{\omega_x^2} - 2\frac{y^2}{\omega_0^2} - 2\frac{z^2}{\omega_z^2} \right), \quad (6.22)$$

with $\omega_{x,z}$ given by $\omega_x^2 = (\cos^2(\frac{\alpha}{2})/\omega_0^2 + \sin^2(\frac{\alpha}{2})/2z_R^2)^{-1}$ and $\omega_z^2 = (\sin^2(\frac{\alpha}{2})/\omega_0^2 + \cos^2(\frac{\alpha}{2})/2z_R^2)^{-1}$. The trap frequencies Ω are given by:

$$\Omega_{x,z} = \sqrt{\frac{4U_{CODT}(0, 0, 0, \omega)}{m\omega_{x,z}^2}} \quad \text{and} \quad \Omega_y = \sqrt{\frac{4U_{CODT}(0, 0, 0, \omega)}{m\omega_0^2}}, \quad (6.23)$$

with m the atomic mass.

6.1.3 Density distribution in an optical dipole trap

Since the two-body losses are density dependent, one needs to calculate the mean density in order to obtain the two-body loss coefficients. The mean density n_m is defined as (Eq. 5.2)

$$n_m \equiv \frac{\int d^3r n^2(\vec{r})}{\int d^3r n(\vec{r})} = \frac{\int d^3r n^2(\vec{r})}{N}, \quad (6.24)$$

where N is the total number of atoms and $n(\vec{r})$ the density distribution for a trapped ideal gas. For an ideal gas in an infinitely deep trap, the density distribution is described by:

$$n_{\text{inf}}(\vec{r}) = n_0 \exp \left[-\frac{U(\vec{r})}{k_B T} \right], \quad (6.25)$$

with $U(\vec{r})$ the trapping potential, T the temperature of the cloud, n_0 the central density and k_B the Boltzmann constant [82]. In the harmonic approximation, the mean density is given by:

$$n_m = N \left(\frac{m}{\pi k_B T} \right)^{3/2} \Omega_x \Omega_y \Omega_z, \quad (6.26)$$

with m the atomic mass and $\Omega_{x,y,z}$ the trap frequencies in the x, y, z direction (Eq. 6.23). For a trap with finite depth ϵ_t the density distribution is described by

$$n(\vec{r}) = n_{\text{inf}}(\vec{r}) \left(\text{erf} \sqrt{\kappa(\vec{r})} - 2 \sqrt{\frac{\kappa(\vec{r})}{\pi}} \exp[-\kappa(\vec{r})] \right) = n_{\text{inf}}(\vec{r}) P(3/2, \kappa), \quad (6.27)$$

with $P(3/2, \kappa)$ the incomplete gamma function given by $P(a, x) = \int_x^\infty dt t^{a-1} e^{-t}$ and $\kappa(\vec{r}) \equiv (\epsilon_t - U(\vec{r}))/k_B T$ [82]. For large $\kappa(\vec{r})$ (≥ 10) $P(3/2, \kappa) \approx 1$. Thus $n(\vec{r}) \approx n_{\text{inf}}(\vec{r})$ and the harmonic approximation can be used. For the density distribution in a crossed optical dipole trap in the general case, when the harmonic approximation does not apply, we have:

$$n(\vec{r}) = n_0 \exp \left[-\frac{U_{\text{CODT}}(\vec{r}, \omega) - U_{\text{CODT}}(0, \omega)}{k_B T} \right] P(3/2, -U_{\text{CODT}}(\vec{r}, \omega)/k_B T), \quad (6.28)$$

with $U_{\text{CODT}}(\vec{r}, \omega)$ given by Eq. 6.21. With this expression for the density $n(\vec{r})$ the mean density in the crossed optical dipole trap can be calculated using Eq. 5.2 by numerical integration. Since the expression for the density use the full potential in the optical trap the intensity distribution of the laser beams have to be characterized as good as experimentally possible. The assumption of Gaussian laser beams can be made and is confirmed by experiment. Thus to determine the density distribution in the crossed optical dipole trap, the laser beam waists and the laser power have to be known as well as the crossing angle of the laser beams. In Chapter 7 the experimental characterization of the laser beams is described in detail. With these parameters the optical potential of the trap U_{CODT} is fully characterized, trap depth and harmonic trap frequencies can be calculated (see Section 6.1) and the density distribution in the trap is inferred from Eq. 6.28.

6.2 Implementation of a crossed optical dipole trap

In the following part, the implementation of the crossed optical dipole trap is described, followed by the loading procedure of the optical dipole trap and finally how the atoms are transferred from the 3P_2 metastable state into the 3P_0 metastable state.

6.2.1 Experimental setup

The crossed optical dipole trap was created with a 50 W Ytterbium fiber laser (*Model YLR-50-LP, IPG*) with a central wavelength at 1065.7 nm and a line width of 0.57 nm. The laser is linearly polarized and has a beam quality (M^2) of 1.04. The laser frequency is below the atomic resonances so that we have a negative dipole potential, and the atoms are attracted to the field maxima. A schematic overview of the experimental setup is given in

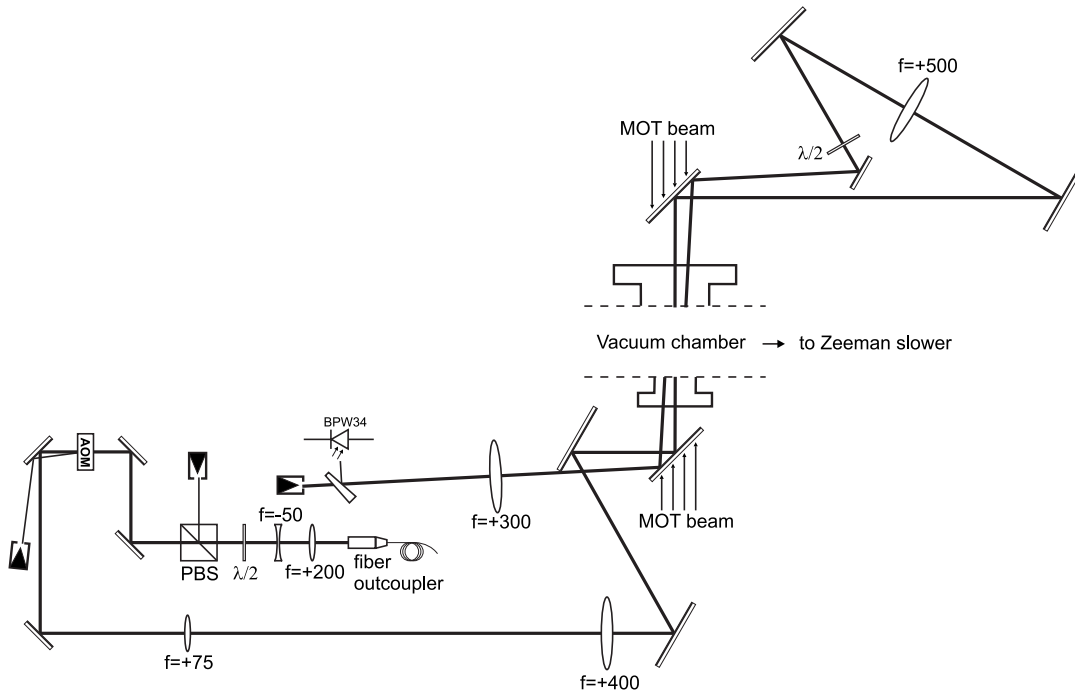


Figure 6.3: Schematic overview of the experimental setup for the optical dipole trap.

Fig. 6.3. The first optical elements the beam encounters are two lenses to reduce the waist, a half wave plate to turn the polarization and a polarizing beam splitter (PBS) to ensure a pure horizontal polarization of the laser light. For fast on/off switching of the optical dipole trap, an AOM (*Model 3110-197, Crystal Technology Inc.*) is used. The nominal efficiency for the first order is 93%, with switching times $< 1.5 \mu\text{s}$. The AOM shifts the laser frequency -120 MHz , which is negligible compared to the detuning of the laser frequency from the atomic transitions. The first order is used for the optical dipole trap and is focused by the "focusing lens". The waist is then imaged 1:1 inside the vacuum chamber with a $f = +400 \text{ mm}$ ($2''$) lens. After going through the vacuum chamber,

the beam is recycled by a converging lens which images the waist at the same position as the first one, but this time under a 2.3° angle. To prevent interference effects, the polarization of the second beam is turned 90° , using a half wave plate. The second beam - after passing the vacuum chamber - is then focused into a beam dump¹. A wedge with an anti-reflex coating at 1064 nm reflects $< 0.5\%$ (at 45°) of the power onto a photodiode used for the intensity stabilization. The electronic scheme is given in appendix B.1. The intensity stabilization allows us to modulate the intensity. This allows us to measure the trap frequencies by parametric heating [118]. Here one has to take special care to ensure that the AOM operates in a regime where a small change in rf-power leads to a visible change in the efficiency of the AOM. The thermal contact of the non-linear crystal with the heat sink is poor and most of the rf-power is dumped into the non-linear crystal so that a change of the rf-power changes the temperature of the crystal. This again leads to a change in the refraction index and thus in the (longitudinal) waist position. An elegant solution to this problem is the use of two radiofrequencies to ensure a constant total rf-power going to the AOM [119].

6.2.2 Loading of the optical dipole trap

The optical dipole trap can be loaded from both the MOT and the magnetic trap. The MOT is loaded with typically $5 - 6 \cdot 10^8$ ^{20}Ne atoms in the 3P_2 metastable state. By changing the magnetic fields, laser intensity and frequency, the atomic cloud is compressed to ensure an efficient transfer to the magnetic trap. During this compression phase, nearly no atoms are lost.

For the optimized loading of the optical dipole trap from the MOT, however, the compression stage had to be optimized for maximum densities. During this compression stage 30 – 50% of the atoms are lost and mean densities of $5 - 10 \cdot 10^{10} \text{ cm}^{-3}$ at mean temperatures of 0.4 mK are obtained. By switching on the optical dipole trap to full power during this compression stage, we were able to load $4 \cdot 10^5$ atoms in the optical dipole trap.

Better results have been obtained when the optical dipole trap was loaded from the magnetic trap. The loading sequence is as follows: After loading the magnetic trap with spin-polarized metastable neon atoms, we applied one-dimensional Doppler cooling. During the Doppler cooling, the optical dipole trap is switched on to half the maximum trap depth. Then, the magnetic fields were ramped down and we simultaneously ramp up the optical dipole trap to its maximum. We observed that the largest increase in the number of trapped atoms in the optical trap was obtained by ramping down the magnetic fields compared to turning it off immediately. The atoms in the magnetic trap are cooled by adiabatic expansion, which enhances collisional cooling and thus loading efficiency. By this we were able to load $2 \cdot 10^6$ atoms in the dipole trap.

¹Note: Due to the high laser power, the beam dumps are getting hot (up to 100°C). A beam passing close to these beam dumps will have position fluctuations due to the change in the refraction index of air by the thermal convection.

6.2.3 Optimization of the crossed optical dipole trap

Before crossing both beams in the horizontal plane one can observe the atoms in the single beams by absorption imaging. When the two beams cross an increase in density is observed in the crossing region and close to it whereas a decrease of the optical density is observed in the single beam arms of the trap further away from the crossing region. In Fig. 6.4 an absorption image of the atoms in the crossed optical dipole trap is given. When the waist of one beam is displaced from the crossing point, an asymmetry in the density distribution in the arms becomes noticeable. Waist positions can be adjusted by displacing the lenses with $f = +75$ mm and $f = +500$ mm (see Fig. 6.3) which are mounted on translation stages for this purpose. By optimizing the symmetry among the four arms of the trap observed by taking absorption images, the displacement of both waists from the center of the crossing region is minimized.

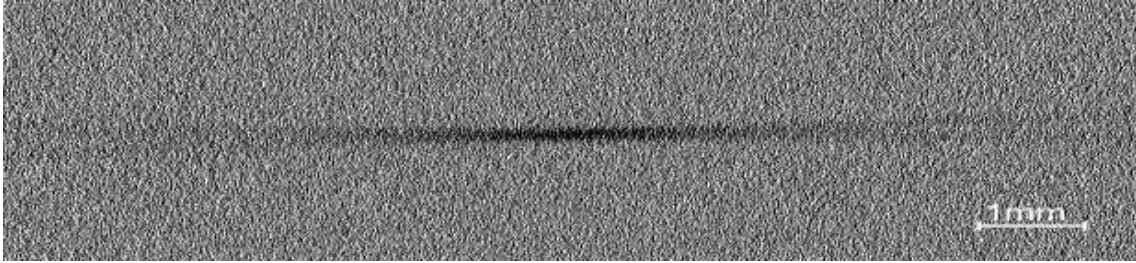


Figure 6.4: Absorption image of the atoms in the crossed optical dipole trap.

For the optimization of the crossing of both beams in the vertical plane, we temporarily rotate the half-wave plate after the $f = +500$ mm lens (see Fig. 6.3) such that the polarization of the two laser beams are no longer strictly orthogonal. Interference effects between their common polarization component produce fluctuations of the trap potential. This leads to a lower effective trap depth and as well induces heating and trap loss. Thus when the waist of one beam is overlapped perfectly with the other, a minimum in the number of atoms in the crossing region is measured. The vertical waist position of the second beam can be adjusted by displacing the $f = +500$ mm lens vertically. For this purpose the lens was mounted on a translation stage allowing precise vertical positioning. We optimized the crossing of both beams in the vertical direction by minimizing the number of trapped atoms in the crossing.

6.2.4 Transfer to the 3P_0 metastable state

An efficient method to transfer the atoms from the 3P_2 to the 3P_0 metastable state is the stimulated Raman adiabatic passage (STIRAP) [120]. Here, a complete population transfer between two quantum states is obtained by applying temporary overlapping pulses (from pump and Stokes laser). Another method to transfer the atoms from 3P_2 to the 3P_0 metastable state is to populate the 3D_1 state directly. From this state, half of the atoms decays to the 3P_0 metastable state, the other half decays to the ground state via the 1P_1 states emitting easily detectable UV photons (Fig. 6.5) [105]. The advantage of this method

is that only one laser is needed. For this, we used the home-build dye laser pumped by an argon ion laser as described in Chapter 2. The dye laser was locked at the 3P_2 - 3D_1 transition by absorption spectroscopy on a rf-discharge in a neon-filled glass cell. For fast on/off switching an AOM was used. The first order is coupled into a single-mode fiber which brings the light to the vacuum chamber. With a second AOM (placed before the 'switching' AOM) we compensated the frequency shift induced by the other AOM. An additional mechanical shutter (*Model LS2T2, Uniblitz*) before the fiber incoupler prevented stray light entering the vacuum chamber. After the fiber, we had around 40 mW of 597.7 nm light, which was then aimed at the atoms.

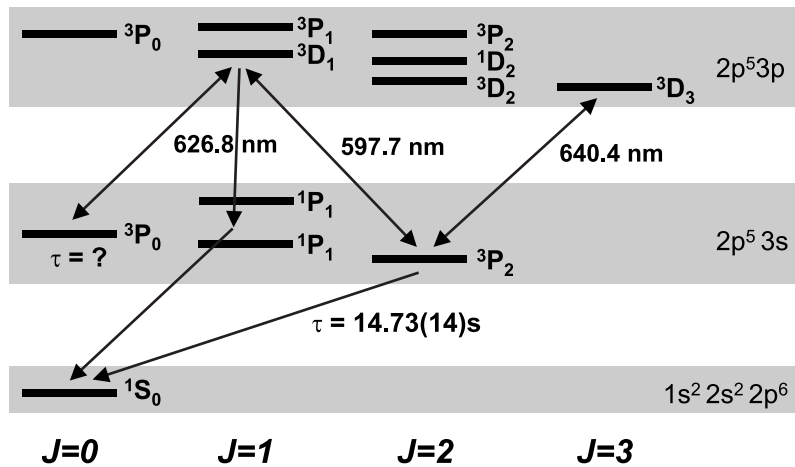


Figure 6.5: Level scheme of neon together with the transitions involved in the transfer process. For STIRAP we have to use two lasers. The Stokes laser coupling the 3P_0 metastable state with an excited state (3D_1) and the pump laser coupling the 3P_2 metastable state with that excited state.

6.3 First trapping of neon in the 3P_0 metastable state

After loading the optical dipole trap with atoms in the 3P_2 metastable state, we transfer the atoms to the 3P_0 metastable state by applying a laser pulse resonant with 3P_2 - 3D_1 transition during which the trap laser was switched off. The shortest pulse duration is 20 μs . During the time the trap laser is switched off, no atoms were lost. The transfer efficiency into the 3P_0 state is 53(7)%, and in this transfer process the temperature of the trapped atoms is increased by 5(4)% of which 1.7% can be ascribed to the gain in energy by the trap depth difference between the 3P_2 and the 3P_0 metastable state (Section 6.1.1). The uncertainty in the number of atoms and in the temperature is determined by the reproducibility of the starting condition in the optical dipole trap. Using absorption imaging, we can confirm that no atoms remain in the 3P_2 metastable state. The atoms in the 3P_0 metastable state are detected as a time-of-flight signal on the MCP detector after turning off the dipole trap. The time-of-flight signals for both metastable states are given in Fig. 6.6. This experiment confirms that we can stably trap neon in the 3P_0 state. Thus

we have cold 3P_0 atoms available for experiments in an optical trap. First collision experiments are presented in Chapter 7 where we investigate two-body loss for this state.

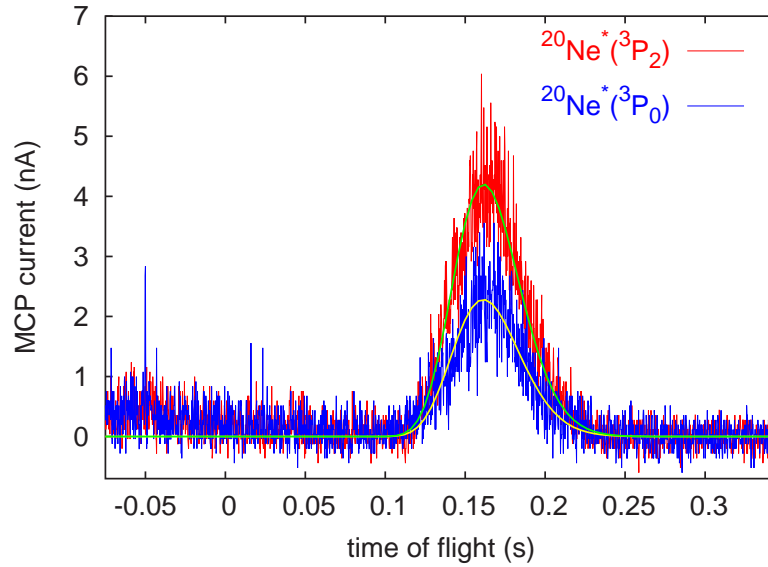


Figure 6.6: Time-of-flight signals on the MCP detector for atoms in the 3P_2 and 3P_0 metastable state. At $t = -0.05$ s, we applied a laser pulse resonant with $^3P_2 - ^3D_1$ transition. The UV photons emitted in this transfer process are also detected.

Chapter 7

Collisional properties of the 3P_0 metastable state

In the previous chapter we implemented an optical dipole trap and were able to trap - for the first time - neon in the 3P_0 metastable state. To determine whether a BEC with this metastable state is possible, we first have to measure the collisional properties of this state. So far, these properties are unknown. To extract the two-body loss coefficients from number decay measurements for the 3P_0 metastable state, a careful analysis of the trap parameters is needed (Section 7.1). The results obtained from the number decay measurements are presented in Section 7.2, followed by the conclusion.

7.1 Determination of the trap parameters

To extract the two-body loss coefficients from number decay measurements, we need to know the density distribution in the crossed optical dipole trap. This distribution is described by the angle between the beams, the waists and the power. As the uncertainty in the two-body loss coefficient depends crucially on the uncertainty of the determined trap parameters, these parameters should be determined as precise as possible.

7.1.1 Intensity distribution and beam pointing stability of the laser beams

The waists of the laser beams which form the optical dipole trap are important parameters which have to be known as precise as possible. In this section the determination of the beam waists is presented. By the same measurement the beam pointing stability was characterized.

Waist measurement

The easiest way to determine the beam waist is to measure the intensity distribution with a camera. By measuring this intensity distribution as function of the longitudinal coordinate and fitting a Gaussian function to each of these measurements, one obtains the beam radius as function of position along the beam axis. For a focused Gaussian beam, the beam radius as function of the longitudinal distance is described by Eq. 6.16. Thus fitting this equation to the measurements gives us the waist of the laser beam. The intensity distribution can as well be measured using a knife-edge. The advantage of this method is that it can also be used in narrow spacings like in this setup. The intensity distribution is measured by moving the knife-edge by means of a translation stage sideways through the laser beam. For a Gaussian beam the power measured behind the knife-edge is described by $\frac{1}{2}P[1 + \text{erf}(\sqrt{2}x/R)]$ with R the beam radius, P the measured power before the knife-edge, x the position of the knife-edge and $\text{erf}(x) = \frac{2}{\sqrt{\pi}} \int_0^x dt e^{-t^2}$. By measuring the intensity distribution at different locations along the beam, the beam radius as function of the longitudinal coordinate is obtained. We characterized both the vertical and the horizontal intensity distribution of the laser beam in this way.

This procedure is applied to both laser beams which from the crossed optical dipole trap. The corresponding beam radii as function of the longitudinal distance for the first beam and for the recycled, second, beam in the crossed beam geometry (Fig. 6.3) are given in Fig. 7.1. The solid lines are fits to the data points. From these fits we obtain a waist of $41 \mu\text{m}$ for the first beam and a waist of $49 \mu\text{m}$ for the second. For the second beam, the position of the horizontal and the vertical waist differs by 5 mm. In order to account for this astigmatism an effective waist of $52 \mu\text{m}$ is used to calculate the trap potential assuming circular beam profiles.

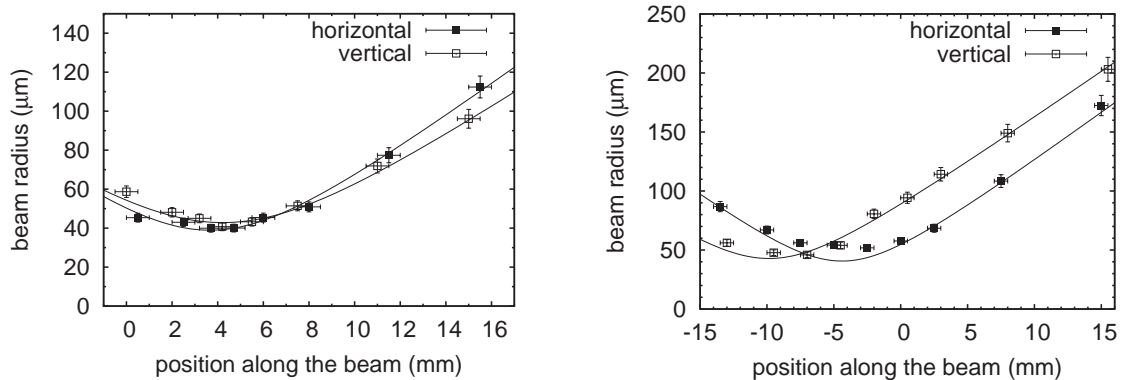


Figure 7.1: Beam radius as function of the longitudinal distance for the first beam (left) and the second beam (right).

The displacement of both waists from the center of the crossing region is minimized by optimizing the symmetry such that the column density among the four arms of the trap, i.e. such that the optical density observed in the absorption image is the same in the four arms of the trap (see Section 6.2.3). The uncertainty in the determination of the waist displacement from the center of the crossing region after this procedure is however large:

~ 7 mm. From Eq. 6.16 we see that this leads to another uncertainty in the effective laser beam waist of $\omega(7 \text{ mm}) = 70 \mu\text{m}$ with $\omega_0 = 52 \mu\text{m}$. The effective laser beam waist has to be determined more accurately by an other method (see Section 7.1.3).

Beam pointing stability

An advantage of a knife-edge to measure the intensity distribution is, that the method also allows to measure beam pointing stability of the laser beams. Since the slope of error function is maximum for $x = 0$, the highest sensitivity to position fluctuations is obtained by putting the knife-edge halfway in the beam at the position of the waist. To obtain a measurement of the beam pointing stability for both beam we insert the knife halfway in the beam and measure the intensity fluctuations behind the knife-edge with a 50Ω -coupled photodiode connected to an oscilloscope. In Fig. 7.2 the measurements for both laser beams used in the crossed trap geometry are presented. We measured the intensity fluctuations on different time-scales (ranging from $1 \mu\text{s}/\text{div}$ to $5 \text{s}/\text{div}$). By measuring the intensity without the knife-edge, we verified that these intensity fluctuations are not fluctuations in the power of the laser, but can be fully ascribed to position movements of the beam. For the first beam position fluctuations are on time-scales > 0.5 s while for the second beam position fluctuations occur on time-scales > 0.2 s. The slope, which couples the intensity fluctuations to position movements, is obtained from the measurement of the intensity distribution. For the measured beam pointing stability in the horizontal(vertical) direction of the first beam we have a slope of $2.3 \text{ V}/\text{mm}$ ($2.6 \text{ V}/\text{mm}$). The standard deviation (STDV) of the position fluctuations are $0.2 \mu\text{m}$ for both directions. For the second beam we have a slope of $0.57 \text{ V}/\text{mm}$ ($0.84 \text{ V}/\text{mm}$). Here the STDV of the position fluctuations are $4 \mu\text{m}$ for both directions. This $4 \mu\text{m}$ is much smaller compared to the beam radius. Furthermore, the frequency of the fluctuations is way smaller than the trap frequencies. The atoms follow the position fluctuations adiabatically and no heating occurs. This situation could only be reached after improving the mechanical stability, reducing mechanical vibrations, air flow and turbulences due to convection at the beam dumps (see footnote on Page 62).

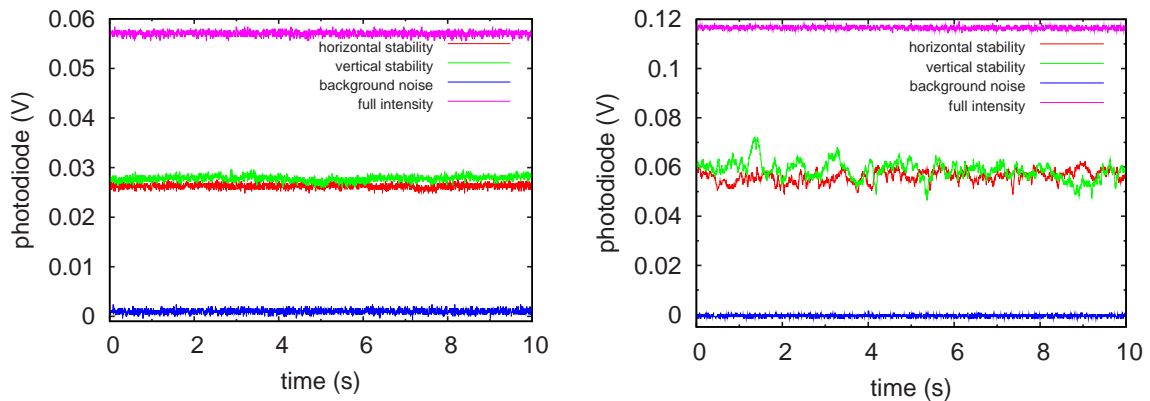


Figure 7.2: Measurements of beam pointing stability of the beams used for the optical trap: first beam (left), second beam (right).

7.1.2 Parametric heating

Parametric heating is an elegant method to measure the trap frequencies. By modulating the potential depth, transitions to higher vibrational levels in the trap can be excited if the modulation frequency equals twice the trap frequency. Atoms parametrically excited in this way climb up the ladder of vibrational levels and are thus heated out of the trap. Also at subharmonic frequencies ($\Omega_{mod} = 2\Omega_{x,y,z}/n$ where n is an integer) parametric resonances can be excited [118]. For a crossed optical dipole trap and with the harmonic approximation for the potential, trap frequencies $\Omega_{x,y,z}$ are obtained according to Eq. 6.23. For small crossing angles the potential approximately has cylindrical symmetry in radial direction and trap frequencies in x and y direction are thus equal: $\Omega_x = \Omega_y = \Omega_r$. For $\omega_0 = 50 \mu\text{m}$, $\alpha = 2.3^\circ$ and $P = 35 \text{ W}$ per beam, the trap frequencies are $\Omega_z/2\pi = 87 \text{ Hz}$ and $\Omega_r/2\pi = 4.2 \text{ kHz}$. We modulated the trap depth using the modulation input of the intensity stabilization (Appendix B). In the first phase of the experiment, the crossed optical dipole trap is loaded from the magnetic trap followed by a waiting period of 0.3 s. The intensity is then modulated with a sinusoidal signal for 0.5 s. After a delay time of 10 ms, the trap is switched off and the remaining atoms are detected with absorption imaging. In Fig. 7.3 the number of remaining atoms after this procedure are given as function of the modulation frequency. We measured the number of atoms for modulation frequencies from 0.1 to 35 kHz at a modulation depth of 5% (dots) and 3% (triangles) and in more detail from 3 to 10.5 kHz at a modulation depth of 5% (dots) and 1% (triangles).

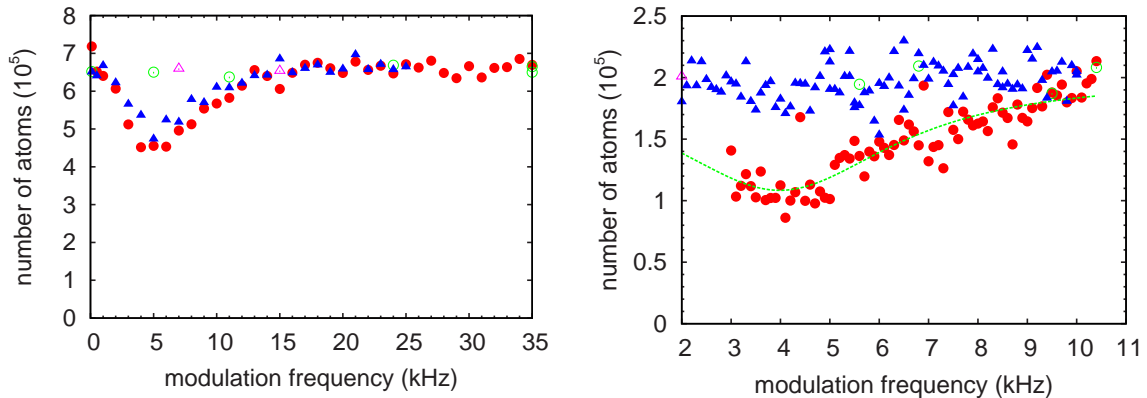


Figure 7.3: Number of atoms as function of modulation frequency. Left-hand side: Modulation of the intensity from 0.1 to 35 kHz. The number of atoms as function of modulation frequency are given by dots (modulation depth: 5% at 4 kHz) and the triangles (modulation depth: 3% at 4 kHz). The open circles and triangles give the number of atoms with zero modulation amplitude. Right-hand side: Modulation of the intensity from 3 to 10.5 kHz at a modulation depth of 5% (dots), 1% (triangles) and with zero modulation amplitude (open circles and triangles). Given as well is a Lorentz fit for the measurement at a modulation depth of 5%.

For these low modulation depths we expect to see sharp resonances at double the trap frequencies. Instead, we detected a very broad resonance with a width of 4 kHz. This can be ascribed to the anharmonicity of the optical dipole trap. The thermal energy of

the atoms, compared to the trap depth, is too high to approximate the trap potential by a harmonic potential. For a Gaussian potential the vibrational level separation decreases for higher vibrational levels. Thus the atoms in the high energy tail of the Boltzmann density distribution are excited to higher vibrational levels at different modulation frequencies compared to the atoms in the low energy tail of the Boltzmann density distribution. It results in the broad resonance as observed in Fig. 7.3. By fitting a Lorentz function to the measurement at a modulation depth of 5%, we obtain a resonance frequency of 4(4) kHz. This resonance corresponds to twice the radial trap frequency Ω_r . Using this resonance observed by parametric excitation we can infer from Eq. 6.23 with $\alpha = 2.3^\circ$ and $P = 35$ W per beam a laser beam waist of $72_{-21}^{+\infty}$ μm .

7.1.3 Measurement of the radial density distribution

The laser beam waist can also be obtained from the radial distribution of the cloud in the center of the crossed optical dipole trap. With absorption imaging we measure the radial size of the cloud. To do this we had to replace the commercial telescope (*MINOLTA MD Macro-Objective 100mm*), which has a magnification of $(2.4)^{-1}$, by a home-build telescope with larger magnification. This telescope consists of two achromats with focal lengths $f_1 = +200$ mm and $f_2 = +300$ mm respectively. The achromats were placed vertically inside the re-entrant flange as close as possible to the atomic cloud. The magnification and the resolution of the optical detection system was characterized in detail using a resolution test target USAF-1951 (*Newport; RES-1*). A calibration factor of 4.1 $\mu\text{m}/\text{pixel}$ and a resolution of 1.8 pixels were obtained. This is enough to resolve the radial distribution of the trapped cloud. In order to be more sensitive to the density distribution in the trap, absorption images are taken immediately after the trap is switched off, such that the expansion of the atomic cloud is as small as possible. The detection pulse itself, however, requires a minimum duration of 40 μs for absorption imaging to work efficiently. In absorption imaging we measure the column density, and the least square fit of a Gaussian to the image data delivers the Gaussian width of the column density distribution. The expansion of the cloud during the detection pulse is accounted for by using Eq. 2.20 and considering a time-of-flight t , which is half the detection pulse duration. With this procedure the density distribution in the trap is accurately reconstructed from the absorption image. The remaining uncertainty due to expansion of the cloud is reduced to 1%. Here the temperature is obtained from the time-of-flight measurement on the MCP detector.

To determine the density distribution of atoms in the trap from the absorption image we calculate the column density by integrating the density given by Eq. 6.28 in the out-of-plane direction for comparison with absorption data. Here, the measured parameters used in the experiment for the power $P = 29$ W per beam and for the crossing angle $\alpha = 2.1(2)^\circ$ are inserted. For the temperature and the effective laser beam waist the uncertainty is larger and the column density calculation is performed for a range of possible values of these parameters. By comparing the radial width of the calculated column density distribution with the width of the measured density distribution we then infer the most probable value to be used for the effective laser beam waist to describe the density

distribution in the trap.

The Gaussian radius in radial direction in the center of the calculated column density distribution as a function of temperature for an effective laser beam waist $\omega_0 = 70 \mu\text{m}$ is given in Fig. 7.4. Here we find that the Gaussian radius is not depending strongly

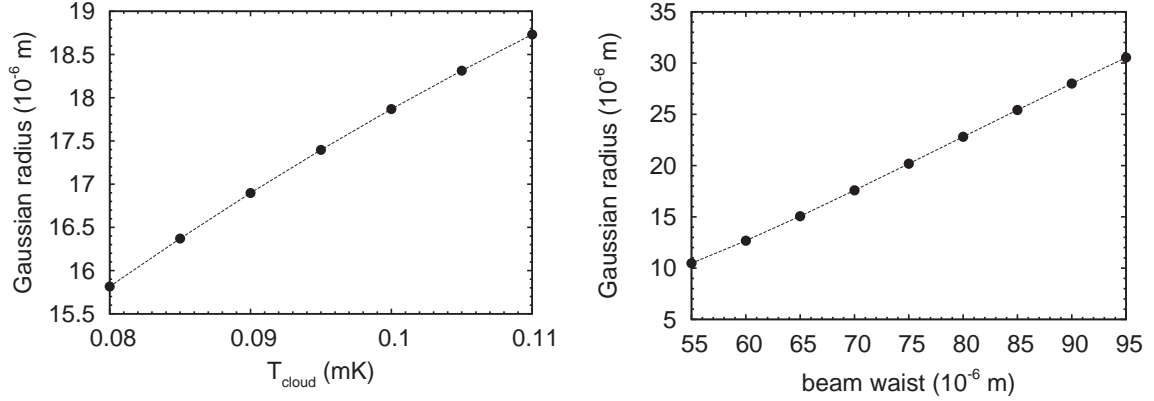


Figure 7.4: *Gaussian radius in radial direction of the calculated column density as function of temperature for $\omega_0 = 70 \mu\text{m}$ (left) and as function of the effective laser beam waist ω_0 for $T = 0.097 \text{ mK}$ (right). The curve connecting the points serves to guide the eye.*

on temperature variations. From the experimental uncertainty of 8% in the temperature measurement results an uncertainty in the Gaussian width of the distribution of only 4%.

The width of the calculated column density is depending strongly on the value used for the effective laser beam waist ω_0 as is also shown in Fig. 7.4. It is thus very important to determine the laser beam waist ω_0 accurately.

From the absorption image we infer the Gaussian radius in radial direction $\sigma_{rad} = 21(3) \mu\text{m}$ of the column density in the trap corrected for the expansion of the cloud during the detection pulse and accounting for the limited resolution of the detection system. The experimental value is now used to deduce the most probable value for the effective laser beam waist from the calculation shown in Fig. 7.4. This calculation is actually done for the temperature $T = 0.097 \text{ mK}$, which corresponds to the temperature of the atomic cloud measured when the absorption image was taken. The resulting most probable laser beam waist is $\omega_0 = 76(6) \mu\text{m}$. To the uncertainty contribute the uncertainty in σ_{rad} and the temperature uncertainty.

7.1.4 Summary of the trap parameters

The measurement of the radial density distribution turned out to be the most precise measurement of the trap parameters. Here we obtained a effective laser beam waist of $76(6) \mu\text{m}$ for the crossed optical dipole trap. With this precise determination of ω_0 the optical trap well enough characterized such that with the other parameters like laser power and crossing angle, number of atoms and temperature, which are easily measured, the trapping potential as well as the density distribution of the atoms in the trap are well known.

With a typical power of 28 W per beam the trap depth of the crossed optical dipole trap can now be calculated from Eq. 6.14: $U_{CODT}/k_B = 0.4$ mK for both metastable states. Similarly, the scattering rates are obtained: $\Gamma_{sc} = 0.4$ photons/s for 3P_2 state and $\Gamma_{sc} = 0.2$ photons/s for 3P_0 state respectively. With a recoil energy $\epsilon_r/k_B \approx 1.7$ μ K these scattering rates are small enough that the heating and trap loss which they cause at typical temperatures $T \approx 0.1$ mK can be neglected.

7.2 Determination of the two-body loss coefficient

In this section we start with the theoretical treatment of the trap loss. The functions which can be used in the least square fitting procedures to extract the two-body loss coefficients are recalled from Chapter 5 and their applicability to the measurements in the optical dipole trap is discussed. Then the experimental procedure is described and the measurements of the number of atoms as function of trap time are presented. In Section 7.2.3 systematic effects in the detection of atoms are identified and required correction procedures are introduced. From experimentally determined values for laser power, crossing angle, number of atoms and temperature we calculate the mean density necessary to extract the two-body loss coefficients from the number decay measurements. This is explained in Section 7.2.4.

7.2.1 Theoretical treatment of the trap loss

In Section 5.1 we discussed the theoretical description of the trap loss. For a constant effective volume V_{eff} (Eq. 5.2), this loss is described by:

$$N(t) = \frac{\alpha N(0)}{\left(\beta \frac{N(0)}{V_{eff}} + \alpha\right) e^{\alpha t} - \beta \frac{N(0)}{V_{eff}}}, \quad (7.1)$$

with $N(0)$ the number of atoms at $t = 0$. For a time dependent V_{eff} , for example when the cloud is heated, we arrive at the equation:

$$\begin{aligned} \left(\frac{1}{t} \log \frac{N(t)}{N(0)}\right) &= -\alpha - \beta \left(\frac{1}{t} \int_0^t dt' n_m(t')\right), \\ y(t) &= -\alpha - \beta x(t). \end{aligned} \quad (7.2)$$

These two equations can be used in least square fitting routines to extract two-body loss coefficients from the number decay measurements. Equation 7.1 is simpler, but assumes a constant effective volume V_{eff} throughout the loss measurement. Using Eq. 7.2 requires additional steps in preparation of the experimental data, i.e. calculation of the quantities

$x(t)$ and $y(t)$, but takes into account effective volume variations during the loss measurement. For trap parameters remaining constant during the measurement, the effective volume changes only if the temperature of the cloud changes in time by collisional cooling or by heating effects from inelastic collisions. Thus it is important to consider the effective volume variations occurring for the range of temperatures measured in an experimental run. For this we calculated the mean density per atom (V_{eff}^{-1}) as function of temperature for different effective laser beam waists. The results are presented in Fig. 7.5. Within

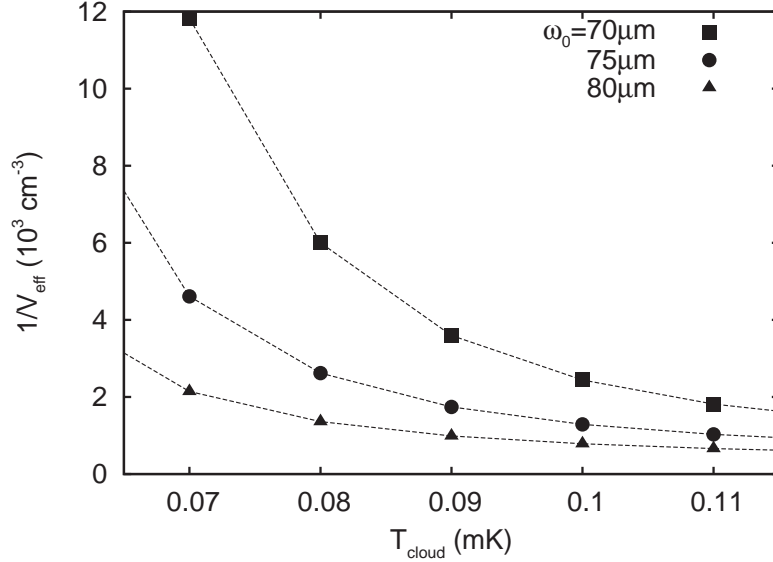


Figure 7.5: Mean density/atom (V_{eff}^{-1}) as function of the temperature for different effective waists. These calculations are carried out for typical experimental values: $P = 28 \text{ W}$ and $\alpha = 2.3^\circ$. The curve connecting the points serves to guide the eye.

the range of temperatures observed throughout a typical loss measurement, 0.08 mK to 0.1 mK (see Fig. 7.6), the calculation shows an increase of the mean density per atom by a factor of 2. Trap decay is therefore best described using Eq. 7.2 and more accurate values for two-body loss coefficients can be obtained than with the simpler function Eq. 7.1.

7.2.2 Experimental procedure

We are interested in the two-body loss coefficients for both metastable states and for both bosonic isotopes. It allows us to compare the two-body loss coefficients for the 3P_2 metastable state with the obtained values by Kuppens *et al.* [121] and Peter Spoden [81]. The two-body loss coefficients are extracted from trap loss measurements in the optical dipole trap. We load the crossed optical dipole trap from the magnetic trap using the optimized loading sequence described in Section 6.2.2. In order to measure the number decay for the atoms in the 3P_0 metastable state, we transfer the atoms shortly after loading of the optical dipole trap from the 3P_2 to the 3P_0 metastable state by applying a laser pulse resonant with 3P_2 - 3D_1 transition during which the trap laser is switched off for $20 \mu\text{s}$ (see Section 6.3). To assure that the trap conditions are the same for both metastable states,

we alternatively measure the trapped number of atoms in the 3P_2 and 3P_0 metastable state as function of trap time. By measuring the number decay back and forth repeatedly, other effects such as fluctuations in the preparation sequence are cancelled out. The number of atoms for different trapping times are determined from absorption images and from the time-of-flight signals on the MCP detector. With absorption imaging we can only detect the atoms in the 3P_2 metastable state. It allows us to verify that no atoms remain in the 3P_2 metastable state after transfer to the 3P_0 metastable state. For absorption imaging here the commercial telescope (*MINOLTA MD Macro-Objective 100mm*) with magnification of $(2.4)^{-1}$ is used. With the MCP detector we can detect both atoms in the 3P_2 and 3P_0 metastable states and for both metastable states, the detection efficiency is the same. The sensitivity of the MCP detector is larger compared to absorption imaging so that clouds with smaller number of atoms $\sim 10^5$ can still be detected. From the recorded time-of-flight signals on the MCP we obtain number of atoms and also temperature. Before each trap loss measurement we optimize the crossing of the trap laser beams (see Section 6.2.3) and measure the laser power and crossing angle. At the end of the measurements, the crossing of the trap laser beams is checked to verify that nothing changed during the trap loss measurement.

Figures 7.6 and 7.7 show an atom number decay measurement with corresponding temperatures for ^{20}Ne in both the 3P_2 and 3P_0 metastable state. The trap loss measurement for ^{22}Ne is presented in Fig. 7.8 and 7.9.

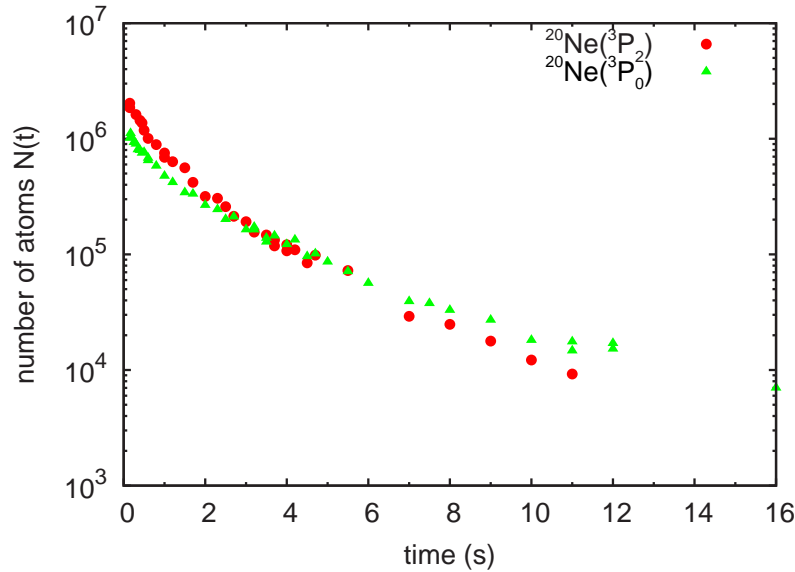


Figure 7.6: Atom number decay of ^{20}Ne of the 3P_2 and 3P_0 metastable states.

7.2.3 Systematic effects in the detection of the atoms

For loss measurements we used both absorption imaging and the MCP detector. From the time-of-flight signal on the MCP detector, number of atoms and temperature are obtained.

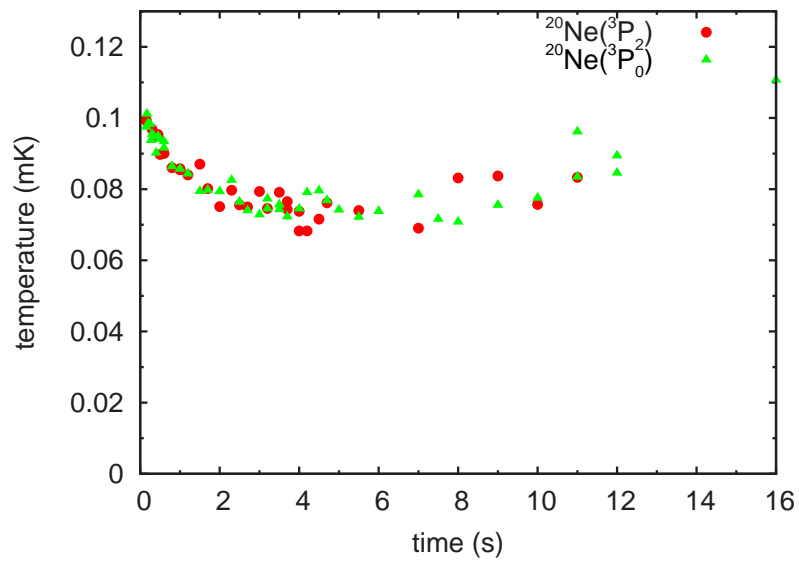


Figure 7.7: The corresponding temperatures for ^{20}Ne of the 3P_2 and 3P_0 metastable states.

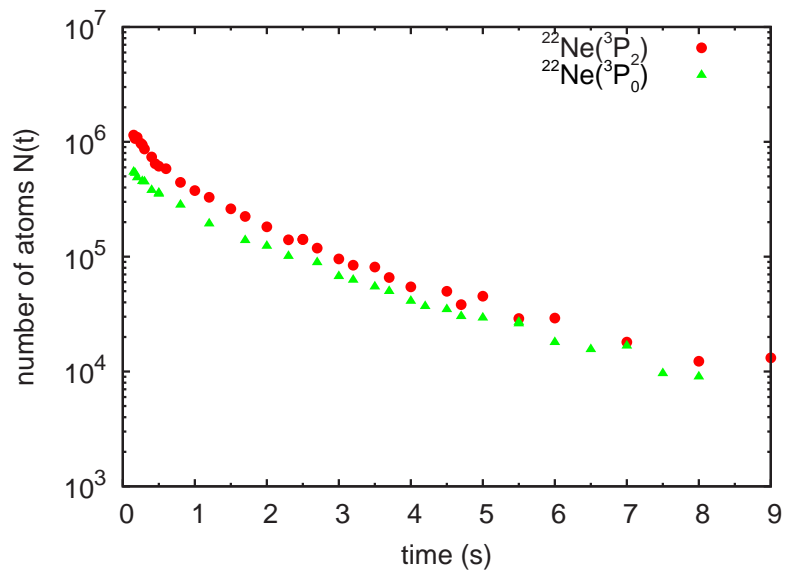


Figure 7.8: Atom number decay of ^{22}Ne of the 3P_2 and 3P_0 metastable states.

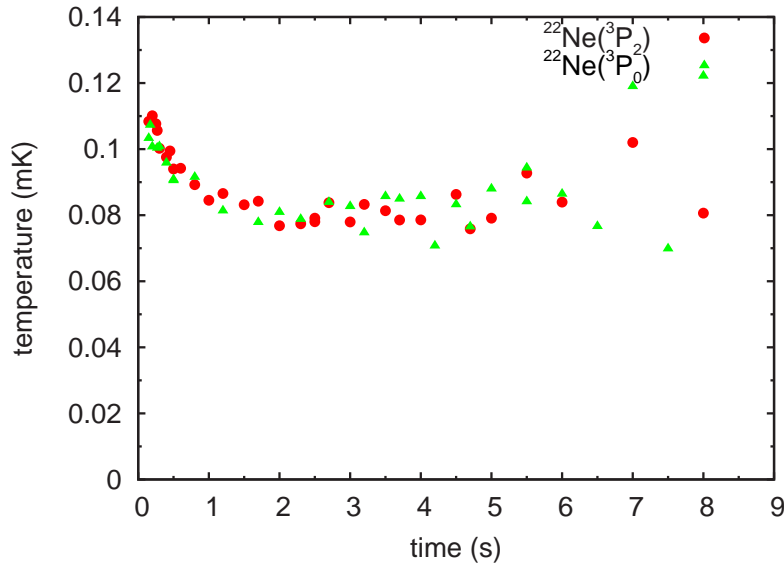


Figure 7.9: The corresponding temperatures for ^{22}Ne of the $^3\text{P}_2$ and $^3\text{P}_0$ metastable states.

Since the temperature is relatively large and corresponds to approximately a quarter of the trap depth, there is a substantial probability finding atoms close to the rim of the trap. This means that the density distribution extends in the arms of the optical trap far outside the crossing region. Atoms which are located far from the trap center do not reach the MCP detector and thus not all the atoms in the optical dipole trap are detected by the MCP detector.

The density distribution is given by Eq. 6.28 and can be calculated for a given waist, laser power and crossing angle. In order to find the fraction of atoms detected by the MCP detector, we simulate the expansion of a point shaped the cloud at different longitudinal distances from the trap center. From these simulations the contribution from different points along the z -axis to the time-of-flight signal is obtained. Weighting with the longitudinal density distribution in the optical dipole trap gives us the simulated time-of-flight signal for the elongated trapped cloud. Applying a least square fit using Eq. 2.29, allows us to determine the fraction of atoms detected by the MCP detector and the correction factor for the temperature. The correction factors for the number of atoms (C_N) and temperature (C_T) as function of effective laser beam waists and temperatures, are presented in Fig. 7.10. These factors, defined as $N = C_N \cdot N_{\text{mcp}}$ and $T = C_T \cdot T_{\text{mcp}}$, apply for both the $^3\text{P}_2$ and the $^3\text{P}_0$ metastable state. For ^{22}Ne in the $^3\text{P}_2$ metastable state we have calculated as well the correction factors and since they only differ very slightly from the correction factors obtained for ^{20}Ne , they are not given here.

Absorption imaging is a powerful tool to measure the column density distribution in the optical dipole trap. It can be used to check the calculated longitudinal column density distribution with the experiment. It allows us as well to verify the crossing in the horizontal plane from the symmetry among the four arms of the trap (see Section 6.2.3). In Fig. 7.12 a longitudinal column density distribution for different trap times during the decay measurement is given.

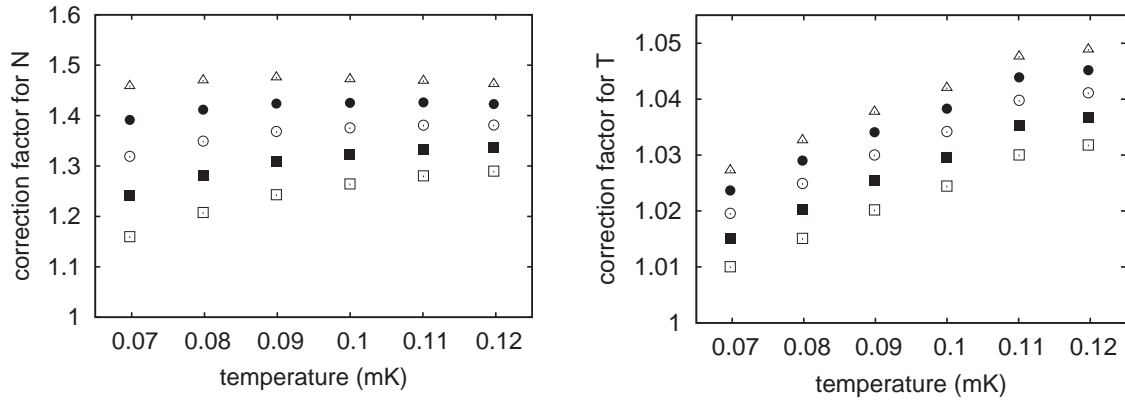


Figure 7.10: MCP data correction factors for number of atoms (left) and temperature (right) as function of temperature and waist. (Open boxes: $\omega_0 = 65 \mu\text{m}$, closed boxes: $\omega_0 = 70 \mu\text{m}$, open circles: $\omega_0 = 75 \mu\text{m}$, closed circles: $\omega_0 = 80 \mu\text{m}$, open triangles: $\omega_0 = 85 \mu\text{m}$.)

Here we applied a moving average of 31 points to the measured column density distribution. Given as well is the calculated longitudinal column density distribution for $P = 28 \text{ W}$, $\alpha = 2.3^\circ$ and $\omega_0 = 76 \mu\text{m}$ at $T = 0.1 \text{ mK}$. The inset gives the longitudinal distribution from window to window of our vacuum chamber. Compared with the MCP detector, a smaller fraction of atoms of $\sim 50\%$ is detected. Mainly in the crossing region where the optical density is largest, absorption imaging is possible with good signal-to-noise ratio. On the other hand, the MCP detector, although it does not detect all the atoms, is not sensitive to column density. An atom coming from the crossing region is practically as likely to be detected as an atom outside of the crossing (as long as it is not too far out of the trap center).

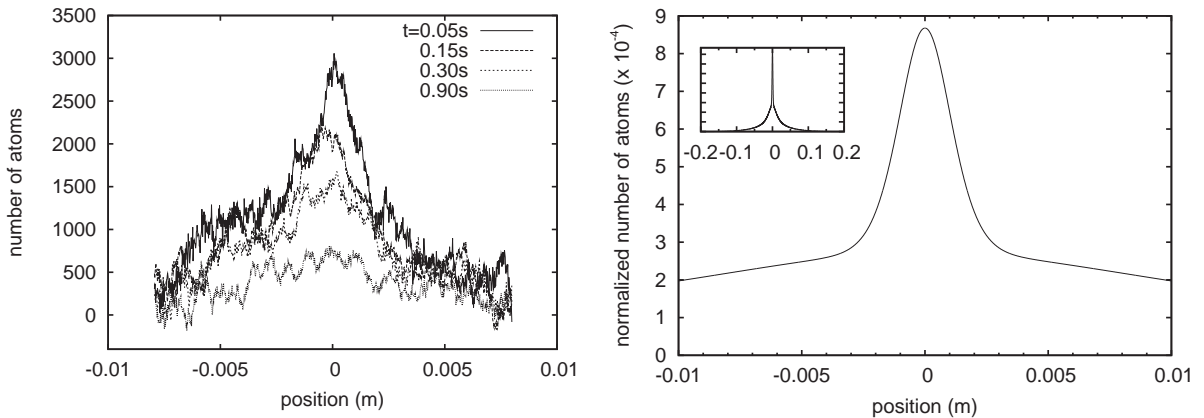


Figure 7.11: Typical longitudinal distributions measured with absorption imaging for different trapping times.

Figure 7.12: Longitudinal distribution for $P = 28 \text{ W}$, $\alpha = 2.3^\circ$, $T = 0.1 \text{ mK}$ and $\omega_0 = 76 \mu\text{m}$. The inset gives the longitudinal distribution from window to window of our vacuum chamber.

From the time-of-flight signal on the MCP, the total number of atoms and the correct

temperature is obtained using the corrections factors given in Fig. 7.10. The ratio of number of atoms in the crossing region to the total number of trapped atoms depends on the trap depth. Changing of the effective laser beam waist leads to a variation of the trap depth and a different ratio.

Comparing the calculated fraction of atoms in the trapping region with the obtained number of atoms by absorption imaging allows us to verify the effective laser beam waist. In Fig. 7.13 the longitudinal column density distribution for ^{20}Ne measured at $t = 0.15$ s together with the calculated distribution for different effective laser beam waists are presented.

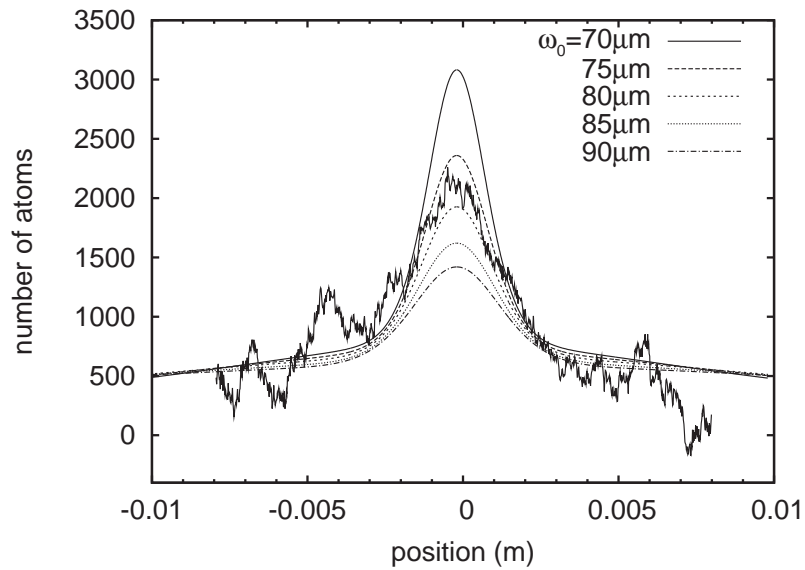


Figure 7.13: Measured longitudinal column density distribution for ^{20}Ne after $t = 0.15$ s together with the calculated distribution for $\omega = 70 - 90 \mu\text{m}$.

From this measurement we obtain an effective laser beam waist of $77(20) \mu\text{m}$. The uncertainty in the effective laser beam waist is mainly determined by the 20% uncertainty on the number of atoms detected by both absorption imaging and the MCP detector. Same analyses were applied to the trap loss measurement with ^{22}Ne . Here we determined an effective laser beam waist of $70(13) \mu\text{m}$. The trap loss measurements for both isotopes were repeated several times and the obtained effective laser beam waists do all agree within their uncertainty. We therefore can safely assume that the trap parameters stayed the same for the different atom number decay measurements and are best described by an effective laser beam waist of $76(6) \mu\text{m}$ as obtained from the measurement of the radial distribution (see Section 7.1.3).

7.2.4 Extraction of the two-body loss coefficients from atom loss measurements

To extract the two-body loss coefficient β from the trap loss measurements, we need to know the mean density for each measured point. With the well known density distribution of the atoms in the trap described by Eq. 6.28, the mean density is calculated by numerical integration of Eq. 6.24. To produce the quantity $x(t) \equiv t^{-1} \int_0^t dt' n_m(t')$ (Eq. 7.2) we do this integration of the mean density numerically. With $x(t)$ and $y(t)$, the atom number decay is described by a linear relation, where the slope is given by the two-body loss coefficient β , and the offset by the one-body loss rate α . The linear representation of the trap loss measurements for ^{20}Ne corresponding to Fig. 7.6 are given in Fig. 7.14. The linear representation of the trap loss measurements for ^{22}Ne is shown in Fig. 7.15.

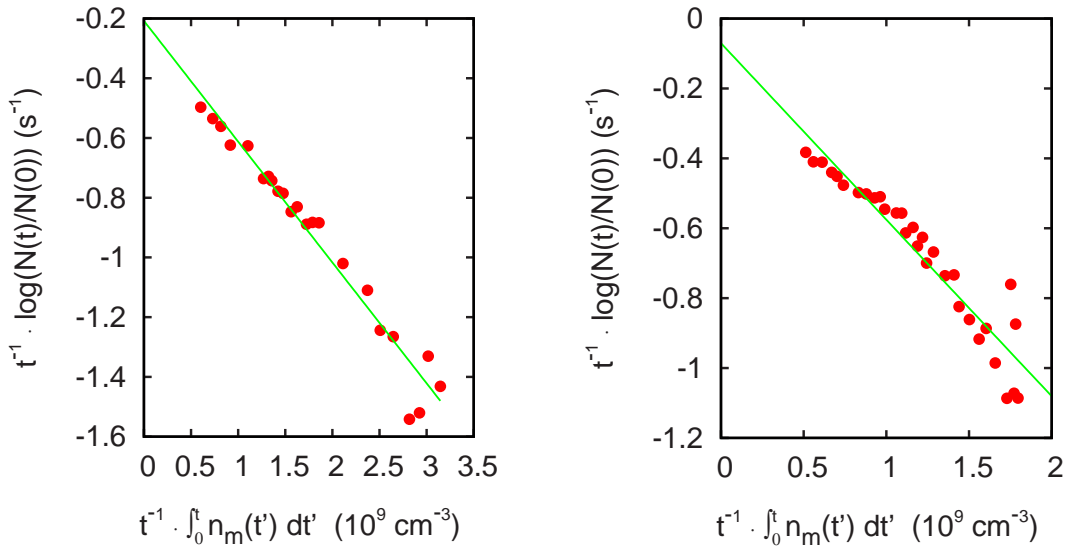


Figure 7.14: Linear representation of the trap loss measurement for ^{20}Ne . Left-hand side: Number decay of the 3P_2 unpolarized metastable state. Right-hand side: Number decay of the 3P_0 metastable state.

We measured the atom number loss for both metastable states of ^{20}Ne and ^{22}Ne several times. Using least square fitting routines and Eq. 7.2 we extracted the two-body loss coefficients from these trap loss measurements. For ^{20}Ne we obtained for the unpolarized 3P_2 metastable state: $\beta = 5_{-3}^{+4} \cdot 10^{-10} \text{ cm}^3/\text{s}$. This two-body loss coefficient is in good agreement with the measurements done by Kuppens *et al.* [121]: $5(3) \cdot 10^{-10} \text{ cm}^3/\text{s}$ and Spoden [81]: $2.5(8) \cdot 10^{-10} \text{ cm}^3/\text{s}$. It confirms that the understanding of the optical dipole trap, density distribution and analyses are accurate. For the 3P_0 metastable state we obtained: $\beta = 6_{-4}^{+5} \cdot 10^{-10} \text{ cm}^3/\text{s}$. The same analyses were applied for ^{22}Ne and here we obtained for the unpolarized 3P_2 metastable state: $\beta = 10_{-5}^{+4} \cdot 10^{-10} \text{ cm}^3/\text{s}$ and for the 3P_0 metastable state: $\beta = 11_{-6}^{+7} \cdot 10^{-10} \text{ cm}^3/\text{s}$.

The uncertainties in the two-body loss coefficients are predominantly caused by the uncertainty in the determined effective laser beam waist of the crossed optical dipole trap. We determined the effect of the uncertainty in this waist on the obtained two-body loss

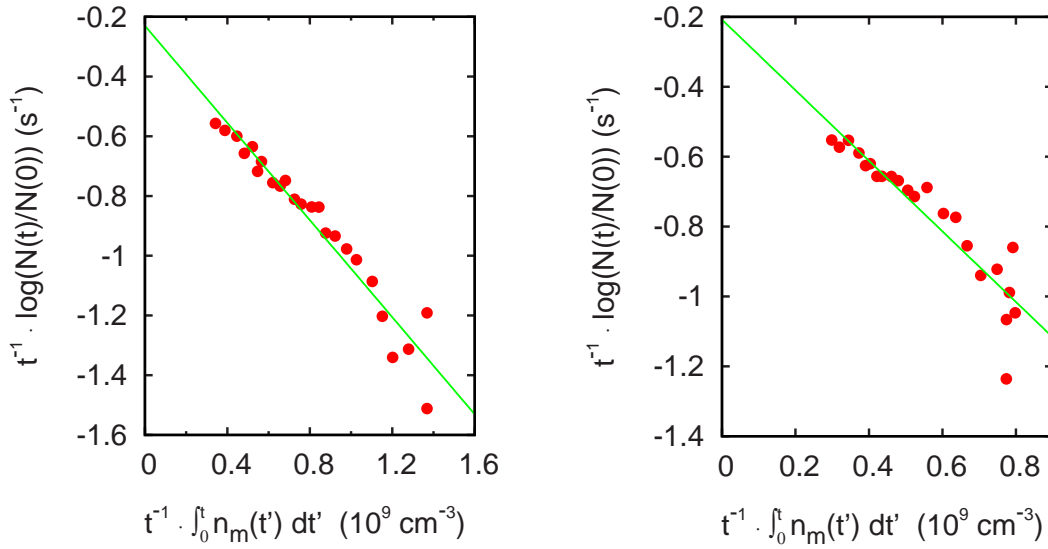


Figure 7.15: Linear representation of the trap loss measurement for ^{22}Ne . Left-hand side: Number decay of the $^3\text{P}_2$ unpolarized metastable state. Right-hand side: Number decay of the $^3\text{P}_0$ metastable state.

coefficients, by analyzing each trap loss measurement according to Eq. 7.2 for different effective laser beam waists corresponding to the uncertainty in the effective laser beam waist.

7.3 Conclusion

We have determined the two-body loss coefficient for both ^{20}Ne and ^{22}Ne in the $^3\text{P}_0$ metastable state. For ^{20}Ne we obtained $\beta(^3\text{P}_0) = 6_{-4}^{+5} \cdot 10^{-10} \text{ cm}^3/\text{s}$ whereas for ^{22}Ne we obtained $\beta(^3\text{P}_0) = 11_{-6}^{+7} \cdot 10^{-10} \text{ cm}^3/\text{s}$. Unfortunately, these two-body loss coefficients are, within the uncertainty, the same as for the unpolarized $^3\text{P}_2$ metastable state. These large two-body losses makes it extremely unlikely to reach degeneracy with this metastable state. Tuning of the collisional properties like proposed for the $^3\text{P}_2$ metastable state are not applicable for this state. Nevertheless it is important that the $^3\text{P}_0$ metastable state can be trapped to investigate other interesting physical effects. For example, it is essential to apply the STIRAP technique for trapped atoms [122] and to realize the proposed coherent control of collisions [123]. There is also a large interest in a precise determination of the lifetime of this metastable state, which is of importance for verification of QED [124].

Chapter 8

Concluding remarks

In this thesis we have examined the collisional interaction between metastable neon atoms. We have proved that the observed inelastic loss in a cloud of trapped neon atoms is almost entirely caused by Penning ionization.

Compared to some of the other atomic species, ^{22}Ne has a rate coefficient of inelastic collisions, which is several orders of magnitude larger. This hampers the evaporative cooling. Still, we were able to increase the phase-space density by a factor of 200 to $5 \cdot 10^{-5}$. Simulations of optimized evaporation for our experimental parameters are consistent with the experimental optimized evaporation route. The simulations also showed that we are limited to a phase-space density on the order of 10^{-5} . To estimate the change in collisional properties needed to reach the quantum degenerate regime, we simulated evaporative cooling for different scattering lengths and two-body loss coefficients. We determined that a 7-fold suppression of the two-body loss coefficient or a 5-fold increase in the scattering length suffices to reach quantum degeneracy.

We investigated the frequency dependence of laser-induced collisions and the possibility to excite photoassociation resonances. We observed for the $^3\text{D}_3$ line a frequency dependence of laser enhanced Penning ionization. This effect is very interesting and the result of the measurement can be useful for other measurements. We did not observe collisional enhancement effect by laser light for the transition to the $^3\text{D}_2$ line. This is intriguing and for an explanation calculations are required. An experimental signature for the excitation of photoassociation resonances was not found.

Measurements of the two-body loss coefficient as function of the magnetic field showed us that already at moderate fields there is a field dependence of the two-body loss coefficient. It allows us to tune the collisional interactions. However, the two-body loss coefficient increases towards both small and large offset fields. This can help theoreticians to determine the dependence of the two-body loss coefficient for larger magnetic fields. In the magnetic trap, we are limited to offset fields ≤ 50 G. In this range of fields, the two-body losses are too large to achieve a Bose-Einstein condensate of magnetically trapped metastable neon.

With the implementation of an optical dipole trap, the range of possible experiments was extended. We decided to trap first the $^3\text{P}_0$ metastable state. Since this state has no mag-

netic moment, it can only be trapped in an optical dipole trap. So far nothing was known about the elastic and inelastic collisions of this state. We are the first to have trapped this state. From trap loss measurements we determined the two-body loss coefficient of the 3P_0 metastable state for both bosonic isotopes ^{20}Ne and ^{22}Ne . With a two-body loss coefficient of $6_{-4}^{+5} \cdot 10^{-10} \text{ cm}^3/\text{s}$ for ^{20}Ne and $11_{-6}^{+7} \cdot 10^{-10} \text{ cm}^3/\text{s}$ for ^{22}Ne , these losses are so large that it is very unlikely to reach the quantum degenerate regime.

Nevertheless, it is important that the 3P_0 metastable state can be trapped to investigate other interesting physical effects. For example, it is essential to apply the STIRAP technique for trapped atoms [122] and to realize the proposed coherent control of collisions [123]. There is also a large interest in a precise determination of the lifetime of this metastable state, which is of importance for the verification of QED [124].

With the optical dipole trap, the two-body loss coefficient of the $^3P_2(m = +2)$ metastable state as function of the magnetic field can be measured for larger magnetic fields. Fields up to 400 G can be readily obtained using the Helmholtz coils. Furthermore, we can trap neon atoms in their energetically lowest magnetic substate $^3P_2(m = -2)$. In ^{52}Cr , loading the atoms in their lowest magnetic substate, the two-body loss was drastically reduced and led to a Bose-Einstein condensate [107].

So far we have not investigated the fermionic neon isotope ^{21}Ne with an abundance of 0.27%. Unlike the bosonic isotopes ^{20}Ne and ^{22}Ne , this isotope has a nuclear spin of $3/2$. This leads to a hyperfine structure splitting. There is no longer a closed cooling transition such as for the bosonic isotopes. In order to trap this fermionic isotope, repumpers are needed. The transitions $F = 5/2 \rightarrow F' = 7/2$, $F = 3/2 \rightarrow F' = 5/2$ and $F = 1/2 \rightarrow F' = 3/2$ are needed to repump the atoms back into the cooling transition $^3P_2(F = 7/2) \rightarrow ^3D_3(F' = 9/2)$, and are only -308.5 MHz , -449 MHz and -481 MHz shifted, respectively [125]. Therefore, these frequencies can be reached with normal AOMs. Since the frequency difference between the $F = 3/2 \rightarrow F' = 5/2$ and the $F = 1/2 \rightarrow F' = 3/2$ transition is relatively small, two repumper frequencies are sufficient to trap ^{21}Ne [126]. With the move of the experiment from the "Leibniz Universität Hannover" to the "TU Darmstadt", the optical setup was rebuilt such that we could generate these two repumper frequencies [125]. This led to a MOT with metastable ^{21}Ne . Shortly thereafter we transferred and trapped the atoms - for the first time - in the magnetic trap. $2.4 \cdot 10^6$ atoms at a mean density of $3.1 \cdot 10^8 \text{ cm}^{-3}$ were trapped in the magnetic trap. Fig. 8.1 shows the preliminary result of a trap loss measurement.

The possibility to trap fermionic neon opens up a new range of exciting experiments. In neon, the contribution of p -wave scattering is greatly suppressed for $T \leq 750 \mu\text{K}$ [81, 127, 125] and only s -wave scattering is allowed. Since the total wavefunction is anti-symmetric for fermions (Pauli exclusion principle) and s -wave scattering is thus forbidden, no collisions occur in an ultracold spin-polarized atomic cloud of fermions [128]. This is also known as "Pauli blocking". For a spin-polarized ^{21}Ne cloud with $T \leq 750 \mu\text{K}$, no collisions should occur. The suppression of the Penning ionization would be a direct measurement of "Pauli blocking". Also interesting is to trap both ^{21}Ne and ^{22}Ne simultaneously, and determine the heteronuclear collisional parameters. The frequency difference of 607 MHz between the cooling transitions ^{21}Ne and ^{22}Ne [74] can

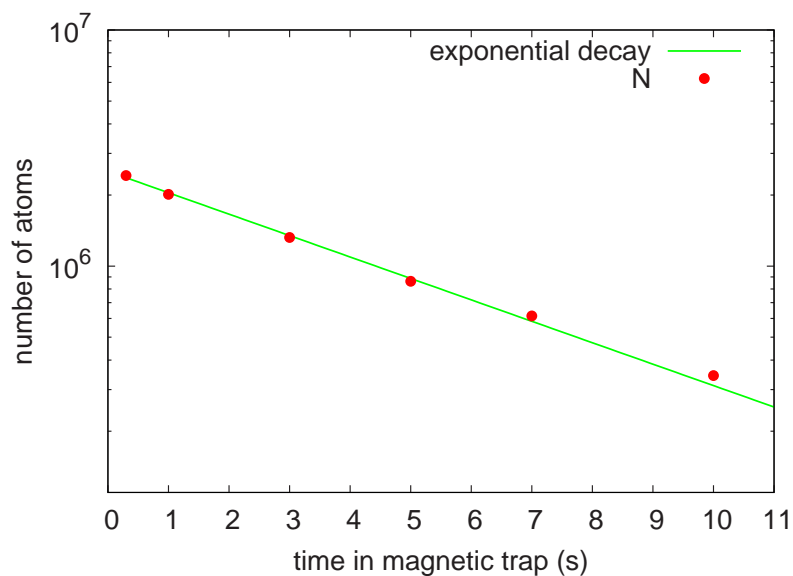


Figure 8.1: *Trap loss measurement of magnetically trapped ^{21}Ne . The line through the points is an exponential fit.*

be reached with AOMs. Trapping ^{21}Ne in an optical dipole trap allows us to examine the collisional properties for different magnetic fields and search for possible Feshbach resonances.

Bibliography

- [1] M. H. Anderson, J. R. Ensher, M. R. Matthews, C. E. Wiemann, and E. A. Cornell, *Observation of Bose-Einstein Condensation in a Dilute Atomic Vapour*, *Science* **269**, 198 (1995).
- [2] K. B. Davis, M. O. Mewes, M. R. Andrews, N. J. van Druten, D. S. Durfee, D. M. Kurn, and W. Ketterle, *Bose-Einstein Condensation in a Gas of Sodium Atoms*, *Physical Review Letters* **75**, 3969 (1995).
- [3] C. C. Bradley, C. A. Sackett, J. J. Tollet, and R. G. Hulet, *Evidence of Bose-Einstein Condensation in an Atomic Gas with Attractive Interactions*, *Physical Review Letters* **75**, 1687 (1995).
- [4] C. C. Bradley, C. A. Sackett, and R. G. Hulet, *Bose-Einstein Condensation of Lithium: Observation of Limited Condensate Number*, *Physical Review Letters* **78**, 985 (1997).
- [5] B. DeMarco and D. S. Jin, *Onset of Fermi Degeneracy in a Trapped Atomic Gas*, *Science* **285**, 1703 (1999).
- [6] A. G. Truscott, K. E. Strecker, W. I. McAlexander, G. B. Patridge, and R. G. Hulet, *Observation of Fermi Pressure in a Gas of Trapped Atoms*, *Science* **291**, 2570 (2001).
- [7] F. Schreck, K. L. Khaykovich, K. L. Corwin, G. Ferrari, T. Bourdel, J. Cuzibolles, and C. Salomon, *Quasipure Bose-Einstein Condensate Immersed in a Fermi Sea*, *Physical Review Letters* **87**, 080403 (2001).
- [8] S. Chu, *Nature* **416**, 206 (2002), an overview of this research topic is given via a compilation of Nature articles. Particularly the applications to frequency metrology and quantum information are discussed.
- [9] S. Chu, *Cold atoms and quantum control*, *Nature* **416**, 206 (2002).
- [10] J. R. Anglin and W. Ketterle, *Bose-Einstein condensation of atomic gases*, *Nature* **416**, 211 (2002).
- [11] S. L. Rolston and W. D. Phillips, *Nonlinear and quantum atom optics*, *Nature* **416**, 219 (2002).

- [12] K. Burnett, P. S. Julienne, P. D. Lett, E. Tiesinga, and C. J. Williams, *Quantum encounters of the cold kind*, Nature **416**, 225 (2002).
- [13] T. Udem, R. Holzwarth, and T. W. Hänsch, *Optical frequency metrology*, Nature **416**, 233 (2002).
- [14] C. Monroe, *Quantum information processing with atoms and photons*, Nature **416**, 238 (2002).
- [15] M. R. Andrews, C. G. Townsend, H.-J. Miesner, D. S. Durfee, D. M. Kurn, and W. Ketterle, *Observation of Interference Between Two Bose Condensates*, Science **275**, 637 (1997).
- [16] L. Deng, E. W. Hagley, J. Wen, M. Trippenbach, Y. Band, P. S. Julienne, J. E. Simsarian, K. Helmerson, S. L. Rolston, and W. D. Phillips, *Four-wave mixing with matter waves*, Nature **398**, 218 (1999).
- [17] S. Burger, K. Bongs, S. Dettmer, W. Ertmer, and K. Sengstock, *Dark Solitons in Bose-Einstein Condensates*, Physical Review Letters **83**, 5198 (1999).
- [18] J. Denschlag *et al.*, *Generating Solitons by Phase-Engineering of a Bose-Einstein Condensate*, Science **287**, 97 (2000).
- [19] K. W. Madison, F. Chevy, W. Wohlleben, and J. Dalibard, *Vortex Formation in a Stirred Bose-Einstein Condensate*, Physical Review Letters **84**, 806 (2000).
- [20] J. R. Abo-Shaer, C. Raman, J. M. Vogels, and W. Ketterle, *Observation of Vortex Lattices in Bose-Einstein Condensates*, Science **292**, 476 (2001).
- [21] M. Greiner, O. Mandel, T. Esslinger, T. W. Hänsch, and I. Bloch, *Quantum Phase Transition from a Superfluid to a Mott Insulator in a Gas of Ultracold Atoms*, Nature **415**, 39 (2002).
- [22] E. L. Raab, M. Prentiss, A. Cable, S. Chu, and D. E. Pritchard, *Trapping of Neutral Sodium Atoms with Radiation Pressure*, Physical Review Letters **59**, 2631–2634 (1987).
- [23] S. Chu, J. E. Bjorkholm, A. Aschkin, and A. Cable, *Experimental Observation of Optically Trapped Atoms*, Physical Review Letters **57**, 314 (1986).
- [24] A. L. Migdall, J. V. Prodan, W. D. Phillips, T. H. Bergeman, and H. J. Metcalf, *First Observation of Magnetically Trapped Neutral Atoms*, Physical Review Letters **54**, 2596 (1985).
- [25] H. F. Hess, *Evaporative cooling of magnetically trapped and compressed spin-polarized hydrogen*, Physical Review B **34**, 3476 (1986).
- [26] H. J. Metcalf and P. van der Straten, *Laser Cooling and Trapping* (Springer, New York, 1999).

- [27] L. S. Butcher, D. N. Stacey, C. J. Foot, and K. Burnett, *Ultracold collisions for Bose-Einstein condensation*, Philosophical Transactions of the Royal Society of London A **357**, 1421 (1999).
- [28] F. Dalfovo, S. Giorgini, L. P. Pitaevskii, and S. Stringari, *Theory of Bose-Einstein condensation in trapped gases*, Review of Modern Physics **71**, 463 (1993).
- [29] J. M. Gerton, C. A. Sacket, B. J. Few, and R. G. Hulet, *Dipolar relaxation collisions in magnetically trapped ^7Li* , Physical Review A **59**, 1514 (1999).
- [30] J. Herbig, T. Kraemer, M. Mark, T. Weber, C. C., H. C. Nägerl, and R. Grimm, *Preparation of a Pure Molecular Quantum Gas*, Science **301**, 1510 (2003).
- [31] C. A. Regal, C. Ticknor, J. L. Bohn, and D. S. Jin, *Creation of ultracold molecules from a Fermi gas of atoms*, Nature **424**, 47 (2003).
- [32] M. Greiner, C. A. Regal, and D. S. Jin, *Emergence of a Molecular Bose-Einstein Condensate from a Fermi Gas*, Nature **426**, 537 (2003).
- [33] S. Jochim, N. Bartenstein, A. Altmeyer, G. Hendl, S. Riedl, C. Chin, J. Hecker Denschlag, and R. Grimm, *Bose-Einstein Condensation of Molecules*, Science **302**, 2101 (2003).
- [34] K. E. Strecker, G. B. Partridge, and R. G. Hulet, *Conversion of an Atomic Fermi Gas to a Long-Lived Molecular Bose Gas*, Physical Review Letters **91**, 080406 (2003).
- [35] M. W. Zwierlein, C. A. Stan, C. H. Schunck, S. M. F. Raupach, S. Gupta, Z. Hadzibabic, and W. Ketterle, *Observation of Bose-Einstein Condensation of Molecules*, Physical Review Letters **91**, 250401 (2003).
- [36] C. A. Regal, M. Greiner, and D. S. Jin, *Observation of Resonance Condensation of Fermionic Atom Pairs*, Physical Review Letters **92**, 040403 (2004).
- [37] T. Bourdel, L. Khaykovich, J. Cubizolles, J. Zhang, F. Chevy, M. Teichmann, L. Tarruell, S. J. J. M. F. Kokkelmans, and C. Salomon, *Experimental Study of the BEC-BCS Crossover Region in Lithium 6*, Physical Review Letters **93**, 050401 (2004).
- [38] J. Kinast, S. L. Hemmer, M. E. Gehm, A. Turlapov, and J. E. Thomas, *Evidence for Superfluidity in a Resonantly Interacting Fermi Gas*, Physical Review Letters **92**, 150402 (2004).
- [39] M. W. Zwierlein, C. A. Stan, C. H. Schunck, S. M. F. Raupach, A. J. Kerman, and W. Ketterle, *Condensation of Pairs of Fermionic Atoms near a Feshbach Resonance*, Physical Review Letters **92**, 120403 (2004).
- [40] M. Bartenstein, A. Altmeyer, S. Riedl, S. Jochim, C. Chin, J. Hecker Denschlag, and R. Grimm, *Collective Excitations of a Degenerate Gas at the BEC-BCS Crossover*, Physical Review Letters **92**, 203201 (2004).

- [41] C. Chin, M. Bartenstein, A. Altmeyer, S. Riedl, S. Jochim, J. Hecker Denschlag, and R. Grimm, *Observation of the Pairing Gap in a Strongly Interacting Fermi Gas*, *Science* **305**, 1128–1130 (2004).
- [42] M. W. Zwierlein, J. R. Abo-Shaeer, A. Schirotzek, C. H. Schunck, and W. Ketterle, *Vortices and superfluidity in a strongly interacting Fermi gas*, *Nature* **435**, 1047–1051 (2005).
- [43] G. Roati, F. Riboli, G. Modugno, and M. Inguscio, *Fermi-Bose Quantum Degenerate $^{40}\text{K} - ^{87}\text{Rb}$ Mixture with Attractive Interaction*, *Physical Review Letters* **89**, 150403 (2002).
- [44] A. Simoni, F. Ferlaino, G. Roati, G. Modugno, and M. Inguscio, *Magnetic Control of the Interaction in Ultracold K-Rb Mixtures*, *Physical Review Letters* **90**, 163202 (2003).
- [45] M. Modugno, F. Ferlaino, F. Riboli, G. Roati, G. Modugno, and M. Inguscio, *Mean-field analysis of the stability of a K-Rb Fermi-Bose mixture*, *Physical Review A* **68**, 043626 (2003).
- [46] J. Goldwin, S. Inouye, M. L. Olsen, B. Newman, B. D. DePaola, and D. S. Jin, *Measurement of the interaction strength in a Bose-Fermi mixture with ^{87}Rb and ^{40}K* , *Physical Review A* **70**, 21601 (2004).
- [47] G. Modugno, G. Roati, F. Ferlaino, R. J. Brecha, and M. Inguscio, *Collapse of a Degenerate Fermi Gas*, *Science* **4**, 2240–2243 (2002).
- [48] C. Ospelkaus, S. Ospelkaus, K. Sengstock, and K. Bongs, *Interaction-Driven Dynamics of 40K-87Rb Fermion-Bose Gas Mixture in the Large-Particle-Number Limit*, *Physical Review Letters* **96**, 020401 (2006).
- [49] F. Ferlaino, E. de Mirandes, G. Roati, G. Modugno, and M. Inguscio, *Expansion of a Fermi Gas Interacting with a Bose-Einstein Condensate*, *Physical Review Letters* **92**, 140405 (2004).
- [50] L. De Sarlo, P. Maioli, G. Barontini, J. Catani, F. Minardi, and M. Inguscio, *Collisional properties of sympathetically cooled ^{39}K* , *Physical Review A* **75**, 022715 (2007).
- [51] S. B. Papp and C. E. Wieman, *Observation of Heteronuclear Feshbach Molecules from a ^{85}Rb - ^{87}Rb Gas*, *Physical Review Letters* **97**, 180404 (2006).
- [52] J. Lawall, S. Kulin, B. Saubamea, N. Bigelow, M. Leduc, and C. Cohen-Tannoudji, *Three-Dimensional Laser Cooling of Helium Beyond the Single-Photon Recoil Limit*, *Physical Review Letters* **75**, 4194 (1995).
- [53] A. Scholz, M. Christ, D. Doll, J. Ludwig, and W. Ertmer, *Magneto-optical preparation of a slow, cold and bright Ne^* atomic beam*, *Optics Communications* **111**, 155 (1994).

- [54] M. Schiffer, M. Christ, G. Wokurka, and W. Ertmer, *Temperatures near the recoil limit in an atomic funnel*, Optics Communications **134**, 423 (1997).
- [55] S. Kuppens, M. Raucher, M. Schiffer, K. Sengstock, W. Ertmer, F. E. van Drosselaer, and G. Nienhuis, *Polarization-gradient cooling in a strong doughnut-mode dipole potential*, Physical Review A **58**, 3068 (1998).
- [56] F. Shimizu, K. Shimizu, and H. Takuma, *Double-slit interference with ultracold metastable neon atoms*, Physical Review A **46**, R17 (1992).
- [57] J. Fujita, M. Morinaga, T. Kishimoto, M. Yasuda, S. Matsui, and F. Shimizu, *Manipulation of an atomic beam by a computer-generated hologram*, Nature **380**, 691 (1996).
- [58] B. Saubaméa, T. W. Hijmans, S. Kulin, E. Rasel, E. Peik, M. Leduc, and C. Cohen-Tannoudji, *Direct Measurement of The Spatial Correlation Function of Ultracold Atoms*, Physical Review Letters **79**, 3146 (1997).
- [59] F. M. Penning, *Naturwissenschaften* **15**, 818 (1927).
- [60] G. V. Shlyapnikov, J. T. M. Walraven, U. M. Rahmanov, and M. W. Reynolds, *Decay Kinetics and Bose Condensation in a Gas of Spin-Polarized Triplet Helium*, Physical Review Letters **73**, 3247 (1994).
- [61] P. O. Fedichev, M. W. Reynolds, U. M. Rahmanov, and G. V. Shlyapnikov, *Inelastic decay processes in a gas of spin-polarized triplet helium*, Physical Review A **53**, 1447 (1996).
- [62] N. Herschbach, P. J. J. Tol, W. Vassen, W. Hogervorst, G. Woestenenk, J. W. Thomsen, P. van der Straten, and A. Niehaus, *Photoassociation Spectroscopy of Cold He(2^3S) Atoms*, Physical Review Letters **84**, 1874–1877 (2000).
- [63] A. Robert, O. Sirjean, A. Browaeys, J. Poupard, S. Nowak, D. Boiron, C. I. Westbrook, and A. Aspect, *A Bose-Einstein Condensate of Metastable Atoms*, Science **292**, 461 (2001).
- [64] F. Pereira Dos Santos, J. Léonard, J. Wang, C. J. Barrelet, F. Perales, E. Rasel, C. S. Unnikrishnan, M. Leduc, and C. Cohen-Tannoudji, *Bose-Einstein Condensation of Metastable Helium*, Physical Review Letters **86**, 3459 (2001).
- [65] A. S. Tychkov, J. M. Jeltès, J. M. McNamara, P. J. J. Tol, N. Herschbach, W. Hogervorst, and W. Vassen, *Metastable helium Bose-Einstein Condensate with a large number of atoms*, Physical Review A **73**, 031603(R) (2006).
- [66] R. G. Dall and A. G. Truscott, *Bose-Einstein condensation of metastable helium in a bi-planar quadrupole Ioffe configuration trap*, Optics Communications **270**, 255–261 (2007).
- [67] T. Jeltès *et al.*, *Comparison of the Hanbury Brown-Twiss effect for bosons and fermions*, Nature **445**, 402–405 (2007).

- [68] M. R. Doery, E. J. D. Vredenburg, S. S. Op de Beek, H. C. W. Beijerinck, and B. J. Verhaar, *Limit on suppression of ionization in metastable neon traps due to long-range anisotropy*, Physical Review A **58**, 3673–3682 (1998).
- [69] C. Orzel, M. Walhout, U. Sterr, P. S. Julienne, and S. L. Rolston, *Spin polarization and quantum-statistical effects in ultracold ionizing collisions*, Physical Review A **59**, 1926 (1999).
- [70] P. Spoden, M. Zinner, N. Herschbach, W. J. van Drunen, W. Ertmer, and G. Birkl, *Collisional Properties of Cold Spin-Polarized Metastable Neon Atoms*, Physical Review Letters **94**, 223201 (2005).
- [71] A. Derevianko and S. G. Porsev, *Ultracold Collisional Properties of Metastable Alkaline-Earth Atoms*, Physical Review Letters **90**, 063002 (2003).
- [72] V. Kokoouline, R. Santra, and C. H. Greene, *Multichannel Cold Collisions between Metastable Sr Atoms*, Physical Review Letters **90**, 253201 (2003).
- [73] N. Vansteenkiste, C. Gerz, R. Kaiser, L. Hollberg, C. Salomon, and A. Aspect, *A frequency-stabilized LNA laser at 1.083 μm : application to the manipulation of helium 4 atoms*, Journal de Physique II France **1**, 1407–1428 (1991).
- [74] E.-M. Kriener, *Speicherung von metastabilen Neon-Atomen*, Diplomarbeit, Technische Universität Darmstadt, 2008.
- [75] A. Aclan, *Erzeugung eines langsamen Atomstrahls für eine Neon-Atomfalle*, Diplomarbeit, Universität Hannover, 1999.
- [76] M. Zinner, *Untersuchungen an lasergekühlten metastabilen Neonatomen*, Dissertation, Universität Hannover, 2002.
- [77] E. L. Raab, M. Prentiss, A. Cable, S. Chu, and D. E. Pritchard, *Trapping of Neutral Sodium Atoms with Radiation Pressure*, Physical Review Letters **59**, 2631–2634 (1987).
- [78] K. Lindquist, M. Stephens, and C. Wieman, *Experimental and theoretical study of the vapor-cell Zeeman optical trap*, Physical Review A **46**, 4082–4090 (1992).
- [79] T. Walker, D. Sesko, and C. Wieman, *Collective Behavior of Optically Trapped Neutral Atoms*, Physical Review Letters **64**, 408–412 (1990).
- [80] C. G. Townsend, N. H. Edwards, C. J. Cooper, K. P. Zetie, C. J. Foot, A. M. Steane, P. Szriftgiser, H. Perrin, and J. Dalibard, *Phase-space density in the magneto-optical trap*, Physical Review A **52**, 1423–1440 (1995).
- [81] P. Spoden, *Stoßwechselwirkungen in einem kalten Gas metastabiler Neonatome*, Dissertation, Universität Hannover, 2004.
- [82] O. J. Luiten, M. W. Reynolds, and J. T. M. Walraven, *Kinetic theory of the evaporative cooling of a trapped gas*, Physical Review A **53**, 381–389 (1996).

- [83] N. Herschbach, *Trapped triplet helium atoms: Inelastic collisions and evaporative cooling*, Dissertation, Vrije Universiteit Amsterdam, 2003.
- [84] P. O. Schmidt, S. Hensler, J. Werner, T. Binhammer, A. Görlitz, T. Pfau, and A. Simoni, *Doppler cooling of an optically dense cloud of trapped atoms*, Journal of the Optical Society of America B **20**, 960–967 (2003).
- [85] K. Huang, *Statistical Mechanics*, 2nd ed. (Wiley, New York, 1987).
- [86] K. Bongs, *Atomoptische Untersuchungen mit Bose-Einstein Kondensaten*, Dissertation, Universität Hannover, 1999.
- [87] P. J. J. Tol, W. Hogervorst, and W. Vassen, *Theory of evaporative cooling with energy-dependent elastic scattering cross section and application to metastable helium*, Physical Review A **70**, 013404 (2004).
- [88] C. Fühner, *Numerische Simulation und Optimierung der Verdampfungskühlung*, Diplomarbeit, Universität Hannover, 1997.
- [89] C. A. Sacket, C. C. Bradley, and R. G. Hulet, *Optimization of evaporative cooling*, Physical Review A **55**, 3797–3801 (1997).
- [90] P. O. Fedichev, M. W. Reynolds, and G. V. Schlyapnikov, *Three-body Recombination of Ultracold Atoms to a Weakly Bound Level*, Physical Review Letters **77**, 2921–2924 (1996).
- [91] K.-A. Suominen, *Theories of cold atomic collisions in light fields*, Journal of Physics B **29**, 5981–6007 (1996).
- [92] S. D. Gensemer and P. L. Gould, *Ultracold Collisions Observed in Real Time*, Physical Review Letters **80**, 936–939 (1998).
- [93] D. Sesko, T. Walker, C. Monroe, A. Gallagher, and C. Wieman, *Collisional losses from a light-force atom trap*, Physical Review Letters **63**, 961 (1989).
- [94] P. S. Julienne, A. M. Smith, and K. Burnett, *Theory of collisions between laser cooled atoms*, Advances in Atomic, Molecular, and Optical Physics **30**, 141 (1992).
- [95] C. D. Wallace, V. Sanchez-Villicana, T. P. Dinneen, and P. L. Gould, *Suppression of Trap Loss Collisions at Low Temperature*, Physical Review Letters **74**, 1087 (1995).
- [96] V. Sanchez-Villicana, S. D. Gensemeyer, K. Y. N. Tan, A. Kumarakrishnan, T. P. Dinneen, W. Süptitz, and P. L. Gould, *Suppression of Ultracold Ground-State Hyperfine-Changing Collisions with Laser Light*, Physical Review Letters **74**, 4619 (1995).
- [97] E. Tiesinga, C. J. Williams, P. S. Julienne, K. M. Jones, P. D. Lett, and W. D. Phillips, *A Spectroscopic Determination of Scattering Lengths for Sodium Atom Collisions*, Journal of Research of the National Institute of Standards and Technology **101**, 505–520 (1996).

- [98] E. R. I. Abraham, W. I. McAlexander, J. M. Gerton, R. G. Hulet, R. Côté, and A. Dalgarno, *Triplet s-wave resonance in ^6Li collisions and scattering lengths of ^6Li and ^7Li* , *Physical Review A* **55**, R3299–R3302 (1997).
- [99] J. R. Gardner, R. A. Cline, J. D. Miller, D. J. Heinzen, H. M. J. M. Boesten, and B. J. Verhaar, *Collisions of Doubly Spin-Polarized, Ultracold ^{85}Rb Atoms*, *Physical Review Letters* **74**, 3764–3767 (1995).
- [100] P. D. Lett, P. S. Julienne, and W. D. Phillips, *Photoassociative Spectroscopy of Laser-Cooled Atoms*, *Annual Review of Physical Chemistry* **46**, 423–452 (1995).
- [101] W. C. Stwalley and H. Wang, *Photoassociation of Ultracold Atoms: A New Spectroscopic Technique*, *Journal of Molecular Spectroscopy* **195**, 194–228 (1999).
- [102] J. Léonard, M. Walhout, A. P. Mosk, T. Müller, M. Leduc, and C. Cohen-Tannoudji, *Giant Helium Dimers Produced by Photoassociation of Ultracold Metastable Atoms*, *Physical Review Letters* **91**, 073203 (2003).
- [103] S. Moal, M. Portier, J. Kim, J. Dugué, U. D. Rapol, M. Leduc, and C. Cohen-Tannoudji, *Accurate Determination of the Scattering Length of Metastable Helium Atoms Using Dark Resonances between Atoms and Exotic Molecules*, *Physical Review Letters* **96**, 023203 (2006).
- [104] M. R. Doery, E. J. D. Vredenburg, J. G. C. Tempelaars, H. C. W. Beijerinck, and B. J. Verhaar, *Long-range diatomic $s + p$ potentials of heavy rare gases*, *Physical Review A* **57**, 3603–3620 (1998).
- [105] NIST Atomic Spectra Database, <http://physics.nist.gov/PhysRefData/ASD/index.html>.
- [106] J. Söding, D. Guéry-Odelin, P. Desbiolles, G. Ferrari, and J. Dalibard, *Giant Spin Relaxation of an Ultracold Cesium Gas*, *Physical Review Letters* **80**, 1869–1872 (1998).
- [107] A. Griesmaier, J. Werner, S. Hensler, J. Stuhler, and T. Pfau, *Bose-Einstein Condensation of Chromium*, *Physical Review Letters* **94**, 160401 (2005).
- [108] T. Weber, J. Herbig, M. Mark, H.-C. Nägerl, and R. Grimm, *Bose-Einstein Condensation of Cesium*, *Science* **299**, 232 (2003).
- [109] N. E. Small-Warren and L.-Y. C. Chiu, *Lifetime of the metastable 3P_2 and 3P_0 states of rare-gas atoms*, *Physical Review A* **11**, 1777–1783 (1975).
- [110] M. Zinner, P. Spoden, T. Kraemer, G. Birkl, and W. Ertmer, *Precision measurement of the metastable 3P_2 lifetime of neon*, *Physical Review A* **67**, 010501 (2003).
- [111] R. Grimm, M. Weidemüller, and Y. B. Ovchinnikov, *Optical dipole traps for neutral atoms*, *Molecular and Optical Physics* **42**, 95 (2000).
- [112] P. S. Jackson, *Classical electrodynamics* (Wiley, New York, 1962).

- [113] C. Degenhardt, H. Stoehr, U. Sterr, F. Riehle, and C. Lisdat, *Wavelength-dependent ac Stark shift of the $^1S_0 - ^3P_1$ transition at 657 nm in Ca*, *Physical Review A* **70**, 023414 (2004).
- [114] A. R. Edmonds, *Angular Momentum in Quantum Mechanics* (Princeton University Press, Princeton, 1957).
- [115] R. C. Hilborn, *Einstein coefficients, cross sections, f values, dipole moments, and all that*, *American Journal of Physics* **50**, 982–986 (1982).
- [116] D. A. Steck, *Rubidium 87 D Line Data*, <http://steck.us/alkalidata> (2001).
- [117] B. E. A. Saleh and M. C. Teich, *Fundamentals of Photonics* (John Wiley & Sons Inc., 1991).
- [118] L. D. Landau and E. M. Lifshitz, *Mechanik* (Akademie-Verlag, Berlin, 1964).
- [119] B. Fröhlich, T. Lahaye, B. Kaltenhäuser, H. Kübler, S. Müller, T. Koch, M. Fattori, and T. Pfau, *Two-frequency acousto-optic modulator driver to improve the beam pointing stability during intensity ramps*, *Review of Scientific Instruments* **78**, 043101 (2007).
- [120] K. Bergmann, H. Theuer, and B. W. Shore, *Coherent population transfer among quantum states of atoms and molecules*, *Review of Modern Physics* **70**, 1003–1025 (1998).
- [121] S. J. M. Kuppens, J. G. C. Tempelaars, V. P. Mogendorff, B. J. Claessens, H. C. W. Beijerinck, and E. J. D. Vredenbregt, *Approaching Bose-Einstein condensation of metastable neon: Over 10^9 trapped atoms*, *Physical Review A* **65**, 023410 (2002).
- [122] F. Vewinger, M. Heinz, R. G. Fernandez, N. V. Vitanov, and K. Bergmann, *Creation and Measurement of a Coherent Superposition of Quantum States*, *Physical Review Letters* **91**, 213001 (2003).
- [123] C. A. Arango, M. Shapiro, and P. Brumer, *Cold Atomic Collisions: Coherent Control of Penning and Associative Ionization*, *Physical Review Letters* **97**, 193202 (2006).
- [124] R. G. Dall, K. G. H. Baldwin, L. J. Byron, and A. G. Truscott, *Experimental Determination of the Helium $2^3P_1 - 1^1S_0$ Transition Rate*, *Physical Review Letters* **100**, 023001 (2008).
- [125] J. Schütz, *Experimente mit lasergekühlten bosonischen und fermionischen Neon-Atomen*, Diplomarbeit, Technische Universität Darmstadt, 2008.
- [126] F. Shimizu, K. Shimizu, and H. Takuma, *Laser cooling and trapping of Ne metastable atoms*, *Physical Review A* **39**, 2758–2760 (1989).
- [127] P. S. Julienne and H. M. Frederick, *Collisions of ultracold trapped atoms*, *Journal of the Optical Society of America B* **6**, 2257 (1989).

- [128] B. DeMarco, S. B. Papp, and D. S. Jin, *Pauli Blocking of Collisions in a Quantum Degenerate Atomic Fermi Gas*, Physical Review Letters **86**, 5409 (2001).
- [129] NIST Handbook of Basic Atomic Spectroscopic Data, <http://physics.nist.gov/PhysRefData/Handbook/index.html>.

Appendix A

Neon parameters

Table A.1: *Physical properties of neon [129].*

	²⁰ Ne	²¹ Ne	²² Ne
Natural abundance	90.48%	0.27%	9.25%
Atomic mass m	19.99244 u	20.99385 u	21.99139 u
	$3.320 \cdot 10^{-26}$ kg	$3.486 \cdot 10^{-26}$ kg	$3.652 \cdot 10^{-26}$ kg
Nuclear spin I	0	3/2	0

Table A.2: Relevant parameters for the manipulation of the 3P_2 metastable state. The recoil velocity and temperature are calculated for ^{20}Ne .

3P_2 metastable state		
Excitation energy		$E = 16.6 \text{ eV}$
Wavelength		$\lambda = 74.6 \text{ nm}$
Lifetime		$\tau = 14.73 \text{ s}$
$^3P_2 - ^3D_3$ cooling transition		
Vacuum wavelength		$\lambda = 640.4 \text{ nm}$
Lifetime		$\tau = 19.4 \text{ ns}$
Linewidth		$\Gamma = 2\pi \cdot 8.18 \text{ MHz}$
Saturation intensity	$I_{sat} = \frac{\pi\hbar c}{3} \frac{\Gamma}{\lambda^3}$	$I_{sat} = 4.08 \text{ mW/cm}^2$
Laser cooling parameters		
Doppler temperature	$T_D = \frac{\hbar\Gamma}{2k_B}$	$T_D = 196 \mu\text{K}$
Recoil velocity	$v_R = \frac{\hbar}{m} k_L$	$v_R = 3.1 \text{ cm/s}$
Recoil temperature	$T_R = \frac{\hbar^2 k_L^2}{mk_B}$	$T_R = 2.3 \mu\text{K}$
Zeeman shifts of the 3P_2 metastable state		
Lande' g_J -factor		$g_2 = \frac{3}{2}$
Zeeman shift	$m_J=2$	$\Delta E_2 = 3\mu_B B$
Energy difference	$\Delta m=1$	$\Delta E_2 - \Delta E_1 = \frac{3}{2}\mu_B B$

Table A.3: Relevant parameters for the optical dipole trap [105].

${}^3\text{P}_2 - {}^3\text{D}_1$ transition	
Wavelength	$\lambda = 597.7$ nm
Linewidth	$\Gamma = 2\pi \cdot 0.56$ MHz
Saturation intensity	$I_{\text{sat}} = 0.34$ mW/cm ²
${}^3\text{P}_0 - {}^3\text{D}_1$ transition	
Wavelength	$\lambda = 626.8$ nm
Linewidth	$\Gamma = 2\pi \cdot 3.96$ MHz
Saturation intensity	$I_{\text{sat}} = 2.10$ mW/cm ²
${}^1\text{D}_1(3s'[1/2]_1) - {}^3\text{D}_1$ transition	
Wavelength	$\lambda = 671.9$ nm
Linewidth	$\Gamma = 2\pi \cdot 3.45$ MHz
${}^1\text{D}_1(3s[3/2]_1) - {}^3\text{D}_1$ transition	
Wavelength	$\lambda = 613.0$ nm
Linewidth	$\Gamma = 2\pi \cdot 0.11$ MHz
ac Stark shift per unit intensity	
${}^3\text{P}_2$	$\bar{u}_{\text{dip}}(1066 \text{ nm}) = 8.99 \cdot 10^{-37}$ m ² s
${}^3\text{P}_0$	$\bar{u}_{\text{dip}}(1066 \text{ nm}) = 9.15 \cdot 10^{-37}$ m ² s
Spontaneous scattering rate per unit intensity	
${}^3\text{P}_2$	$\bar{u}_{\text{sc}}(1066 \text{ nm}) = 7.29 \cdot 10^{-11}$ m ² /J
${}^3\text{P}_0$	$\bar{u}_{\text{sc}}(1066 \text{ nm}) = 3.17 \cdot 10^{-11}$ m ² /J

Table A.4: Summary of the collision parameters for ${}^3\text{P}_2$: effective relaxation cross section σ_{rel} for $\bar{T} = 200$ and $550 \mu\text{K}$, scattering length a and the two-body loss parameters β for polarized atoms at $B_0 = 25$ G [70].

		${}^{20}\text{Ne}$	${}^{22}\text{Ne}$
$\sigma_{\text{rel}}(\sim 200 \mu\text{K})$	$[10^{-17} \text{ m}^2]$	8(2)	30(8)
$\sigma_{\text{rel}}(\sim 550 \mu\text{K})$	$[10^{-17} \text{ m}^2]$	2.8(7)	13(3)
a	$[a_0]$	-180(40)	$+150_{-50}^{+80}$
β	$[10^{-12} \text{ cm}^3/\text{s}]$	6.5(18)	12(3)

Table A.5: *Summary of the two-body loss rate coefficients obtained in this work for both metastable states.*

		^{20}Ne	^{22}Ne
$\beta(^3\text{P}_0)$	$[10^{-10} \text{ cm}^3/\text{s}]$	6_{-4}^{+5}	11_{-6}^{+7}
$\beta_{\text{unpol}}(^3\text{P}_2)$	$[10^{-10} \text{ cm}^3/\text{s}]$	5_{-3}^{+4}	10_{-5}^{+4}

Appendix B

Laser intensity stabilization scheme

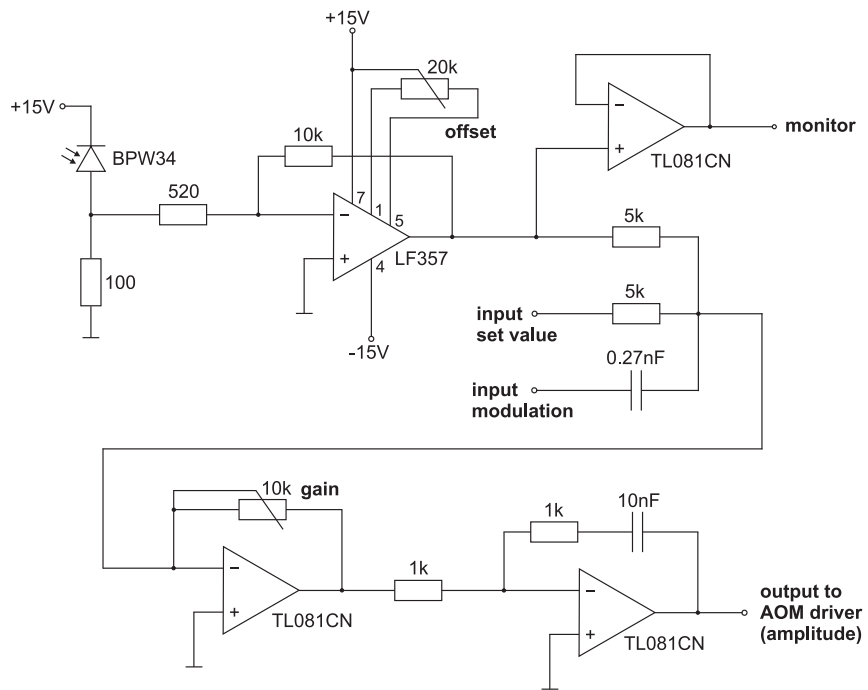


Figure B.1: *The electronic circuit for the laser intensity stabilization.*

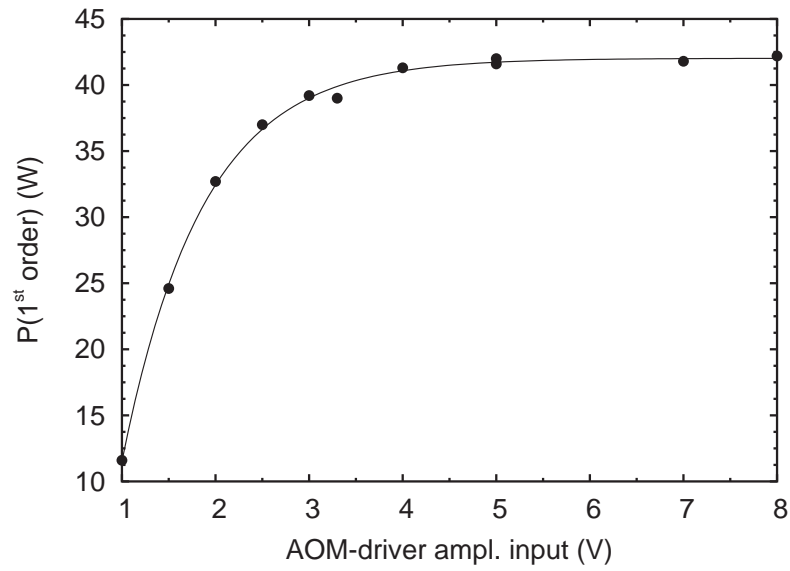


Figure B.2: Measured power in the first order of the AOM as function of the AOM-driver amplitude input for $P_{\text{laser}} = 46$ W. The line through the points (to guide the eye) is an exponential fit.

Curriculum Vitae

Name: Wouter Johannes van Drunen
Date of birth: May 31, 1977
Place of birth: Amsterdam, The Netherlands
Nationality: Dutch

Education

From 03/2007 Ph.D. at the Institute of Applied Physics, TU Darmstadt
10/2003 - 02/2007 Ph.D. at the Institute of Quantum Optics, Leibniz University of Hannover
09/1997 - 06/2002 Studies at Leiden University, The Netherlands
M.Sc. degree in physics
Master thesis in the "Optics and Mechanics" group at Philips Research Laboratories in Eindhoven, The Netherlands. Topic: "Optical feedback and intensity noise in blue semiconductor lasers" (Juni 2002)
Research assistant in the "Quantum Optics" group at Leiden University, The Netherlands. Topic: "Spatial correlation between the degenerate twin photons" (September 2001)
08/1995 - 06/1997 Pre-university education at "Radulphus College" at Curaçao, Netherlands Antilles

Work experience

08/2002 - 09/2003 Zilveren Kruis Achmea in Noordwijk, The Netherlands

Acknowledgements

My thesis could not have been realized without the help and support from various persons. I therefore gladly use this last page to thank all the people with whom I spent my PhD period.

First of all, I want to thank Prof. Dr. Gerhard Birkl for giving me the opportunity to work on this fascinating experiment and for his helpful discussions and support during all these years.

I'm very grateful to Prof. Dr. W. Elsässer for kindly accepting the role as co-referee on my thesis, even when I was rather late with my request.

This work was partly carried out in Hannover. I would like to thank Prof. Dr. Wolfgang Ertmer for his hospitality and his enormous amount of enthusiasm which really infected me.

I would particularly like to thank Dr. Norbert Herschbach, with whom I worked on this experiment. During the long measurement runs, usually ending in the early morning of the following day, but also during the time when we moved the whole experiment in a record time to Darmstadt, he kept our spirits high and concentration sharp by starting interesting discussions, giving new ideas, telling stories and jokes.

After moving the experiment to Darmstadt, Eva-Maria Kriener and Jan Schütz joined our experiment. Together we managed to put it in an up-and-running status again within no time. Recently Matthias Euler joined us. I wish both Jan, now PhD student on the neon project, and Matthias many exciting results and a great time with neon.

Without the administrative assistance of Gabriele (Gabi) Jenny-Deußer in Darmstadt and Frau Faber, Frau Hünitzsch, Frau Pfennig in Hannover nothing would have runned so smoothly. Thank you very much for making our lives so much easier.

I would also like to thank Herr Kalbfleisch and Herr Heidekrüger, representatives of the Feinmechanikwerkstatt in Darmstadt and Hannover, for creating the high quality mechanical components needed for these measurements.

The good atmosphere during and outside working hours could not have been possible if not for the presence of my colleagues Johanna Nes, Tanja Mehlstäubler, Norbert Herschbach, Sascha Drenkelforth, Oliver (Olli) Topic, Carsten Klempt, Thorsten Henninger, Tim van Zoest, Matthias Riedmann, Jens Kruse, Oliver (Olli) Wille, Jan Friebe, Stephan Falke, Michal Piotrowice and many others.

Finally, I want to thank my family and friends for their continuous support during these years. I especially would like to thank my girlfriend Katrin Hanne for always being there for me.